

2017

A BCB Diaphragm Based Adhesive Wafer Bonded CMUT Probe for Biomedical Application

Rayyan Manwar
University of Windsor

Follow this and additional works at: <https://scholar.uwindsor.ca/etd>

Recommended Citation

Manwar, Rayyan, "A BCB Diaphragm Based Adhesive Wafer Bonded CMUT Probe for Biomedical Application" (2017). *Electronic Theses and Dissertations*. 5996.
<https://scholar.uwindsor.ca/etd/5996>

This online database contains the full-text of PhD dissertations and Masters' theses of University of Windsor students from 1954 forward. These documents are made available for personal study and research purposes only, in accordance with the Canadian Copyright Act and the Creative Commons license—CC BY-NC-ND (Attribution, Non-Commercial, No Derivative Works). Under this license, works must always be attributed to the copyright holder (original author), cannot be used for any commercial purposes, and may not be altered. Any other use would require the permission of the copyright holder. Students may inquire about withdrawing their dissertation and/or thesis from this database. For additional inquiries, please contact the repository administrator via email (scholarship@uwindsor.ca) or by telephone at 519-253-3000ext. 3208.

**A BCB Diaphragm Based Adhesive Wafer Bonded CMUT Probe
for Biomedical Application**

By

Rayyan Manwar

A Dissertation

Submitted to the Faculty of Graduate Studies
through the Department of **Electrical and Computer Engineering**
in Partial Fulfillment of the Requirements for
the Degree of **Doctor of Philosophy**
at the University of Windsor

Windsor, Ontario, Canada

2017

© 2017 Rayyan Manwar

A BCB Diaphragm Based Adhesive Wafer Bonded CMUT Probe
for Biomedical Application

by

Rayyan Manwar

APPROVED BY:

T. W. Yeow, External Examiner
University of Waterloo, Waterloo, ON

E. Maeva
Department of Physics

M. Khalid
Department of Electrical and Electronic Engineering

R. Muscedere
Department of Electrical and Electronic Engineering

S. Chowdhury, Advisor
Department of Electrical and Electronic Engineering

May 08, 2017

DECLARATION OF ORIGINALITY

I hereby certify that I am the sole author of this dissertation and that no part of this dissertation has been published or submitted for publication.

I certify that, to the best of my knowledge, my dissertation does not infringe upon anyone's copyright nor violate any proprietary rights and that any ideas, techniques, quotations, or any other material from the work of other people included in my dissertation, published or otherwise, are fully acknowledged in accordance with the standard referencing practices. Furthermore, to the extent that I have included copyrighted material that surpasses the bounds of fair dealing within the meaning of the Canada Copyright Act, I certify that I have obtained a written permission from the copyright owner(s) to include such material(s) in my dissertation and have included copies of such copyright clearances to my appendix.

I declare that this is a true copy of my dissertation, including any final revisions, as approved by my dissertation committee and the Graduate Studies office, and that this dissertation has not been submitted for a higher degree to any other University or Institution.

ABSTRACT

This dissertation presents the design methodology, fabrication procedure, and key experimental characterization results of a linear array of capacitive micromachined ultrasonic transducers (CMUT) for possible ophthalmic anterior segment imaging application. The design methodology involves analytical, 3-D electromechanical finite element analysis, and Verasonics Vantage 128 ultrasonic research platform based diagnostic imaging simulations to develop a technique that minimizes electrical charging and center frequency drift while improving the transduction efficiency. In the design, Bisbenzocyclobutene (BCB), a low K polymer from Dow Chemical Company, has been innovatively used for the first time to fabricate the structural layer of the CMUT diaphragm, realize the interelectrode dielectric spacer, and to act as a low temperature adhesive bonding agent. Additionally, the top CMUT electrode has been placed at the bottom of the diaphragm to affect higher capacitance change that increases sensitivity and provides additional decoupling of the electrical charging effects. Several arrays with element count ranging from 8 to 128 elements and a center frequency range of 5 MHz to 40 MHz have been designed and fabricated. Due to an unforeseen adhesion issue during wirebonding, a 32 channel 40 MHz CMUT array has been packaged manually to validate the fabrication process and CMUT operation. Extensive SEM inspections of the CMUT cross-sections show good agreement with the design specifications. Static and dynamic measurements using a Polytec laser Doppler vibrometer, impedance measurement using an Agilent vector network analyzer, and LCR measurement results are in excellent agreement with analytical and FEA analysis

using IntelliSuite. The frequency analysis exhibits high electromechanical coupling coefficient of 0.66 at a low bias voltage of 20V and high uniformity.

A successful measurement of the lower drift of the center frequency 0.32% and higher coupling coefficient verifies the hypothesis that the excellent electrical, structural, and processing characteristics of BCB is a viable option to mitigate the dielectric charging and improve the transduction efficiency of CMUTs.

DEDICATION

I would like to dedicate my dissertation work to my parents. This achievement of mine would not have been possible without their support and prayer. I am grateful to Almighty for blessing me with parents like you who have sacrificed a lot to provide me with the best education. I think I was able to make you proud.

I would like to dedicate this work to my elder brother and sister who have never left my side and are very special and dear to me.

I would also like to dedicate this dissertation to my lovely nieces and nephew. They have been my best cheerleaders.

ACKNOWLEDGEMENTS

To my supervisor, Prof. Dr. Chowdhury. Thank you for giving me the opportunity to carry out my dissertation work under your supervision and for supporting me with all the equipment/materials, and facility access. Without you, I would not have been able to execute my ideas and finish the project. To my committee members, Prof. Dr. Khalid, Prof. Dr. Muscedere and Prof. Dr. Maeva. Thank you for all the comments and suggestions on my project. To Prof. Dr. Yeow, thank you for agreeing to be the external reader and traveling to Windsor for my defense. The CMUTs in this dissertation were fabricated in the Nanofabrication Facility, Western University, London, ON. I would like to thank Dr. Bakhtazad and Todd Simpson who have helped me with the cleanroom facility. Dr. Gerardo and Prof. Dr. Cretu from UBC to allow and help me with the characterization. Jennifer, Ashley and Mariusz for the support from CMC. Sharon from GLIER Department for giving me the opportunity to use the SEM equipment and Terry from Delvotec for technical support with the wirebonder. Prof. Dr. Rashid for allowing me to use the RCIM lab facility. I especially want to say thank you Frank, Andria and Lorraine for your administrative support. Last but not the least, I would like to acknowledge the support, motivation, and idea from my lab mates, colleagues, and friends. Weiying, Arjunan, Sujitha, Varshitha and Sreejit, I was lucky to have you guys being there for me throughout my Ph.D. journey.

TABLE OF CONTENTS

DECLARATION OF ORIGINALITY	iii
ABSTRACT	iv
DEDICATION	vi
ACKNOWLEDGEMENTS	vii
LIST OF TABLES	xi
LIST OF FIGURES	xii
LIST OF APPENDICES	xvii
LIST OF ABBREVIATIONS	xviii
NOMENCLATURE	xx
Chapter 1 INTRODUCTION	1
1.1 <i>Motivation</i>	2
1.2 <i>Problem Statement</i>	4
1.3 <i>Existing Solutions and Their Limitations</i>	7
1.4 <i>Research Objective</i>	9
1.5 <i>Proposed Solution Approach/ Hypothesis</i>	10
1.6 <i>Contributions & Publications</i>	11
1.7 <i>Dissertation Outline</i>	13
Chapter 2 ULTRASOUND IMAGING AND CMUT OVERVIEW	16
2.1 <i>Ultrasound Imaging</i>	18
2.2 <i>Phased Array</i>	22
2.3 <i>Different Modes of Image Display</i>	26
2.4 <i>Piezoelectric Ultrasonic Transducer Probe</i>	28

2.5	<i>Capacitive Micromachined Ultrasonic Transducer</i>	31
Chapter 3 CMUT PHASED ARRAY DESIGN		39
3.1	<i>Ophthalmic Anterior Segment Imaging</i>	40
3.2	<i>Specifications to Safe Ophthalmic Ultrasound Imaging</i>	41
3.3	<i>Phased Array Design Methodology</i>	42
3.4	<i>Simulation based Array Performance Analysis</i>	49
3.5	<i>Discussion</i>	52
Chapter 4 CMUT CELL DESIGN		56
4.1	<i>Design Methodology</i>	56
4.2	<i>Center Displacement and Deflection Profile</i>	59
4.3	<i>Collapse Voltage</i>	63
4.4	<i>Resonant Frequency, Drift Analysis and Coupling Efficiency</i>	65
4.5	<i>Capacitance Analysis and Sensitivity</i>	68
4.6	<i>Dynamic Analysis</i>	70
4.7	<i>Discussion</i>	73
Chapter 5 FABRICATION OF LINEAR PHASED CMUT ARRAY		77
5.1	<i>Oxide Layer Deposition</i>	81
5.2	<i>Realization of BCB Diaphragm</i>	81
5.3	<i>Top Metallization and Routing</i>	84
5.4	<i>BCB Cavity Formation</i>	85
5.5	<i>Preparation of the Carrier Wafer and Realization of Insulation Layer</i>	88
5.6	<i>Adhesive Bonding of the Wafers</i>	90
5.7	<i>Layer Transfer</i>	91
5.8	<i>Metallization of Contact Pads and Dicing</i>	92
5.9	<i>Die Singulation</i>	93

5.10	<i>Discussion</i>	93
Chapter 6	FABRICATION VALIDATION AND CHARACTERIZATION OF CMUT ARRAY	95
6.1	<i>SEM Inspection and Fabrication Validation</i>	96
6.2	<i>Packaging of the Array and Wirebonding</i>	101
6.3	<i>Static Characterization of the Fabricated CMUT Structure</i>	104
6.4	<i>Experimental Analysis using Laser Doppler Vibrometer</i>	110
6.5	<i>Discussion</i>	114
Chapter 7	PERSPECTIVE, SUMMARY AND FUTURE DIRECTIONS	116
7.1	<i>Perspective</i>	116
7.2	<i>Summary and Discussion</i>	118
7.3	<i>Future Directions</i>	121
7.4	<i>Concluding Remarks</i>	125
	APPENDICES	126
	REFERENCES	128
	VITA AUCTORIS	128

LIST OF TABLES

Table 2.1: Acoustic Impedance Values of Different types of Human Organs.....	20
Table 2.2: Acoustic coefficients of Different types of Human Organs.....	21
Table 2.3: Frequency Specific Ultrasound Imaging Applications.....	22
Table 2.4: Types of Arrays, Structural Configurations and Generated Beam Shapes	26
Table 2.5: Industrially available Ultrasonic Transducer Probes	27
Table 2.6: Fabrication and Performance Comparison between Piezoelectric and CMUT.....	32
Table 2.7: Advantages and Disadvantages of Adhesive Wafer Bonding Technique	34
Table 3.1: Array specifications	48
Table 3.2: Validation of the Design Methodology and Analysis	53
Table 4.1: Material Properties	58
Table 4.2: Sensitivity Parameters Extracted From IntelliSuite™	70
Table 4.3: Design Specifications of a CMUT Cell	73
Table 4.4: Analysis of the Spring Softening Effect on Stiffness and Coupling Coefficient.....	74
Table 5.1: 80% Curing Profile for BCB.....	84
Table 5.2: The 50-60 % Curing Profile for BCB	86
Table 5.3: The 38% Curing Profile for BCB.....	88
Table 6.1: 32 Channel 40 MHz CMUT Array Specifications.....	95
Table 6.2: Comparison of Resonant Frequency Drift in MHz with Time.....	108

LIST OF FIGURES

Figure 1.1. CMUT design with dielectric posts instead of continuous insulating layer as presented in [17].	8
Figure 1.2. CMUT design with spacer and spacing to address the charging issue presented in [18].	9
Figure 2.1. (a) Specular reflection, (b) Non-specular reflection (Scattering), (c) Refraction, (d) Absorption and (e) Transmission of ultrasoundbeam.	19
Figure 2.2. The effect of transducer frequency on penetration depth and resolution of ultrasonic imaging	22
Figure 2.3. Phased array electronically (a) beam steering, and (b) beam focusing in transmit mode	24
Figure 2.4. Phased array electronically (a) beam steering, and (b) beam focusing in receive mode	25
Figure 2.5. Typical components of piezoelectric transducers.	29
Figure 2.6. Working principle of a piezoelectric ultrasonic transducer.	29
Figure 2.7. Typical cross-section of a capacitive micromachined ultrasonic transducer.	32
Figure 2.8. Working principle of CMUT (a) Transmit, and (b) Receive mode.	32
Figure 2.9. Process steps of surface micromachining technique, (a) deposition of insulation/ etach stop layer, (b) deposition and pattern of the sacrificial layer, (c) deposition and pattern of membrane layer, and (d) etching of the sacrificial layer, releasing the diaphragm.	33
Figure 2.10. Process steps of fusion bonading technique, (a) deposition of insulation and sidewall layer, (b) patterning of insulation layer to realize cavity, (c) SOI wafer layer transfer and fusion bond, and (d) wet etching of the silicon substrate and oxide layer to realize the diaphragm and metalization	34
Figure 3.1. (a) Typical linear phased array structure. (b) CMUT array cross-section along the azimuthal direction with three cells in each element	

shown conceptually.....	42
Figure 3.2. (a) Radiation pattern and (b) beam directivity of 16 and 128 elements linear phased array with a pitch of 18.75 μm	44
Figure 3.3. -3dB angular response of a single element	46
Figure 3.4 Near field pressure calculation of 128-elements linear array	47
Figure 3.5. (a) Vantage 128™ simulated pulse echo signal received by the 64th element at 40 MHz (no steering). (b) Spectra in frequency domain showing the -6dB fractional bandwidth as 55%	50
Figure 3.6. (a) Simulated echo signal from object 1 received by (b) element 1, (c) element 64, (d).element 128 at +40° steering angle, (e) echo signal from object 2 received by (f) element 1, (g) element 64 and (h) element 128 at -40° steering angle. The simulation was carried out in Vantage 128 from Verasonics™	51
Figure 3.7. A typical anatomy of an anterior eye segment	53
Figure 3.8. B-scan of a four-wire phantom. (a) Experimental result from 41 MHz Si_3N_4 based linear CMUT array [74], (b) Simulated result from 40 MHz BCB based linear phased array CMUT in Vantage128™	54
Figure 3.9. Synthetic aperture image of a five-wire phantom in B-scan mode by (a) 35 MHz piezo-composite ultrasound transducer array [72], (b) 40 MHz BCB based CMUT linear phased array in Vanatge128™ imaging platform	55
Figure 4.1. (a) A cross-section of the proposed CMUT cells, (b) A single cell structure	58
Figure 4.2. Typical boundary conditions and center deflection of a CMUT unit cell.....	59
Figure 4.3. Comparison of the diaphragm deflection profile under ambient pressure of 101.3 kPa between analytical and FEA simulation result.....	62
Figure 4.4. 3-D FEA deflection result of a 10x10 μm^2 diaphragm from IntelliSuite™	62
Figure 4.5. (a) Collapse voltage of a 10 x 10 μm^2 square diaphragm CMUT cell at 1752 V, (b) 3D FEA diaphragm collapses at pull-in voltage in IntelliSuite™	64

Figure 4.6. Spring softening phenomenon in terms of natural frequency drift as a function of bias voltage	66
Figure 4.7. Mechanical impedance of a CMUT cell diaphragm as a function of frequency	66
Figure 4.8. Matlab based resonance and anti-resonance frequencies extracted from imaginary electrical impedance curve as a function of frequency	67
Figure 4.9. Comparison of a single cell capacitance changes as a function of applied DC bias voltage based on analytical and 3-D FEA model	69
Figure 4.10. Dynamic displacement of a 10 x 10 μm^2 square diaphragm as a function of frequency in IntelliSuite™	71
Figure 4.11. Dynamic settling time of a unit cell (a) applying 1V DC bias and (b) reducing to 0V DC bias in IntelliSuite™	72
Figure 5.1. (a) Thermally grown 1000 nm oxide layer on both sides of the silicon wafer (wafer 1), (b) structural BCB layer deposition for CMUT diaphragm (1500 nm), (c) gold metallization to realize the top electrode and routing traces, (d) BCB layer deposition for interelectrode dielectric spacer (750 nm), and (e) Patterning of BCB layer to create the CMUT cavities.	78
Figure 5.2. (a) Wafer 2 (bottom electrode) cleaning, (b), 200 nm BCB insulating layer realization, and (c), (d) Adhesive wafer bonding of wafer 1 and wafer 2. nm thick gold contact pads	79
Figure 5.3. (a) BCB diaphragm realization by etching the top silicon and oxide layers, (b) realization of contact pad regions by selectively etching the top BCB diaphragm, and (c) realization.of contact pads by depositing gold layer (400 nm).....	80
Figure 5.4. (a) Conceptual top view of the fabricated CMUT array, and (b) magnified cross-section across the azimuthal plane	81
Figure 5.5. Cyclotene™ 3022-35 spin curve for different BCB and Mesitylene ratio.	82
Figure 5.6. (a) Temperature profile, and (b) the corresponding curing level for BCB diaphragm layer.....	83

Figure 5.7. (a) Temperature profile, and (b) the corresponding curing level for BCB layer suitable for bonding	87
Figure 5.8. (a) Temperature profile, and (b) the corresponding curing level for BCB layer deposited on wafer 2	89
Figure 5.9. Temperature (blue line), pressure (black line), and vacuum (red line) profile	90
Figure 5.10. Fabricated arrays after dicing and isopropyl alcohol bath	93
Figure 6.1. Top metallization of a section of a linear array	96
Figure 6.2. Cross-sectional SEM images of the fabricated CMUT elements each consists of 2 CMUT diaphragms along the lateral direction after the adhesive wafer bonding	97
Figure 6.3. Surface topography of a portion of the 40 MHz CMUT linear phased array	98
Figure 6.4. SEM images of (a) 2 μm wide conductive traces to individually access elements, and (b) 150 x 150 μm^2 contact pads for wire bonding	99
Figure 6.5. Optical images of diced diaphragms with cavities underneath	100
Figure 6.6. (a) Silver conductive epoxy part A and part B, and (b) array glued to the base of the package using the epoxy mixture of 1:1 ratio	101
Figure 6.7. (a) Damaged contact pad while wire bonding, and (b) the detached gold pad from the contact pad area along with the 28 μm thin bonded wire	102
Figure 6.8. CMUT contact pads wire bonded to the package using EPOTEK 12670 EE silver conductive epoxy	103
Figure 6.9. Vector Network Analyzer (VNA) setup for electrical input impedance measurement (a) schematic, and (b) experimental	104
Figure 6.10. Real and imaginary electrical input impedance as a function of frequency measured using vector network analyser, applied DC bias 20 V ..	105
Figure 6.11. (a) Series and (b) parallel resonance of the array elements measured using VNA 5061B	106
Figure 6.12. Static capacitance across the array element using LCR meter	107

Figure 6.13. Frequency drift with time for (a) BCB, (b) Silicon and (c) Silicon nitride based diaphragm.....	108
Figure 6.14. Spring softening effect on the frequency as function of bias voltage at 30V, 40V and 50V.....	109
Figure 6.15. Surface topography of a portion of the CMUT array.....	111
Figure 6.16. 60V DC bias deflection of CMUT diaphragms measured using a Polytec MSA-500 laser Doppler vibrometer.....	112
Figure 6.17. 3D snapshot of the out of plane vibration of the CMUT cell diaphragms.....	113
Figure 6.18. Diaphragm displacement as a function of frequency validating the resonance at 10.13 MHz with a peak deflection.....	113
Figure 6.19. Velocity measurement of CMUT diaphragm.....	114
Figure 7.1. (a) 1.5 μm deep 20 μm narrow trench for routing and (b) gold contact pad adhered to BCB layer.....	122
Figure 7.2. (a) 3D design of the probe casing in SOLIDWORKS and (b) 3D printed probe head from PROTO 3000	123
Figure 7.3. 8 layer PCB design of readout module with the CMUT array carrier board.....	123
Figure 7.4. 1.4x1.1 cm^2 two layer PCB designed for breakout module	124

LIST OF APPENDICES

Appendix A. Advanced kinetic model for Cyclotene polymerization	140
--	-----

LIST OF ABBREVIATIONS

CMUT-	Capacitive Micromachined Ultrasonic Transducer
BCB-	Bisbenzocyclobutene
C-V-	Capacitance-Voltage
MEMS-	Micro Electro Mechanical System
RF-	Radio Frequency
PF-	Poole-Frenkel
MOS-	Metal Oxide Semiconductor
PF-	Poole-Frenkel
SEM-	Scan Electron Microscopy
FEA-	Finite Element Analysis
SONAR-	Sound Navigation and Ranging
NDT-	Non-destructive testing
A-mode-	Amplitude mode
M-mode-	Motion mode
PW-	pulse wave
PZT-	lead zirconium titanate
SNR-	signal to noise ratio
VLSI-	Very large signal integration
HIFU-	High intensity focused ultrasound
IC-	Integrated Circuit
PECVD-	Pressure enhanced chemical vapor deposition
IVUS-	Intra-vascular ultrasound system
LASIK-	laser-assisted in situ keratomileusis

TAC-	Transducer array calculation
MI-	Mechanical index
TI-	Thermal index
TIS-	Thermal index for soft tissue

NOMENCLATURE

$Z =$	Acoustic impedance
$\rho =$	Medium density
$v =$	Velocity of sound in the medium
$I_r =$	Reflected ultrasound beam intensity
$I_i =$	Incident ultrasound beam intensity
$Z_1 =$	Acoustic impedance in medium 1
$Z_2 =$	Acoustic impedance in medium 2
$\alpha =$	Attenuation coefficient
$\Delta t_i =$	Relative time delay
$\Delta C_i =$	Relative amplitude weights
$N =$	Number of elements
$D_e =$	Directivity pattern of a single element
$D_a =$	Directivity pattern of an array
$\theta =$	off-axis angle
$r_l =$	lateral resolution
$f_{geo} =$	geometric focal length
$\phi_{-6dB} =$	-6db bandwidth
$n_f =$	near field distance
$\Delta k =$	near field correction factor
$P_x =$	Angular response

$P_{peak} =$	peak rarefaction pressure
$W_0 =$	acoustic power output
$f =$	center frequency
$c_m =$	acoustic speed in the medium
$\lambda =$	wavelength
$A =$	aperture
$D =$	element pitch
$W =$	element width
$L =$	element length
$K =$	kerf
$DOF =$	depth of field
$E =$	Young's modulus
$\tilde{E} =$	effective Young's modulus
$\nu =$	Poisson's ratio
$\sigma =$	residual stress
$\varepsilon =$	relative permittivity
$S =$	conductivity
$w_0 =$	center deflection
$D_{eff} =$	effective flexural rigidity
$P_a =$	ambient pressure
$d_{eff} =$	effective gap height
$t = d_m =$	membrane thickness
$d_i =$	insulation layer thickness

$d_0 =$	airgap height
$V_{collapse} =$	collapse voltage
$a =$	half of the sidelength
$T =$	tensile force
$L =$	diaphragm sidelength
$f_a =$	anti-resonance
$f_r =$	series resonance
$k_T =$	electromechanical coupling coefficient
$C_0 =$	parallel plate capacitance
$C_{ff} =$	capacitance due to fringing field
$C_d =$	dynamic capacitance
$C_{dc} =$	capacitance due to DC bias voltage
$\Delta P =$	acoustic pressure
$V_0 =$	operating voltage
$k_s =$	spring softening
$k_u =$	stiffness during unbiased condition
$k_b =$	stiffness due to biased condition
$P_{out} =$	generated output pressure
$\text{Re}(Z_m) =$	real value of medium impedance
$\omega =$	frequency in radian
$I =$	generated current

The global market for ultrasonic equipment should reach \$31.6 billion and \$54.5 billion in 2016 and 2021, respectively, reflecting a five-year compound annual growth rate (CAGR) of 11.5 %. As a segment, technology encompassing ultrasonic motors/actuators, along with spares and consumables, tops all growth rates with a five-year CAGR of 13.1 percent [1]. The medical field has taken to ultrasonic and allied equipment in a big way, with newer applications coming up frequently in various fields. The diagnostic ultrasound is a booming market with use of three-dimensional (3D) and four-dimensional (4D) imaging increasing in many new fields. Similarly, ultrasonic applications in various types of surgical and therapeutic fields are significantly increasing. Because of these key drivers, the medical field offers high potential for growth in ultrasonic applications [1].

The emerging capacitive micromachined ultrasonic transducers (CMUT) technology offers a superior method of ultrasound generation and detection as compared to the conventional piezoelectric transducers. Global research efforts are underway to make this technology available commercially for biomedical diagnostics and non-destructive testing [2]. It has been mentioned that CMUTs are not intended to replace piezoelectric transducers for conventional imaging applications, but that they are the only option in some applications, such as large array integration in medical imaging probes [3].

In this dissertation work, a 40 MHz linear phased CMUT array with 128 elements was designed and fabricated that is suitable for ophthalmic anterior segment imaging. The CMUT cell diaphragm was designed using a low-K, B-staged polymer Bisbenzocyclobutene (BCB). This material was also used to realize the dielectric spacer and insulation layer. The objective of this research work is to reduce the dielectric charging of the existing CMUT array and achieve higher transduction efficiency at comparatively lower bias voltage that would provide a wider dynamic range of CMUT transmit and receive operation. As a verification of the use of BCB to reduce the dielectric charging and improve the transduction efficiency, a 32 channel linear phased array has been fabricated and experimentally characterized. The fabricated CMUT array was also compared in terms of the effect of spring softening and frequency shift to other CMUT arrays based on Si-SiO₂ and Si-BCB which were developed in our lab earlier.

1.1 Motivation

The motivation behind the dissertation work is to reduce the dielectric charging of capacitive micromachined ultrasonic transducer (CMUT) linear phased array. This dielectric charging effect of CMUTs is one of the main concerns when it comes to biomedical application of an ultrasound system adopting CMUT technology [2, 4-9]. Very few research have been carried out so far to address this issue. Investigation is necessary to find a solution to the root cause of the CMUT deficiency due to dielectric charging effect. The presence of ionic contamination, dipole randomization, and trapped charges in the dielectric materials, typically used to realize CMUT diaphragm, lead to dielectric charging. This degrades the

transduction efficiency since the induced polarization reduced the effective bias across a capacitive transducer [10]. Transduction efficiency is directly related to the electro mechanical coupling coefficient. In order to increase the coupling coefficient, CMUTs are operated at higher bias voltage near the collapse region. When a large electric field due to a high DC bias is applied to the device, electric charges are trapped in the dielectric layers. These trapped charges create a shift in the CMUT internal electric field, causing the CMUT resonant frequency to change. Image quality will deteriorate if different elements in a phased array experience different frequency changes [4, 5, 8-9]. In addition, a shift in the electric field could reduce the CMUT electromechanical coupling efficiency and even can cause the device to collapse in a premature way [11].

A simple and cost effective fabrication process needs to be developed that can address the existing limitations, such as wafer bow or crack at high annealing temperature during state of the art CMUT fabrication process [2]. High residual stress of such diaphragms leads to diaphragm warping that alters the vibrational characteristics of the diaphragm and leads to wafer bow or crack during high-temperature annealing process [2]. Single crystal silicon, polysilicon, and silicon carbide have also been used as the diaphragm structural material. High process temperature during fusion bonding as used in some CMUT fabrication processes [11, 21-22] makes the post process CMOS integration complex [11]. Lack of planarization also degrades the bonding quality [23-25]. Additionally, due to the uncertainty with the thickness variation of the SOI device layers (typically $\pm 0.3-0.5$

μm), it is extremely difficult to realize the desired thickness uniformity across all the CMUT cells in an array [22] that drastically affects the imaging quality.

To resolve the issues as mentioned earlier, it is necessary to use a low residual stress material and low charge trapping property over a wide frequency range to realize the structural layer of a CMUT diaphragm. Additionally, the other insulating layers such as the dielectric spacer and the insulation layer at the top of the bottom electrode also need to have minimal trapped charges during operation. To reduce the unwanted charge flow in the dielectric material due to the charge tunnelling phenomenon, the top electrode could be designed beneath the diaphragm material that will increase the effective capacitance change to increase the sensitivity.

1.2 Problem Statement

Typically, CMUTs are fabricated using a surface micromachining technique or a high temperature fusion bonding process [2, 17-19]. Silicon nitride or silicon dioxide are commonly used to realize the dielectric spacer in a CMUT structure. However, both silicon nitride and silicon dioxide suffer from high ionic contamination, trapped charges, and wafer bow or cracking during the high temperature annealing process that eventually degrades the transduction efficiency and leads to device failure [20]. The process of silicon oxidation to grow silicon dioxide introduces trapped charges in the Si-SiO₂ interface due to the interruption of the silicon periodic lattice structure at the Si-SiO₂ interface [21]. These trapped charges occupy energy states in the silicon energy bandgap. There

are also some ionic fixed charges located within approximately 3 nm of the Si-SiO₂ interface that arise when silicon oxidation stops leaving uncompleted silicon bonds at the interface to result in a sheet of positive charges [21]. The oxidation process also introduces mobile ionic charges, typically alkali ions such as Na, K, and other metallic ions with a surface concentration of 10¹² to 10¹³.cm⁻² [22]. The combined effects of all these charge contaminations contribute to dielectric polarization at high electric field originating from the bias voltages due to the motion of the mobile ions. For example, the conductivity of the oxide surface was measured to be 10⁻¹² S after carrying out the cleaning process [23]. Similar trap charges also exist in silicon nitride thin films arising due to the dangling bonds known as K center defects. Excessive charges trapped in those dangling bonds can alter the C-V characteristics of microfabricated capacitor like geometries such as a CMUT or a MEMS RF switch [24]. In [25], a quasi-two-dimensional simulation and experimental verification of the simulation results of the effects of fixed dielectric charge on the actuation of clamped-clamped beams have shown that a sheet of fixed charge in the dielectric layer results in a voltage offset in the C-V curve of the beam. This offset is directly proportional to magnitude of the fixed charge, while the direction of the shift depends on the polarity of the fixed charge. These results were confirmed by measurements showing a shift in the operational voltages of a microwave switch in [24]. During regular C-V measurements of Si₃N₄ samples, it was found that applying a suitable gate bias could easily change the magnitude and sign of charges present in the nitride film. After applying a gate bias of +40 V for 3 minutes prior to taking the C-V measurement, the C-V curve shifted to -11 V.

The net charge density in the nitride film increased by one order of magnitude by applying a positive gate bias. On the other hand, after applying a gate bias of -40 V for the same duration prior to taking C-V measurement, the voltage was shifted to the positive side to +7.5 V [24]. This experiment proved that the K centers present in the nitride film behave as amphoteric defects that can trap both holes and electrons based on the applied external gate bias, thereby, giving a net positive or a net negative charge to the Si_3N_4 film.

Combined effects of different dielectric charging mechanisms subject to a high electric field cause a net polarization of charges due to space charge polarization and dipole polarization effects. The induced polarization reduces the effective bias voltage across a capacitive transducer and degrades the overall sensitivity. Additionally, under high electric field during the operation, charges might tunnel into the dielectric layer following the Poole-Frenkel (PF) movement phenomenon and alter the CMUT operational behavior [7-9]. In [9], charging problems have been investigated using optical interferometer and electrical reflection method. The results indicated that the negative charges diffused from the aluminium electrode into the silicon nitride diaphragm causing a significant decrease in the resonant frequency with time that led to change in the effective electric field in the cavity. These charges alter the C-V characteristics of a CMUT in a similar way as it happens in a MOS capacitor as presented in [6, 21]. Adding a fixed dielectric charge results in a shift in the C-V curve has been shown in [25]. In [28], it has been mentioned that the individual polarization mechanisms have varied dependencies on the frequency of the applied electric field and generally, the

larger the masses involved, the slower the response upon application or removal of a field. In [8], it was observed that the mechanical resonant frequency of a CMUT array decreased by several percent over hours at the same bias voltage. A small frequency shift was observed between amplitude vs. frequency curves representing at $t=10$ s and 2 min when -25V DC bias was applied. The resonant frequency decreased with time, indicating that the charges travelling from the aluminum electrode and into the silicon nitride membrane. It was expected that there would be increased changes for higher DC voltages. Measurements indicated that this is the dominant charging mechanism. Also in [29], capacitance drift was noticed due to charge trapping when the CMUT was operated for a longer period. Electrical charge trapping is a matter of great concern while using a dielectric material for both the diaphragm and insulation layer as it leads to significant deterioration in CMUT performance.

1.3 Existing Solutions and Their Limitations

Even though this dielectric charging has been investigated as one of the barriers to commercialization of CMUT technology, very few research have been done to mitigate this issue. In [4], a new CMUT design was proposed with isolation posts as a solution to the charging problems. In this design, one or a few isolation posts replace the isolation layer used to prevent shorting between the CMUT electrodes during operation as shown in Figure 1.1. The height, location, size, and shape of the posts need to meet two criteria: to prevent shorting during the operation, and to make the transverse area of the oxide posts small enough so that charges

trapped in them have a negligible effect on device operation. The silicon diaphragm based CMUT array was fabricated using wafer bonding technique, experimentally

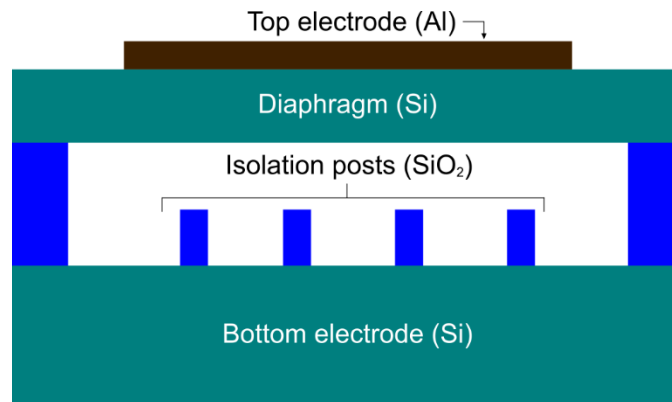


Figure 1.1. CMUT design with dielectric posts instead of continuous insulating layer as presented in [17].

compared with conventional CMUT arrays based on CV curve shifting. There was negligible shifting in the curve for the post based CMUTs. However, the new design was not verified when the diaphragm is also a dielectric material. Silicon diaphragm is observed to change dielectric properties with the change of frequency. As a result, it acts as an insulator at lower frequency and switches to conductor at higher frequency. Frequency based verification is also required in this case to experimentally quantify the effect of using dielectric posts instead of a continuous layer on the transduction efficiency. Realization of the posts requires additional steps during the existing wafer bonding fabrication process as presented in [4].

In [5], highly reliable CMUT cell structure with spacers beneath the membrane and openings in the top electrode was proposed. The proposed CMUT cell structure as shown in Figure 1.2 reduced the dielectric charging effect and suppressed

degradation of dielectric property compared with the conventional CMUT structure. In this case, PECVD-SiO₂ has been used as both the diaphragm and insulating

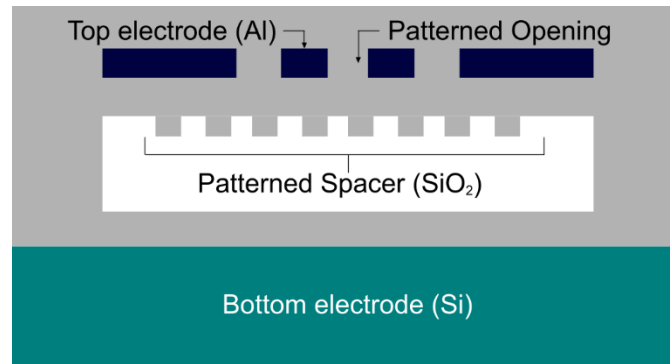


Figure 1.2. CMUT design with spacer and spacing to address the charging issue presented in [18].

layer. Though, the proposed design achieved higher endurance while operating near or beyond collapse voltage compared to the conventional ones. However, the design is yet to be verified in terms of frequency shift and electromechanical transduction efficiency. PECVD-SiO₂ has its own limitation that has been described further in chapter 2. The fabrication process to realize the patterned opening and spacers are complicated, expensive and reduces the overall yield.

1.4 Research Objectives

- Achieve higher electromechanical coupling coefficient at a lower bias voltage
- Reduce the frequency drift.
- Reduce the charging effect
- Increase the dynamic range of CMUT operation

- Reduce the possibility of operating CMUT in non-linear region.
- Improve CMUT reliability.

Overall effect would result in an increase of the transduction efficiency at a very low bias voltage.

1.5 Proposed Solution Approach/ Hypothesis

In [10, 30], a low-k dielectric that has been derived from B-staged bisbenzocyclobutene (BCB) and commercialized by the Dow Chemical Company [30] under the trade name Cyclotene 3000™ has been used as the dielectric spacer to mitigate the effects of electrical charging. In contrast to polyimides, which are also often used as thin film layers, BCB has few advantages. One of them is that BCB has very low ionic contamination of maximum 10 ppm [31]. Distilling process can even reduce the ionic contamination to ppb level [31-33]. The mobile ions caused from dangling bonds can be further reduced by using adhesion promoter AP3000 while the spin coating on silicon [34]. The non-polar chemical structure of BCB leads to low dielectric constant ($\epsilon_r = 2.65$) and a high breakdown voltage ($530 \text{ V} \cdot \mu\text{m}^{-1}$) in combination with a low water uptake ($< 0.2 \%$) [31-36]. BCB is highly cross-linked, based on the small monomer, which leads to higher thermal stability in comparison to the cure temperature [35-36]. It also leads to a complete isotropic behavior of the polymer film [34]. No volatile emission has been observed during the curing process and the products from ring opening reaction are non-polar hydrocarbons [35]. On the other hand, the long-chain characteristic of the polyimide leads to a higher elongation at break, which is an important factor

in reliability [36]. A low residual stress of 28 MPa enables BCB to be deposited at a low-temperature process to minimize wafer bow and cracking issues associated with high residual stress [37-40]. The polymerization reaction of the BCB does not emit any volatile by products [31, 33], resulting in low cure shrinkage (< 5 %). Furthermore, BCB also is an excellent low temperature adhesive wafer bonding agent with a fracture strength as high as silicon, low thermal loss, excellent stability for a wide range of frequency, and high level of planarization [30, 37-41]. The good planarization properties also make BCB attractive for 3D and adhesive bonding [29, 42-43]. These exceptional electrical, mechanical and thermal properties make BCB a suitable and preferable choice to fabricate the diaphragm of a CMUT. Experimental results published in [6] verified that CMUTs fabricated with BCB as the dielectric spacer exhibit better transduction efficiency. Thus, it can be safely argued that a BCB based diaphragm bonded with BCB based dielectric spacers as realized in [9, 29] would enable to fabricate high performance CMUTs with better electrical and mechanical properties to minimize electrical charging effects while achieving excellent structural, operational and processing benefits. Realization of the top conductive electrode beneath the diaphragm can reduce the polarization effect in the dielectric under high electric field.

1.6 Contributions & Publications

- Use of BCB as the diaphragm material in CMUT design and fabrication
- Simple fabrication process using adhesive wafer bonding technique

- Reduced electrical charging effect (most demanding factor in CMUT considered by one of the pioneers in industrialization of CMUT technology [4])
- Superior transduction efficiency in terms of improved electromechanical coupling coefficient by 53.9% from [26] at 1.76% of the collapse voltage
- Lower frequency drift 0.11% after continuously operating for 24 hours
- Easier and low cost implementation of both CMUT 1D and 2D arrays
- Enables reproducibility in different sizes and shapes to meet the specification of different kinds of ultrasonic diagnostic imaging and therapeutic applications

Journals and conference papers related to this dissertation are listed as follows:

- i. **R. Manwar**, T. Simpson, A. Bakhtazad and S. Chowdhury, "Fabrication and Characterization of a High Frequency and High Coupling Coefficient CMUT Array," in *Microsyst. Technol.*, Springer, November 2016, doi:10.1007/s00542-016-3225-4.
- ii. **R. Manwar** and S. Chowdhury, "Experimental Analysis of Bisbenzocyclobutene Bonded Capacitive Micromachined Ultrasonic Transducers," *MDPI Sensors: Integrated Sensor Arrays and Array Signal Processing*, vol. 16(7), no. 959, June 2016.

- iii. A. Bakhtazad, **R. Manwar** and S. Chowdhury, "Fabrication and characterization of sealed cavities realized by adhesive wafer bonding with dry etched Cyclotene™," *Microsystem Technologies*, 2015 pp. 2435-2442
- iv. **R. Manwar** and S. Chowdhury, "40 MHz high coupling coefficient high frequency CMUT array," *Journal of Healthcare Engineering*, Hindawi, London, UK, 2017 (Submitted)
- v. **R. Manwar** and S. Chowdhury, "Characterization of adhesive wafer bonded CMUTs realized from BCB based sealed cavity," 2016 IEEE International Symposium on Circuits and Systems (ISCAS), Montreal, QC, 2016, pp. 2531-2534.
- vi. A. Bakhtazad, **R. Manwar** and S. Chowdhury, "Cavity formation in bonded silicon wafers using partially cured dry etch bisbenzocyclobutene (BCB)," *Circuits and Systems (LASCAS)*, 2014 IEEE 5th Latin American Symposium on, Santiago, 2014, pp. 1-4.
- vii. **R. Manwar**, L. Arjunan, M. Ahmadi and S. Chowdhury, "Resonant frequency calculation of square diaphragms: A comparison," *Circuits & Systems (LASCAS)*, 2015 IEEE 6th Latin American Symposium on, Montevideo, 2015, pp. 1-4.

1.7 Dissertation Outline

The dissertation is organized as follows. Chapter 2 presents the overview of ultrasound imaging technique, commercially available different types of ultrasonic probes for biomedical applications, basic operation of piezoelectric transducers,

and their limitations, CMUT working principle and comparative analysis with piezoelectric counterpart. This chapter also presents the state of the art CMUT designs, their applications and fabrication processes.

In Chapter 3 the array design methodology and the analysis of a high coupling coefficient 40 MHz center frequency 128 channel CMUT array for ophthalmic anterior ultrasonic imaging has been presented. It starts with a brief description of anterior segment imaging and followed by determining the array design parameters, directivity analysis, pulse-echo simulation, beam focusing and steering using Verasonics imaging platform. Later, the simulated results of the array model has been compared with the experimental results of other state of the art array designs to validate the design method.

In chapter 4, individual CMUT cell were designed using a cross-verification platform comprised of MATLAB based analytical and IntelliSuite™ based 3-D electromechanical static and dynamic finite element analysis.

Chapter 5 presents a simple and cost effective fabrication process that has been implemented to realize 1D and 2D BCB based CMUT linear phased arrays.

In chapter 6, fabrication process has been validated using SEM inspection of different sections of the arrays, which are followed by initial characterization using vector network analyzer and discussion on the effect of using BCB as diaphragm material based on the experimental results.

The dissertation concludes with the future direction of this research that includes the possible optimization techniques to overcome the challenges faced during this process and remarks on promising possibilities that are yet to be explored.

Ultrasound Imaging and CMUT Overview

Ultrasound is a form of acoustic energy that propagates as longitudinal wave due to the particle motion or vibration of the medium. The usual frequency range of ultrasound starts beyond the average human hearing capacity (>20 KHz). Animals have been using this acoustic wave for navigation even before it is scientifically established. The evolution of ultrasound technology, a brief history of transducer and a comparison between conventional piezoelectric ultrasound transducer and CMUT is given below.

Ultrasound imaging has its roots in SONAR (SOund Navigation And Ranging), developed in the first half of the 20th century. In 1912, Lewis Richardson patented an ultrasonic underwater detection device [44]. In 1914, Reginald Fessenden detected an iceberg from 3 km away by echo-ranging with a moving-coil transducer. In 1918, Constantin Chilowsky and Paul Langevin detected a submarine at 1.5 km using a piezoelectric transducer. During 1930s many ocean-going liners are fitted with echo-ranging devices. During 1940s sonar is widely used for submarine detection in World War II [44]. After that, non-destructive testing (NDT) and ultrasonic flaw detection process were developed [45]. In 1941, Floyd Firestone invented “The Supersonic Reflectoscope” which used 5 MHz, 1 μ s pulses to locate flaws in materials [46]. In late 1940s, commercial ultrasonic flaw detectors were produced in UK (Kelvin Hughes), Germany (Siemens), Austria (KretzTechnik AG), France (Ultrasonique), Japan (Mitsubishi) [44, 47]. The

application of ultrasound imaging to the human body using flaw detection equipment was followed and developed throughout the second half of the 20th century. In, 1940, H. Gohr and T. Wedekind suggested ultrasound for medical diagnosis specially the tumor detection using echo reflection [44, 47]. In 1942, one of the pioneers of ultrasound, Karl Dussik attempted ultrasonic transcranial brain imaging using 1.2 MHz pulses of 100 ms duration [44, 47]. George Ludwig published a report on the use of ultrasound for diagnosis, which includes a mean value of tissue sound speed of 1540 m/s and recommended an optimal frequency of 1 and 2.5 MHz [48]. In 1953, I. Edler and C. Hertz detected heart motions as the first example of echocardiology [48]. Followed on by Sven Effert in Germany in 1956, Claude Joyner and John Reid at the University of Pennsylvania in 1957 and Chih-Chang Hsu in China, designing their own A- and later on M-mode equipment. Similarly A-mode devices were used in ophthalmologic investigations by Henry Mundt Jr. and William Hughes at the University of Illinois in 1956, Arvo Oksala in Finland in 1957 and Gilbert Baum and Ivan Greenwood in 1955 [49, 50]. These uses were all in the 1950s and largely predated clinical applications in the abdomen and pelvis. In 1962, Shigeo Satomura suggested blood flow measurement using Doppler-ultrasound. In 1965, first real-time scanner was built by Siemens. During 1980s ultrasound screening for pregnant women was introduced. During 1990s tissue harmonic imaging improves image resolution. During 2000s Real-time 3D ultrasound imaging [44, 47].

2.1 *Ultrasound Imaging*

Typically, the ultrasound frequency ranges from 1-60 MHz in the diagnostic and therapeutic imaging applications. The acoustic pulses are transmitted at a certain frequency that travels through the medium. The image is constructed based on the acoustic strength, the time duration and the frequency components of the echo reflecting from the target object [1, 51-53]. The ultrasound pulse interacts differently to the tissues it comes across on its path depending on the extent to which those tissues resist the change in their mechanical impedance due to the incident pulse. This characteristic of individual material is also known as characteristic acoustic impedance, Z (MRayl) and it can be defined as the product of the medium density, ρ and the velocity of sound, v in the medium following (2.1).

$$Z = \rho \times v \quad (2.1)$$

Locations within the organs or tissue at which this acoustic impedance changes is known as acoustic boundaries. Similar to light wave, ultrasound can also be reflected, absorbed, refracted and transmitted at this acoustic boundaries based on the difference in the characteristic acoustic impedance of the adjacent tissues. When a beam of ultrasound strikes the acoustic boundary, a portion of the beam energy is redirected backward to the initial medium as shown in Fig. 2.1(a). Usually, there are two types of reflections occur, (a) specular and (b) non-specular reflection. Specular reflection takes place specially when the acoustic boundary is larger than one wavelength of the incident ultrasound beam and it follows the governing law of the reflection of light [51-53]. The reflected beam is considered

as the echo that is used for image construction and the intensity of the echo is dependent on the angle of incidence as well as on the difference in the acoustic impedances between the medium on both sides of the acoustic boundaries. The difference in acoustic impedances, also known as impedance mismatch, can be used to calculate the intensity of the reflected ultrasound beam following (2.2) where, I_r and I_i represents the reflected and incidence ultrasound beam intensity respectively on the acoustic impedances Z_1 and Z_2 of two different medium.

$$\frac{I_r}{I_i} = \frac{(Z_1 - Z_2)^2}{(Z_1 + Z_2)^2} \quad (2.2)$$

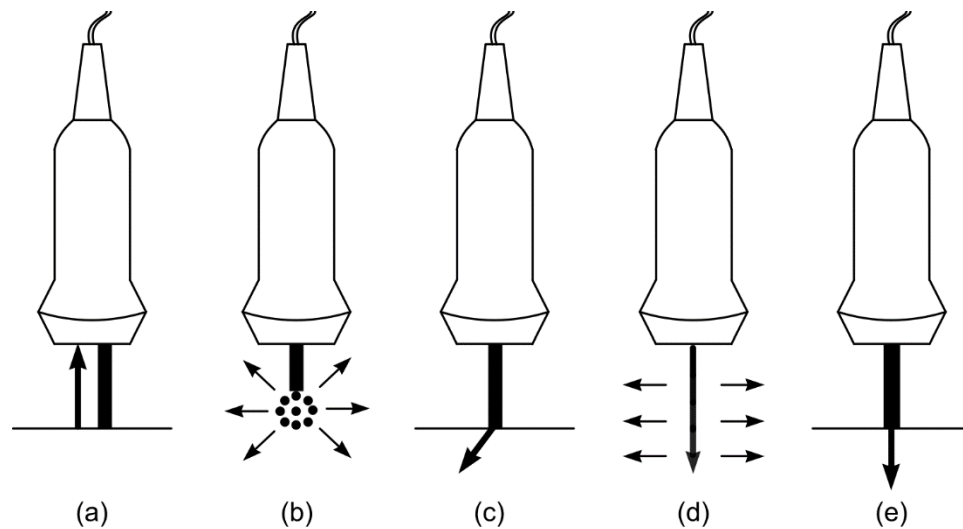


Figure 2.1. (a) Specular reflection, (b) Non-specular reflection (Scattering), (c) Refraction, (d) Absorption and (e) Transmission of ultrasound beam.

In Table 2.1, acoustic impedance of some materials of interest in clinical ultrasound is provided.

TABLE 2.1. ACOUSTIC IMPEDANCE VALUES OF DIFFERENT TYPES OF HUMAN ORGANS.

Material	Acoustic Impedance (MRayl)
Muscle	1.7
Fat	1.38
Brain	1.58
Kidney	1.62
Liver	1.65
Blood	1.61
Soft tissue (average)	1.63
Water	1.48
Bone	7.80
Air	0.004

Non-specular reflection, also known by scattering as shown in Fig. 2.1(b) occurs when the acoustic boundary is smaller than the dimension of the ultrasound beam and irregular in shape. Scattering is frequency dependant and it increases with the increase in operating frequency. Refraction is the change in the direction of the ultrasound beam at the boundary of the two media as shown in Fig. 2.1(c). The velocity of the ultrasound beam changes due to the change in wavelength while the frequency remains the same. Following Snell's law, the intensity of the reflected beam can be evaluated [53]. Unlike specular reflection, refraction does not contribute significantly to form the image. Absorption is the process where a portion of the ultrasound energy is transformed into a different energy mostly heat along its travelling path as shown in Fig. 2.1(d). This process is affected by the viscosity of the medium, relaxation time of the medium particle and the frequency which are linearly proportional to the absorption rate. The overall loss of acoustic energy due to the absorption, reflection and scattering is considered as the attenuation. In soft tissues, 80% attenuation of the ultrasound wave is caused by

absorption. Attenuation is measured in decibels per centimeter of the tissue and is represented by the attenuation coefficient, α of the specific tissue type as provided in Table 2.2.

The rest of the energy is transmitted through the acoustic boundaries as shown in Fig. 2.1(e). In ultrasound imaging, the rapid increase of attenuation as the beam frequency increased implies that very high frequency cannot be employed to examine the tissues located at higher depth from the surface of the transducer. Figure 2.2 shows a trade-off between the penetration depth and the image resolution as a function of frequency based on which different ultrasound frequency is used to clinically examine different segments of the body which is shown in Table 2.3.

TABLE 2.2. ACOUSTIC COEFFICIENTS OF DIFFERENT TYPES OF HUMAN ORGANS.

Material	Attenuation Coefficient (dB.cm ⁻¹ @ 1 MHz)
Muscle	1.3
Fat	0.63
Kidney	1
Liver	0.5
Blood	0.18
Water	0.002
Bone	5

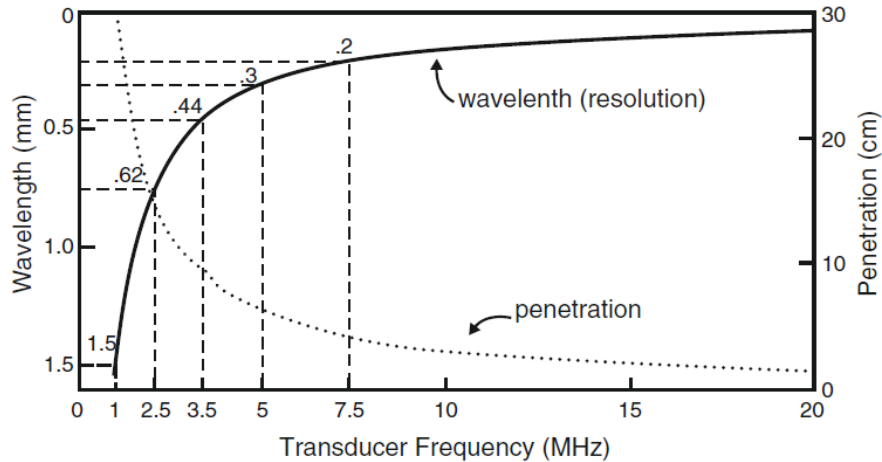


Figure 2.2. The effect of transducer frequency on penetration depth and resolution of ultrasonic imaging.

TABLE 2.3. FREQUENCY SPECIFIC ULTRASOUND IMAGING APPLICATIONS.

Frequency (MHz)	Applicable Imaging Zone
2.5-5	Deep abdomen, obstetric and gynaecological
5-10	General abdomen, obstetric and thyroid, transthoracic
10-12	Superficial veins, superficial masses, musculoskeletal, intracardiac
12-15 and onwards	Superficial structures, ophthalmology, intracoronary

2.2 Phased Array

Based on geometric properties, the ultrasonic transducer arrays have different geometric focal length. To achieve better resolution, this focal point needs to be adjusted according to the position of the target object. Also, if the target object is larger than the active transducer aperture, the echo is scattered in different

directions [53]. For which, the transmitted beam needs to be steered to be able to capture the reflected signal as much as possible. Typically, the transducers are mechanically moved or the orientation is changed to focus and or steer at a desired point. Then a collection of measured signals can be obtained and used to help better determine such quantitative information. However, mechanical scanning is slow and expensive to perform with a single element transducer setup [4, 6, 53-54].

A phased array of ultrasonic transducers for diagnostic imaging unlike single element transducers, is capable of dynamic focusing and steering the beam electronically to achieve higher resolution image and minimum scan time. In a phased array setup, the ultrasonic transducer is composed of an array of small elements, where each element can be separately driven and the response of each element independently received [4, 6, 53-54]. If each of the element is driven in an identical fashion so that the driving electrical pulses travel in unison and all arrive at the piezoelectric elements at the same time then each small element of the array acts effectively like a point source and radiates a spherical wave [54]. These spherical waves combine to form a traveling wave pulse. However, by varying the relative time delays, Δt_i of the driving pulses the ultrasonic phased array is able to electronically steer the sound beam generated in different directions without requiring any motion of the transducer itself as shown in Fig. 2.3(a). With an appropriate non-linear delay law, the same array can also generate a focused sound beam as shown in Fig. 2.3(b). A more complex combination of these delay laws can simultaneously perform both beam steering and focusing [54].

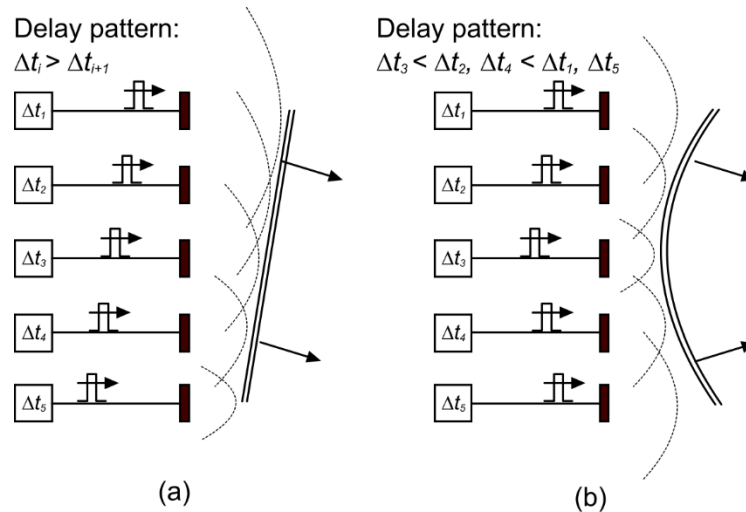


Figure 2.3. Phased array electronically (a) beam steering, and (b) beam focusing in transmit mode.

This flexibility of ultrasonic phased arrays to electronically control the properties of the sound beam can make use of many ultrasonic measurements rapid and cost-effective. Relative time delays for each element can also be used for modifying the characteristics of the signals received by an array. Fig. 2.4(a) shows the case where a plane wave front arrives at an array. As this wave strikes each element of the array in succession, a series of electrical pulses will be generated [54]. If relative time delays, Δt_i , are applied to these received signals so that all of the signals occur at the same time, then they can be summed to generate a single, large output signal. Thus, this reception delay law effectively acts much the same as a single element receiving transducer oriented to face the incoming wave. Similarly, in Fig. 2.4(b), where the incident wave front is curved, relative time delays can be applied on reception to align all the signals from the elements so they also can be summed.

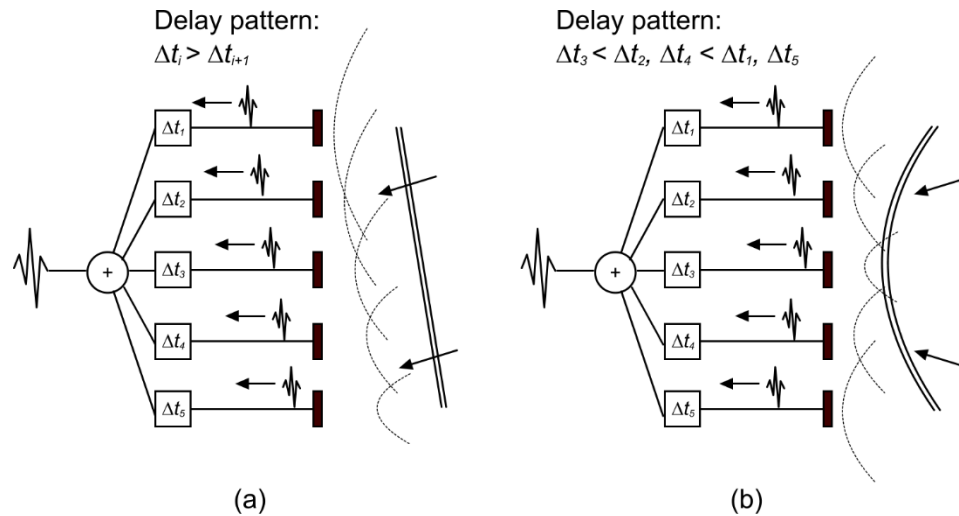




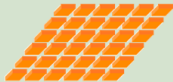
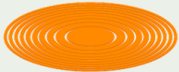
Figure 2.4. Phased array electronically (a) beam steering, and (b) beam focusing in receive mode.

This delay law is then analogous to what would happen with a focused single element transducer on reception [54]. Because an ultrasonic phased array can transmit/receive with each element of the array independently of the other elements, it is possible to apply individual amplitude weights, ΔC_i , to the elements on either sound generation and reception. The ensemble of such amplitude weights is called an apodization law [52-54]. The ability to use general delay laws and apodization laws on generation and reception makes an ultrasonic phased array a very versatile and effective device for conducting ultrasonic tests. Various phased array imaging probes are available based on different configuration of the transducer elements and their beam shapes as shown in Table 2.4 [55].

Commercially available ultrasonic transducer array probes are mostly based on piezoelectric principle. Philips, Hitachi, General Electronics are some of the largest

manufacturers of these probes. In the following Table 2.5, a few of them is provided along with their specifications [56].

TABLE 2.4. TYPES OF ARRAYS, STRUCTURAL CONFIGURATIONS AND GENERATED BEAM SHAPES.

Type of array	Beam shape	Transducer element
1-D	Elliptical	
1.5-D	Elliptical	
2-D	Spherical/elliptical	
Annular ring	Spherical	

2.3 Different Modes of Image Display

Different methods are used to display the acquired information by the transducer. The most common ones are outlined below.

2.3.1. A-scan (Amplitude)

In amplitude or A-scan mode, the signals received for the reflectors is displayed as spikes against the time scale as shown in Fig. 2.5(a). The magnitude of the spike represents the relative echo strength and the time scale provides relative measure of the distance between the transducer surface and the reflector [52-54].

This mode is not capable of the constructing an image. It can only provides one dimensional information.

2.3.2. B-scan (Brightness)

In brightness or B-scan mode, the signals are displayed in terms of dots with varying intensities. The intensity of the dot is a relative measure of the echo size and the time base represents the relative location of the reflector within the scanning region as shown in Fig. 2.5(b). The combined information of different scan lines provide a 2D image of the cross-section through which the beam sweeps [52-54].

TABLE 2.5. INDUSTRIALLY AVAILABLE ULTRASONIC TRANSDUCER PROBES.

	L11-4V	C5-2V	P4-2V	L12-3V	L22-14V
Type	Linear	Convex	Phased array	Linear	Linear
No. of elements	128	128	64	192	128
Resonant frequency (MHz)	8	3.5	3	8.5	18.5
Pitch (mm)	0.3	0.5	0.3	0.2	0.1
Elevation focus (mm)	15-25	60	60	20	6
Probe					

2.3.3. M-scan (Motion)

The motion or M-mode is used to generate an electronic trace of a moving object lying along the ultrasound path Fig. 2.5(c). The transducer is kept fixed at a certain location relative to the moving object and the echo signal will be represented with dots as in B-scan mode. If the object is stationary, it would be traced as a straight line of dots perpendicular to the time base [52-54]. If the object is moving, the trace would show zig-zag or sinusoidal pattern. Typically, M-scan is used to display the cardiac movement.

Other methods of displaying the echo signal are continuous, doppler, harmonic and pulse inversion modes. Doppler mode which is based on the doppler shift can be categorized again as color, continuous, pulsed wave (PW) doppler. Doppler mode is used for imaging the blood flow.

2.4 *Piezoelectric Ultrasonic Transducer Probe*

2.4.1. Components

- a. Piezoelectric transducer: Transmit and receive ultrasound wave
- b. Backing layer: To suppress the rear vibration and shorten the pulse length in order to improve the axial resolution
- c. Acoustic matching layer: To reduce the acoustic impedance mismatch phenomenon
- d. Acoustic lens: To improve the ultrasound wave directivity and focusing [43].

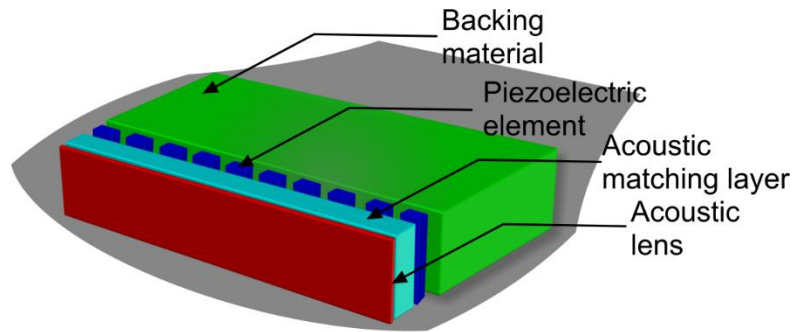


Figure 2.5. Typical components of piezoelectric transducers.

2.4.2. Working Principle

Almost all of the ultrasound based imaging equipment use piezoelectric transducers those are made of expensive single crystal piezoelectric ceramics [1, 10, 57-60]. When a voltage pulse is applied to the piezoelectric crystal, it starts oscillating by repeated expansion and contraction due to the accumulation of charge polarity and generates ultrasound wave. Conversely, an incoming ultrasound wave pressure causes strains in piezoelectric material in turn and generates piezoelectricity. Commonly used materials include lithium niobate, barium or lead zirconate titanate (PZT) because of high conversion efficiency [2].

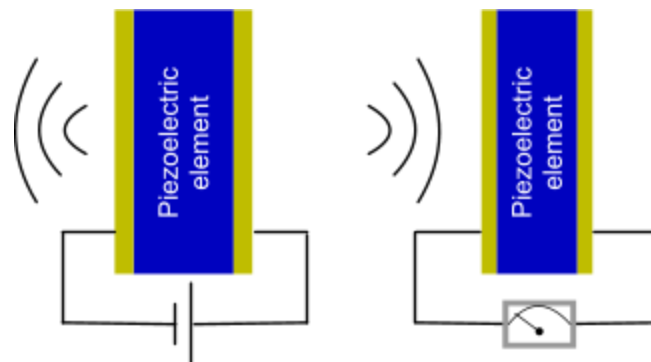


Figure 2.6. Working principle of a piezoelectric ultrasonic transducer.

2.4.3. Limitations

Despite the capability of generating high amplitude while operating at resonance, the piezoelectric transducers have been rated poorly in [1, 10, 57-60] due to following drawbacks:

2.4.3.1. Acoustic Impedance Mismatch

PZT has a typical acoustic impedance of 30MRayl that is much higher than the acoustic medium generally used. For example, acoustic impedance of air, water & vegetable oil is 400 Rayl, 1.5 & 1.391 MRayl respectively [58]. Attenuation due to the impedance mismatch affects SNR. Leads to long ring down of the acoustic pulse that narrows down the bandwidth and in turn degrades the axial resolution. To reduce the mismatch, it requires separate matching & backing layers.

2.4.3.2. Fabrication complexity and challenges

Piezoelectric transducers are usually realized by dicing into elements using saw method or focused laser. Typically the blade widths are more than 15 μm that makes the realization of high frequency array even more complex. Resonant frequency is directly related to the thickness of piezo layer and thereby limiting the operation to a single frequency [1, 59]. Relation between the frequency and element pitch causes tight tolerances to fabricate high frequency 1 & 2D arrays [59]. Narrow cuts significantly reduce the active area of the sensing surface. Even at lower frequency, dicing significantly impacts the uniformity.

2.5 Capacitive Micromachined Ultrasonic Transducer

The capacitive micromachined ultrasonic transducer (CMUT) is a type of microelectromechanical systems (MEMS) device that is constructed using processes similar to conventional VLSI technology to generate and receive ultrasound [2]. As opposed to the conventional piezoelectric principle based ultrasonic transducers, the CMUTs rely on electrostatic principles for ultrasound generation and reception. These transducers consume low power, low noise, offer excellent electrical and thermal stability, and a wider fractional bandwidth [1, 57-59]. Due to these advantages, CMUTs have gained much popularity over the last decade and are considered a potential alternative to commercially available piezoelectric transducers for biomedical imaging, non-destructive testing, high intensity focused ultrasound (HIFU), automotive collision avoidance, and parking assistance applications [11, 17, 59-61]. A typical CMUT geometry is constructed to have a square, circular or hexagonal diaphragm that is supported on a fixed backplate by an insulating layer enclosing a small cavity filled with vacuum or air. The structure functions as a variable capacitor where one of the electrodes (the diaphragm) is free to move or deform against the other (the backplate) to effect a change in capacitance.

In the transmit mode, a DC bias voltage superimposed with an AC signal of desired frequency is applied to the CMUT geometry to generate a time varying electrostatic force that causes the diaphragm to vibrate to create ultrasonic vibration in the

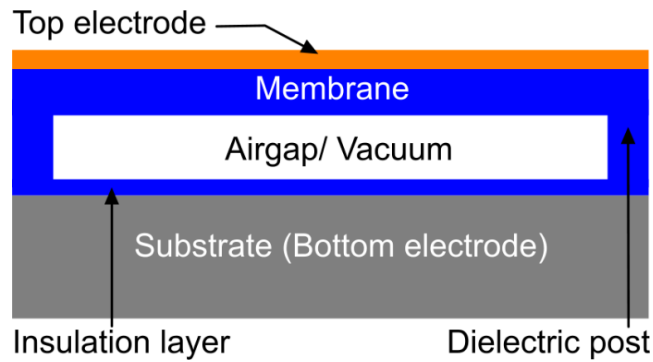


Figure 2.7. Typical cross-section of a capacitive micromachined ultrasonic transducer.

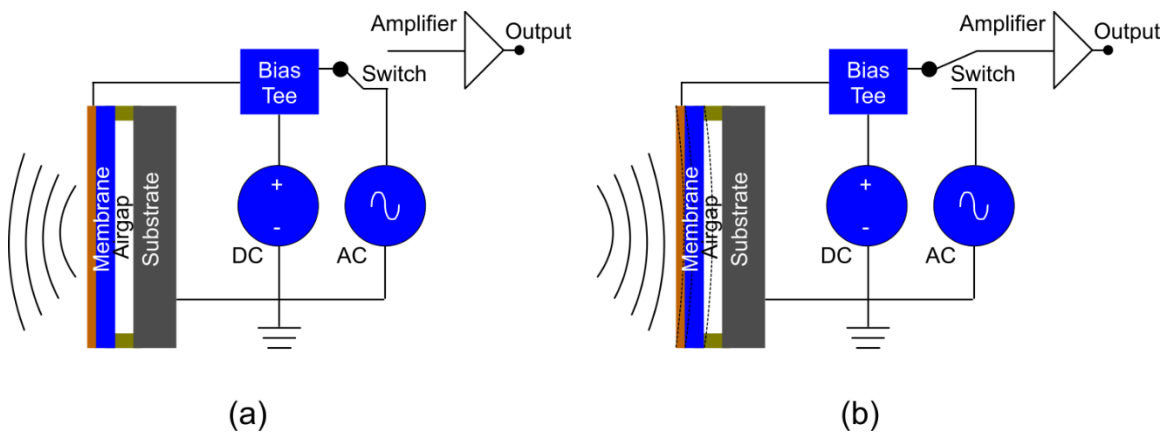


Figure 2.8. Working principle of CMUT (a) Transmit, and (b) Receive mode.

TABLE 2.6. FABRICATION AND PERFORMANCE COMPARISON BETWEEN PIEZOELECTRIC AND CMUT

	Piezoelectric	CMUT
Fabrication technology	Ceramic	MEMS
Array fabrication	Difficult & expensive	Easy & low cost
Frequency Range	Relatively narrow	Broad
Bandwidth	Moderate & matching layers required	Wide
Uniformity	Moderate	High
Thermal stability	Low	High
IC integration	No	Yes
Output pressure	High	Improving

surrounding medium. When the CMUT is exposed to an incident ultrasound wave, the sound pressure deforms the diaphragm (top electrode) towards the fixed bottom electrode. The resulting change in capacitance is converted into an electrical signal using a suitable microelectronic circuit.

2.5.1. Typical Fabrication Processes

2.5.1.1. Surface Micromachining

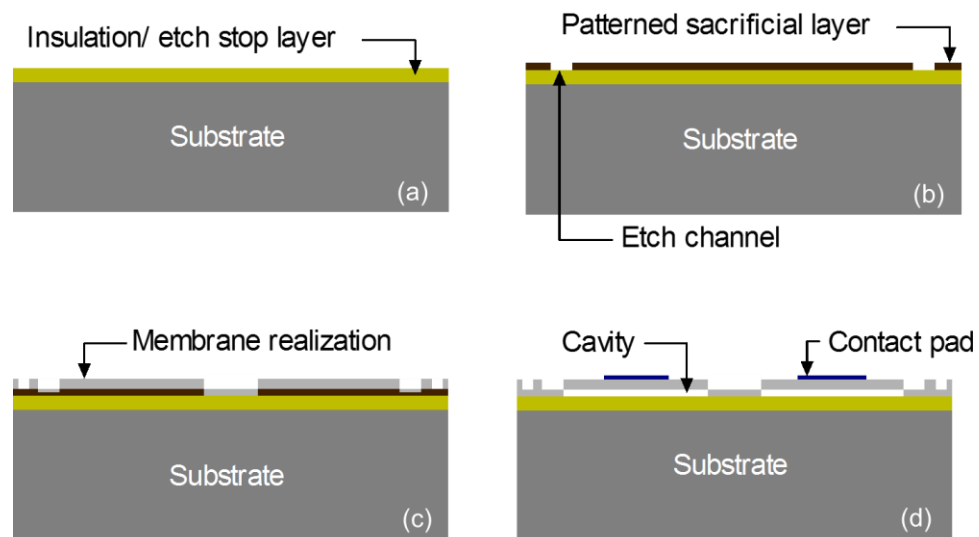


Figure 2.9. Process steps of surface micromachining technique, (a) deposition of insulation/etch stop layer, (b) deposition and pattern of the sacrificial layer, (c) deposition and pattern of membrane layer, and (d) etching of the sacrificial layer, releasing the diaphragm.

2.5.1.2. Fusion Bonding

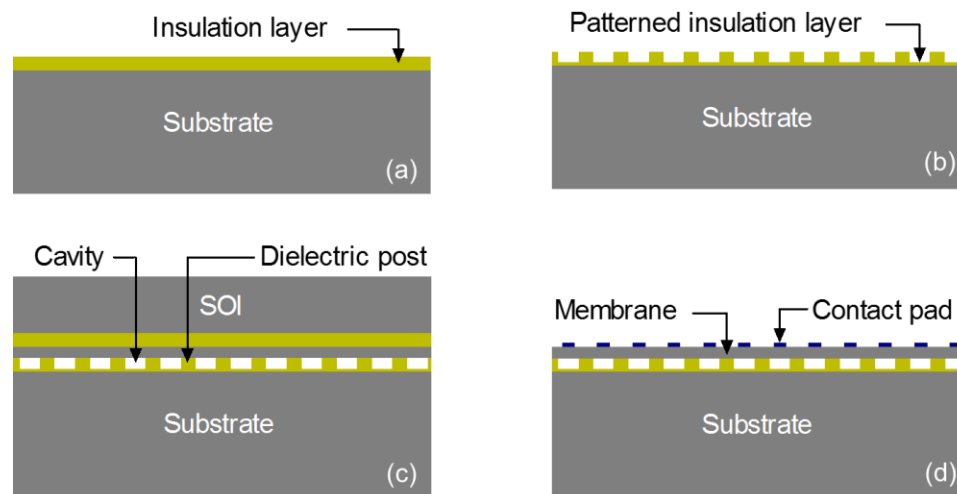


Figure 2.10. Process steps of fusion bonding technique, (a) deposition of insulation and sidewall layer, (b) patterning of insulation layer to realize cavity, (c) SOI wafer layer transfer and fusion bond, and (d) wet etching of the silicon substrate and oxide layer to realize the diaphragm and metalization.

2.5.1.3. Adhesive wafer bonding technique

Adhesive bonding (also referred to as gluing or glue bonding) describes a wafer bonding technique with applying an intermediate layer to connect substrates of different materials [62]. The pros and cons are provided in the following Table 2.7.

TABLE 2.7. ADVANTAGES AND DISADVANTAGES OF ADHESIVE WAFER BONDING TECHNIQUE

Advantage	Disadvantage
Feasibility in vacuum	Limited long term stability
Simple and low cost process	Limited temperature stability
Low bonding temperature	Relatively low bond strengths
Absence of electrical voltage/ current	Penetration of moisture
Higher surface uniformity	
Less contamination	
High transparency	

2.5.2. State of the Art

Hitachi Corporation announced the first successful commercialization of a CMUT-based 1.5D array for conventional 2D cross-sectional imaging [60]. Philips identified the advantages of CMUTs over the conventional piezoelectric transducers mainly as the reduced production costs and improved bandwidth and imaging quality. Fraunhofer IPMS concluded that CMUTs should not be seen only as a replacement for piezoelectric transducers for conventional imaging applications, but they are the only option in some applications (integrated diagnostic and therapeutic capabilities) [11]. A 7 MHz linear array with 40 μm diameter CMUT cells was presented in [17] for imaging of an echographic cyst phantom immersed in a uniform parenchyma mimicking the human body. Sacrificial release process has been used to realize 64 elements array where Chromium acted as sacrificial layer. PECVD Silicon Nitride was used to realize the diaphragm and insulation layer. A 3.3 mm long 128 element wafer bonded 1-D CMUT array was used with commercial scanners to obtain clinical images which was compared to equivalent piezoelectric transducer array in [61]. Demonstrated an improved resolution with better definition of fine structures in the carotid artery and the thyroid gland. -6dB bandwidth of 110% at 6 MHz had been realized using sacrificial release process. A low frequency CMUT array was also presented using patterned Silicon wafer fusion bonding process for underwater imaging in [17]. The design had resonant frequency at 270 KHz with 128 elements. Silicon and Silicon dioxide had been used as the membrane and insulation layer respectively. A 2-D 16x16 array with 5 MHz resonant frequency has been presented for volumetric 3-

D imaging in [17]. Through wafer interconnects and flip chip bonding using gold bump has been utilized for electronic integration. A 1.15 mm diameter 64 elements annular ring array with resonant frequency at 13 MHz for Intra-Vascular Ultrasound (IVUS) was presented in [63].

2.5.3. Limitations

2.5.3.1. Drawbacks of surface micromachining process

- ❑ Breakdown of large membranes during wet release process using poly-silicon as sacrificial layer, especially for rectangular membranes due to high compressing stress
- ❑ LPCVD Silicon Nitride as sacrificial layer suffers from poor etch selectivity and results varying membrane thickness
- ❑ PECVD process to deposit SiO_2 as sacrificial layer and Si_3N_4 as membrane also suffers from poor etch rate selectivity that makes the membrane fragile and lowers the reliability
- ❑ Stiction is a common issue while realizing large membrane and small cavity height in sacrificial release process [2].

2.5.3.2. Drawbacks of using silicon as membrane

- ❑ Lack of ability to control the resistivity of Silicon makes it difficult to selectively make silicon conductive
- ❑ The top electrode cannot be patterned to reduce the parasitic capacitance if the membrane is not selectively made conductive

- ❑ Silicon as membrane adds complexity while modeling the CMUT as it switches the conductivity with the change in frequency [2]
- ❑ When the surrounding environment is conductive, the top electrode suffers from shorting and electrolysis.

2.5.3.3. *Drawbacks of using Si_3N_4 & SiO_2*

- ❑ For high frequency applications, membrane sealing using Si_3N_4 requires long channels with reduced channel height.
- ❑ As a result, efficient sealing will end up with loss of active area, reduced output pressure and sensitivity
- ❑ Wafer bow and crack are common phenomenon for SiO_2 based dielectric posts during high temperature annealing process [17]
- ❑ The quality of wafer bonding depends on the surface roughness and flatness which is a concern for Si_3N_4 based membrane

2.5.3.4. *Dielectric breakdown, charging & front-end electronics integration*

- ❑ Dielectric charging at high voltage is one of the prime concern for SiO_2 and Si_3N_4 based insulation and dielectric posts due to high ionic contamination, dipole polarization, trapped charges
- ❑ These trapped charges do not contribute to the overall capacitance but may affect the DC operating point [2]

- ❑ The charges trapped in the insulation layer alter the electric field in the cavity, changes the static force of the membrane thus changes the operating point and make the CMUT operation unstable
- ❑ Etch holes reduces the fill-factor to a great extent which eventually contributes to higher parasitic capacitance [9]
- ❑ Front-end electronics integration is still an issue because of high complexity, lengthy process and overall lower yield percentage due to flip-chip bonding [64].

Despite generating high amplitude ultrasound pressure, these transducers suffer from high acoustic impedance mismatch that degrades the performance in terms of signal to noise ratio and bandwidth. For which, CMUTs are considered to be a promising alternative to the conventional ones especially in high frequency high resolution ultrasonic imaging application. Higher frequency (>20MHz) provides improved axial and small lateral resolution that enables to generate images of subsurface structures at the cost of penetration depth. High frequency ultrasound imaging can be useful in the field of ophthalmology, dermatology, and odontology for pre-clinical applications. Conventional diagnostic equipment yield valuable information concerning the surfaces of ocular tissues, but provide little information about subsurface structures. The clinically important tissues in the anterior segment are located within 2-4 mm of the surface of the eye, this imaging problem is an ideal application for high-frequency ultrasound.

High-resolution ultrasonic imaging is mostly dependent on the realization of high frequency ultrasound transducers with high coupling efficiency. Higher frequency (>20MHz) provides improved axial and lateral resolutions that enable to generate high quality images of subsurface structures. However, the penetration depth is immensely affected due to the exponentially increased level of attenuation as a function of ultrasound travelling distance in human tissues. High frequency ultrasound imaging can be useful in the field of ophthalmology, dermatology, and odontology. In addition, intravascular, intra-articular and small animal imaging for pre-clinical applications has demanded the development of efficient high frequency ultrasonic transducers. The eye presents a microcosm of tissue types in terms of acoustic properties; they include the anechoic vitreous humor, the highly absorptive ocular lens, the thin (150- μ m) retina, and pathologic structures (eg, choroidal melanomas) with complex internal structures [67]. The ophthalmoscope, slit lamp, and Gonioscope are the standard instruments for visualizing the anterior segment of the eye [65, 66]. These instruments yield valuable information regarding the ocular tissue surfaces but provide little information about subsurface structures. The most important difference between ophthalmic requirements and those of other specialties is the need to examine small structures. This requires the use of higher frequencies, which are practical because the eye is superficial, and its chambers contain low-absorption, water like ocular humors [67]. Since all

the clinically important tissues in the anterior segment are located within a few millimeters of the surface of the eye, this imaging problem is an ideal application for high-frequency ultrasound [65, 66].

3.1 Ophthalmic Anterior Segment Imaging

In the early 1970s, several groups developed relatively simple, reliable systems for routine clinical use. A manually controlled scan unit was developed by Coleman et al. [68]. Higher frequency transducers were developed to provide improved resolution of optical components such as the cornea, lens, and anterior segment. Pavlin et al [69] introduced a 50-MHz instrument using a polyvinylidene difluoride transducer and a sector scanner that provided excellent definition of the segments of the anterior segment of the eye. This scanner is commonly known as ultrasonic biomicroscope. A 50 MHz transducers in an arc scan mode maintains approximately normal angles of incidence over the entire surface of the specular cornea known Artemis system [70]. This permits very high definition over the entire anterior segment used in conjunction with digital processing. Arc scans have provided highly detailed maps of the thicknesses and local radii of curvature of the 50- μm corneal epithelium and 500 μm corneal stroma. Such maps have helped to plan and evaluate corneal sculpting procedures such as LASIK [67].

Commercially available high frequency ultrasound imaging systems are using single element transducers mechanically driven from 20-50 MHz [70]. These transducers suffer from the small depth of field and lower frame rate that limits the image resolution near the geometrically fixed focus [71]. Current researchers are emphasizing on array technology that offers electronic dynamic focusing on

improving the resolution and reducing the scan time. High frequency transducer arrays are presented in [70-73] based on piezoceramic or piezoelectric polymers. A high-resolution 50 MHz multi-element transducer was developed by VisualSonics Inc. Toronto, ON, Canada [70, 73]. However, achieving the required dimensions such as small element pitch and narrow kerf to avoid grating lobes and realize the small thickness of the active material for high frequency application is a stringent challenge to fabricate piezoelectric ultrasonic transducers [74]. Acoustic impedance mismatch and lower thickness mode coupling coefficient are also dominant factors for degraded performance of the piezoelectric transducers [72].

3.2 Specifications to Safe Ophthalmic Ultrasound Imaging

A phased array of ultrasonic transducers for diagnostic imaging as shown in figure 3.1, unlike single element transducers, is capable of dynamic focusing and steering the beam electronically to achieve higher resolution image at minimum scan time. This type of array is usually designed to have a certain aperture size, element pitch, elevation focus, operating frequency, and bandwidth. Arrays with larger aperture size generating shorter pulses can improve the axial resolution and narrow beam width can provide better lateral resolution. At the same time, element pitch should be at least equal or less than half of the wavelength to avoid grating lobes. According to [75], the peak rarefaction pressure of the diagnostic ultrasound generated from a transducer array can be in the range of 0.5-5 MPa with maximum acoustic power in the range of 4-256 mW. The mechanical and thermal index should be in the range of 0.2-1.7 and 0.5-4.1 respectively as reported in [75]. For

ophthalmic application the maximum attainable derated spatial peak time average intensity should be less than or equal to 50 mW.cm^{-2} [76]. According to the guidelines of safe use ultrasound [76], for ophthalmic devices, the maximum attainable value for the thermal index should be less than or equal to 1, the maximum attainable value of the mechanical index should be less than or equal to 0.23.

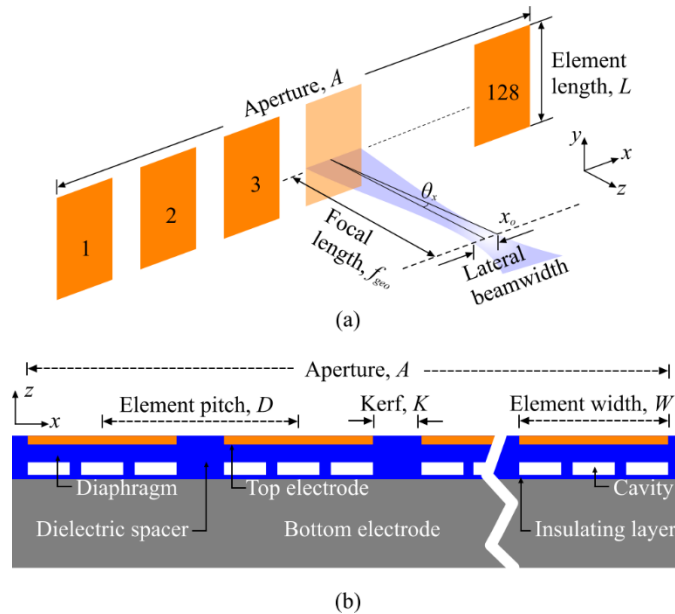


Figure 3.1. (a) Typical linear phased array structure. (b) CMUT array cross-section along the azimuthal direction with three cells in each element shown conceptually.

3.3 Phased Array Design Methodology

The emission performance of ultrasonic transducers is related not only to the properties and status of the medium, but also to the structural parameters of the transducers [77-79]. For the target ophthalmic application, 40 MHz center frequency has been determined to be optimal considering the aperture size, depth of penetration, and fabrication constraints. To maintain the criteria of avoiding

grating lobes, the element pitch size is chosen to be $18.75 \mu\text{m}$ that equals $\lambda/2$. The gap between two adjacent elements also known as kerf has been decided to be $8.75 \mu\text{m}$ considering the fabrication process constraints and mechanical strength of the spacers to support the diaphragms.

3.3.1. Directivity Analysis and Aperture Size

Typically, the size of cells and the space between each pair of cells are very small, the directivity functions for the designed CMUT require a plane array element to analyze [80]. Based on Huygen's principle, the directivity pattern of a rectangular element was deduced in [80] and can be evaluated using (3.1). A single CMUT element often cannot meet requirements of directivity function or generate sufficient ultrasound power. The directivity pattern of the linear array with N number of elements can be expressed as (3.2).

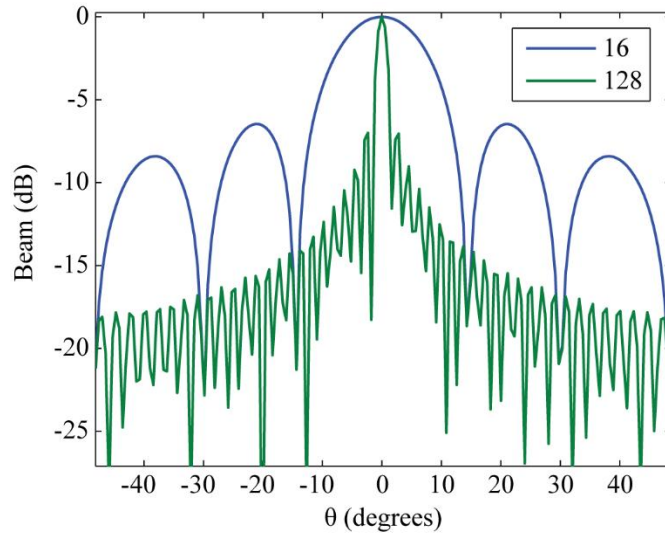
$$D_e(\theta) = \left| \frac{\sin\left(\frac{\pi W \sin(\theta)}{\lambda}\right)}{\frac{\pi W \sin(\theta)}{\lambda}} \right| \quad (3.1)$$

$$D_a(\theta) = D_e(\theta) \left| \frac{\sin\left(\frac{\pi W N D \sin(\theta)}{\lambda}\right)}{N \sin\left(\frac{\pi W \sin(\theta)}{\lambda}\right)} \right| \quad (3.2)$$

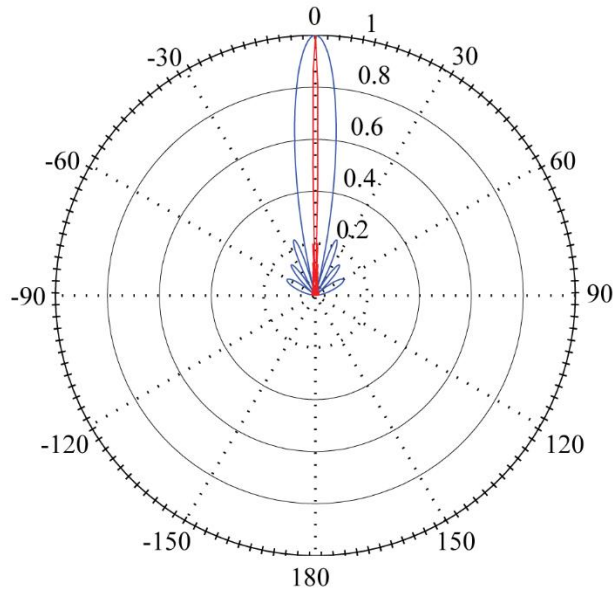
$$A = N \times W + (N - 1) \times K \quad (3.3)$$

Where, θ is the off-axis angle. In this case, number of elements has been chosen to be 128 to improve lateral resolution and that provides an aperture size of 2.41

mm using (3.3) which is optimal for the target application and comparable to the array designs for ophthalmic application presented in [72-74].



(a)



(b)

Figure 3.2. (a) Radiation pattern and (b) beam directivity of 16 and 128 elements linear phased array with a pitch of $18.75 \mu\text{m}$.

The directivity distribution of the array with the proposed design is shown in figure.

3.2 (a) and (b). For comparison purpose the directivity pattern of a 16 element

array has also been shown in figure 3.2 (a) and (b) that clearly shows the effect of number elements on the main lobe width and the increase in the number of sidelobes. Sidelobes can be further reduced by applying appropriate weights following Dolph-Chebyshev and Taylor weighting method that can suppress the side lobes up to -40 dB [80].

3.3.2. Near Field Calculation and Lateral Resolution

Lateral resolution is defined as the ability of the system to distinguish two points in the direction perpendicular to the direction of the ultrasound beam. Lateral resolution is affected by the width of the beam and the depth of imaging. Wider beams typically diverge further in the far field and any ultrasound beam diverges at greater depth, decreases lateral resolution [75-76]. Therefore, lateral resolution is a key design parameter for applications that deal with shallow depths such as ophthalmic anterior segment imaging. Lateral resolution can be expressed as (3.4):

$$r_l = \frac{0.41 \times c_m}{f_{geo} \times \tan(\theta_x)} \quad (3.4)$$

Where, $\theta_x = \sin^{-1}(\lambda/D)$, is the angle of the point x_0 from the normal axis, c_m is the ultrasound speed in the test medium and f_{geo} is the geometric focal length. Lateral resolution can also be approximated based on one-fourth of the -6dB beam width at the focal length, ϕ_{-6dB} where the focal length, f_i can ideally be considered as half of the near field distance, n_f [55].

$$\phi_{-6db} = \frac{\lambda f_i}{A} \quad (3.5)$$

$$n_f = \frac{\Delta k A^2 f}{4c_m} \quad (3.6)$$

Where, near field correction factor, $\Delta k = A/L$ and f is the operating frequency of the array. -6dB depth of field, DOF and -3dB angular response of a single element can be calculated from (3.7) and (3.8) respectively. -3dB angular response of a single element is shown in figure 3.3.

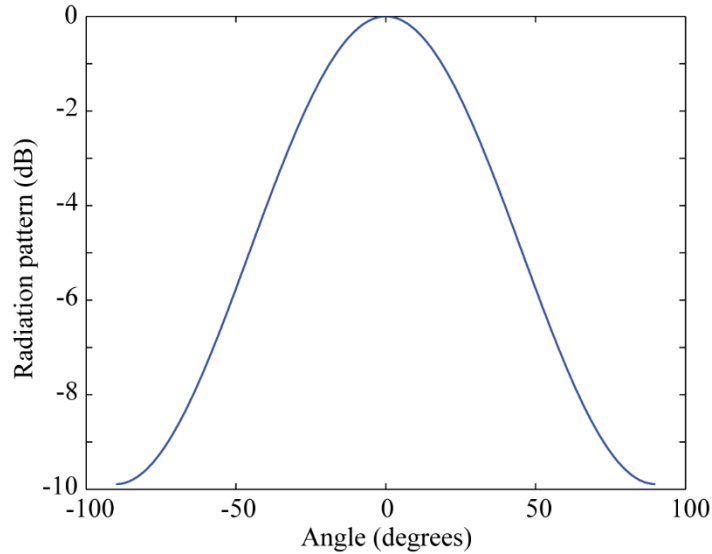


Figure 3.3. -3dB angular response of a single element.

$$DOF = 7\lambda \left(\frac{f_i}{A} \right) \quad (3.7)$$

$$P_x(\theta_x) = \frac{\sin^2 \left(\frac{\pi W}{\lambda} \sin(\theta_x) \right)}{\left(\frac{\pi W}{\lambda} \sin(\theta_x) \right)^2} \cos^2(\theta_x) \quad (3.8)$$

Figure 3.4 shows the generated acoustic pressure as a function of distance from the array surface obtained from the MATLAB Transducer Array Calculation (TAC) Toolbox [81]. Following Figure. 3.4, the maximum pressure at a distance of 2~4 mm from the array surface vary within 1~4 MPa. This pressure corresponds to a peak time average intensity of 45~49 mW.cm⁻² that is within the maximum attainable range for ophthalmic application [75].

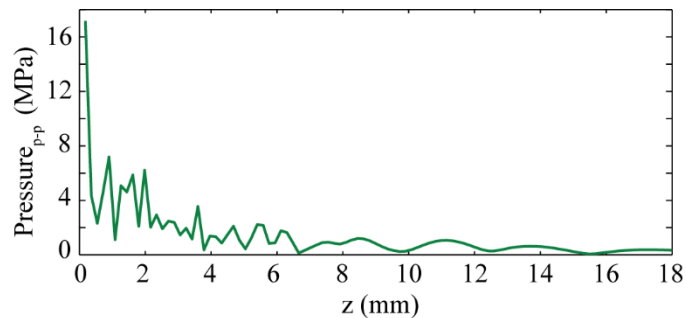


Figure 3.4 Near field pressure calculation of 128-elements linear array.

3.3.3. Mechanical and Thermal Index

Mechanical Index (MI) is intended to indicate the probability of occurrence of inertial cavitation, while Thermal Index (TI) is an indicator of the likely maximum temperature rise in tissues [75]. The soft tissue TI (TIS) is meant to be displayed for examinations in which the ultrasound beam travels a path which is made up principally of homogeneous soft tissue or a soft tissue/fluid path. Mechanical Index can be exposed to the ultrasound field [76]. Both MI and TIS can be defined as (3.9) and (3.10).

$$MI = \frac{P_{peak}}{\sqrt{f(\text{MHz})}} \quad (3.9)$$

$$TIS = \frac{W_0^{0.73} f^{0.62}}{130} \quad (3.10)$$

Where, P_{peak} is the peak rarefaction pressure and W_0 is the acoustic output power based on the acoustic pressure in dB at the target distance. Table 3.1 provides the key parameter values of the target array design.

TABLE 3.1. ARRAY SPECIFICATIONS.

Symbol	Parameters	Value
f	Center frequency	40 MHz
c_m	Medium acoustic speed	1500 m.s ⁻¹
λ	Wavelength	37.5 μ m
N	Number of elements	128
A	Aperture size	2.41 mm
D	Element pitch	18.75 μ m
W	Element width (azimuth)	10 μ m
L	Element length (elevation)	5 mm
K	Kerf width	8.75 μ m
f_{geo}	Geometric Focal length	9.3 mm
DOF	-6dB depth of field	1 mm
MI	Mechanical index	0.16
TIS	Thermal index for soft tissue	0.69

3.4 Simulation based Array Performance Analysis

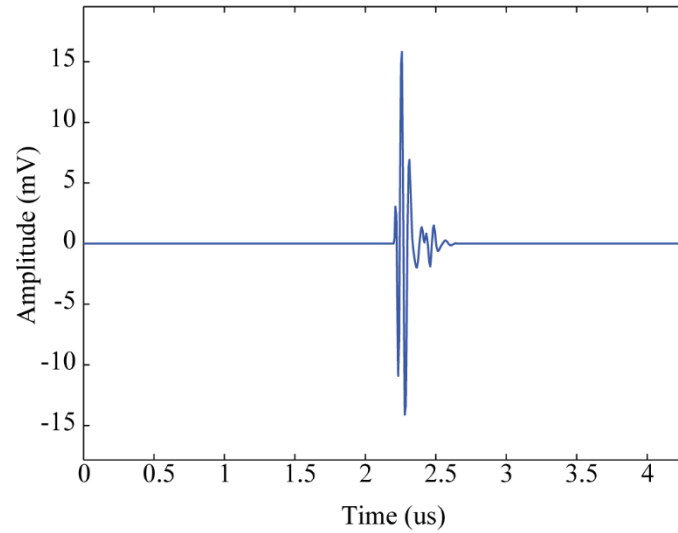
A simulation model of the designed array has been developed in Vantage 128™ system from Verasonics™, an industry standard imaging system for both piezoelectric and capacitive micromachined ultrasonic transducers.

3.4.1. Beam Focusing, Pulse-echo and Bandwidth

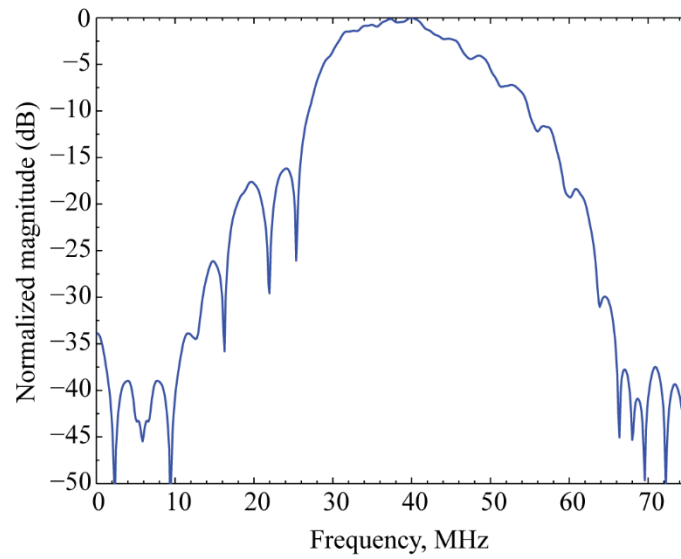
To carry out a pulse-echo transmit mode simulation of the developed array, a simulated object model known as the media point was placed at a distance of 100λ (3.75 mm as maximum depth of anterior segment to avoid computational complexity) from the array model surface without any apodization. Figure. 3.5(a) shows the simulated echo as captured by the 64th array element in time domain after filtering (Butterworth) and averaging. MATLAB Signal Processing Toolbox has been used to process the data. The frequency spectrum of the received signal in Figure. 3.5(a) is shown in Figure. 3.5(b) that shows a -6dB fractional bandwidth of 55%.

3.4.2. Dynamic Beamsteering

Beamsteering and focusing analysis were simulated in Vantage128™ platform to determine the angular response of the array. Object 1 and 2 were placed at a pre-defined focal depth of 50λ (1.87 mm that is considered as the minimum depth of the anterior segment from the array surface) and equally spaced apart from the center of the aperture by 1 mm. The beam was steered $\pm 40^\circ$ and the simulated return signal was received by elements 1, 64 and 128, respectively as shown in Figure. 3.6.



(a)



(b)

Figure 3.5. (a) Vantage 128™ simulated pulse echo signal received by the 64th element at 40 MHz (no steering). (b) Spectra in frequency domain showing the -6dB fractional bandwidth as 55%.

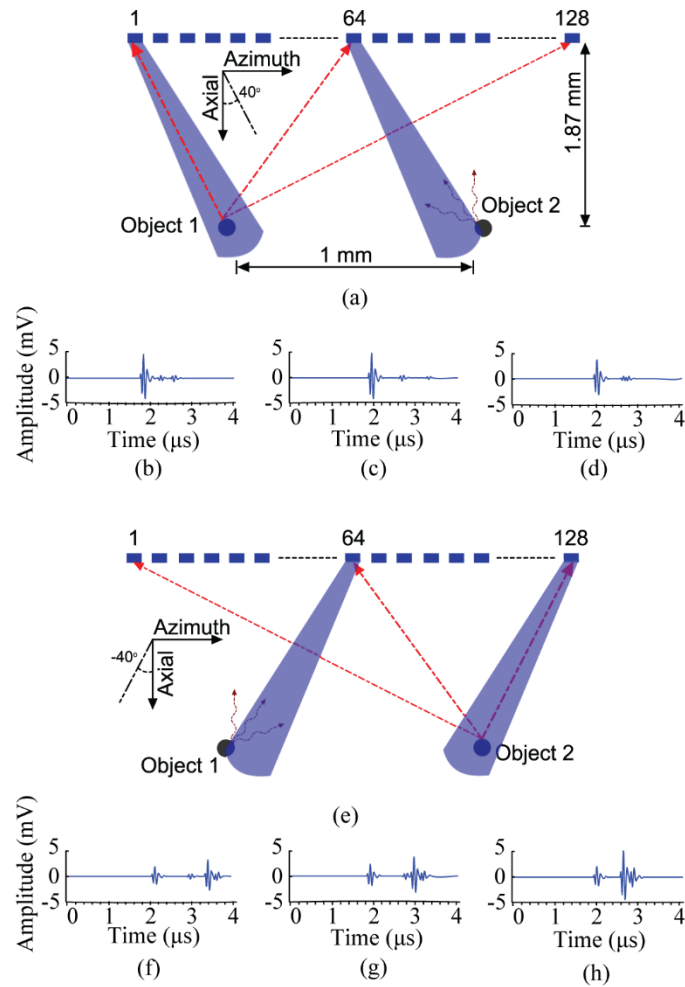


Figure 3.6. (a) Simulated echo signal from object 1 received by (b) element 1, (c) element 64, (d).element 128 at +40° steering angle, (e) echo signal from object 2 received by (f) element 1, (g) element 64 and (h) element 128 at -40° steering angle. The simulation was carried out in Vantage 128 from Verasonics™.

As it is evident from Figure. 3.6(a), when steered to +40°, the strength of the acoustical echo received by the elements 1, 64, and 128 is much higher as compared to the signal received from object 2 by the same elements. Some ringing due to reverberations are also visible. In Figure. 3.6(a), the dotted straight lines represent the reflected signal received by elements 1, 64 and 128. Being the nearest element to object 1, element 1 received the echo signal 0.2 and 0.21 μs earlier as compared to element 64 and element 128 and shows higher amplitude compared to the other two as shown in Figure. 3.6(b, c, d). Similarly, in Figure.

3.6(f, g, h) when the beam was steered -40° as shown in Figure. 3.6(e), echo from object 2 was identified by all the elements. Element 128 received the echo earliest at $2.73 \mu\text{s}$. Element 1 and 64 received the echo with a delay of 0.45 and $0.25 \mu\text{s}$ respectively. An echo with 40% less strength was also noticeable that is due to the unwanted scattered echo from object 1 shown as curved line in Figure. 3.6(e). This analysis verifies that the designed CMUT array is capable of laterally distinguishing two objects apart by 1 mm from each other even at one fifth of the geometric focal length using electronic beamsteering and focusing.

3.5 Discussion

Table 3.2 presents a comparison of the key design specifications of the proposed CMUT array with similar array specifications published elsewhere [72-74]. The comparison establishes that the presented design is capable of providing a wider fractional bandwidth with a lower aperture size for an array with 128 elements to achieve sufficient focal length for ophthalmic diagnostic imaging application.

The B-scan mode imaging performance has been compared with the experimental results presented in [72-74]. A generalized anatomy of the anterior segment of the eye is shown in Figure 3.7. According to [74], the distance from the cornea to iris is typically 2.5 - 3 mm which also includes anterior chamber filled with aqueous humor with an acoustic impedance of 1.72 MRayl . From iris to the back wall of lens is ~ 7 mm that includes posterior chamber, zonules and portion of sclera.

A comparable 4 glass fiber wire phantom has been used in [74] based on the location of the cornea, anterior chamber and the iris of the anterior eye segment.

TABLE 3.2. VALIDATION OF THE DESIGN METHODOLOGY AND ANALYSIS.

Parameter	Presented design	CANNATA <i>et al.</i> [72]	BROWN <i>et al.</i> [73]	YEH <i>et al.</i> [74]
Type	CMUT	Piezoelectric	Piezoelectric	CMUT
Diaphragm material	BCB	2-2 Composite	1-3 Composite	Silicon Nitride
Center frequency (MHz)	40	35	40	41
Number of elements	128	64	256	64
Aperture (mm)	2.41	3.2	10.24	2.3
Pitch (μm)	18.75	50	40	36
Focal depth (mm)	9.3	10	10.24	4.5
-6dB fractional bandwidth	55	52	50	32
Elevation beamwidth (μm)	145		112	
-6dB lateral resolution (μm)	36.4	100		

A 41 MHz silicon nitride based 64 elements CMUT linear array was experimentally operated in B-scan mode at dynamic range of 40 dB. The designed array presented in this paper and similar wire phantom have been simulated in

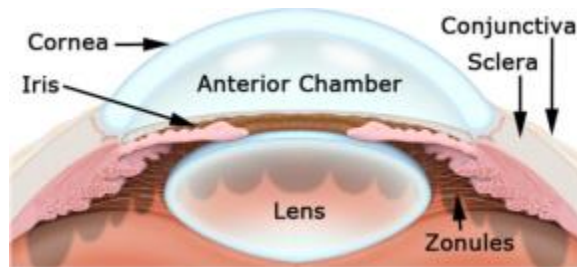


Figure 3.7. A typical anatomy of an anterior eye segment.

Vantage128™ to image in B-scan mode. Comparisons of these two images are shown in Figure 3.8 where it is evident that the presented design is capable of generating high-resolution images as compared to the array presented in [74] even at a depth of >3 mm where the iris is located.

The performance of the BCB based CMUT array was also compared to a 35 MHz piezo-composite ultrasound transducer array in B-scan mode based on the

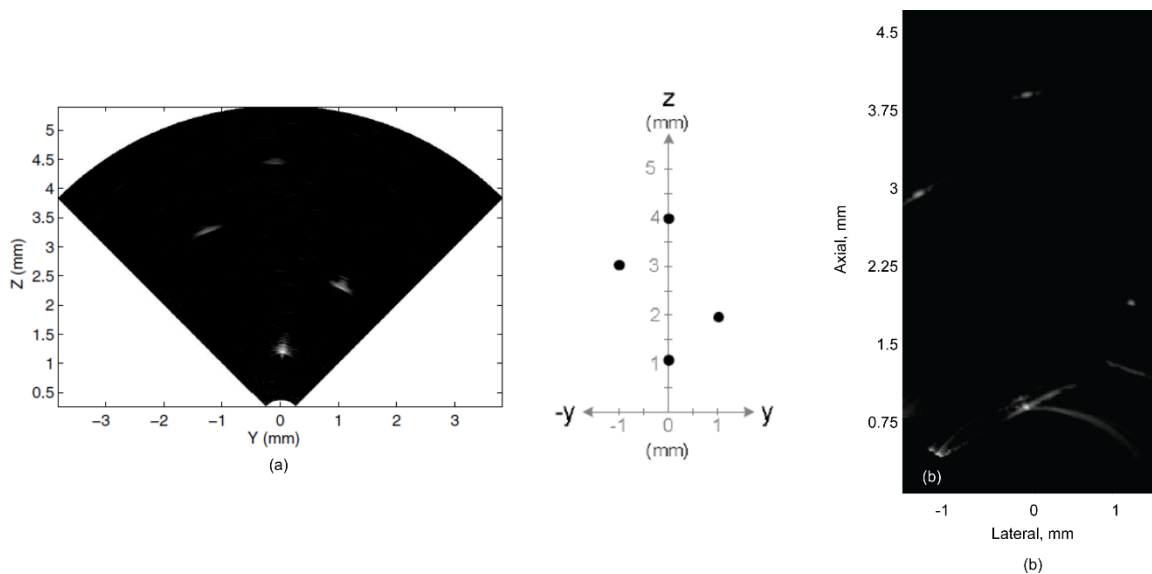


Figure 3.8. B-scan of a four-wire phantom. (a) Experimental result from 41 MHz Si_3N_4 based linear CMUT array [74], (b) Simulated result from 40 MHz BCB based linear phased array CMUT in Vantage128™.

imaging of a five wire phantom as presented in [72]. These wires were located in such way to mimic the position of the rest of the part of the anterior segment. Synthetic aperture images from both the arrays are shown in Figure 3.9. Even though the piezo-composite transducer shows better quality images of the wires placed after 9mm due to higher axial resolution, the design CMUT array is capable of imaging the wires distinctly. Most of the received data from the target wire located at 9.5mm was discarded due to the low signal strength below the threshold

during the signal processing which can be resolved by introducing an apodization scheme to the simulation model.

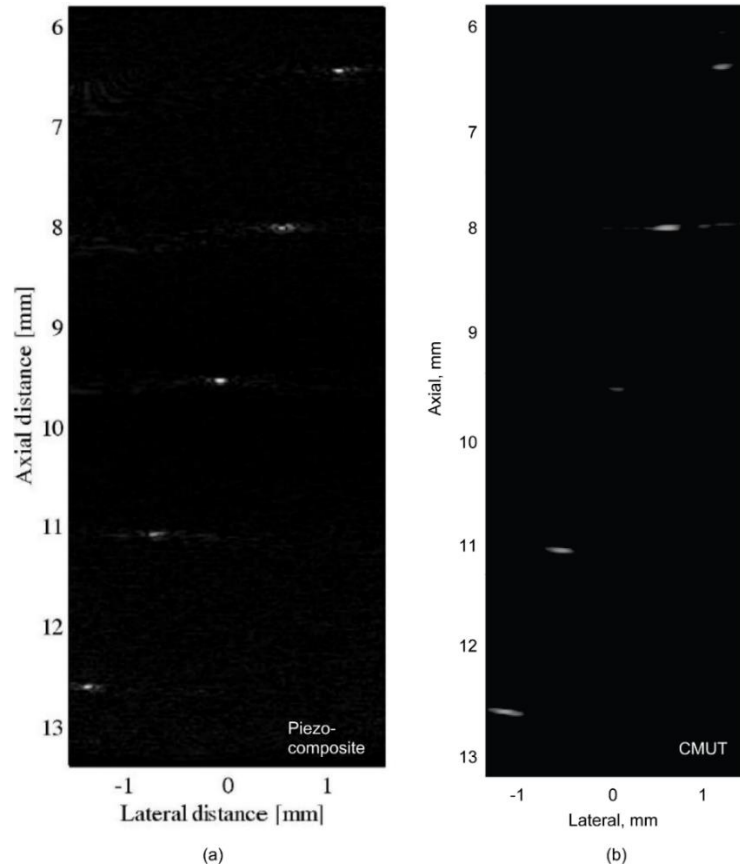
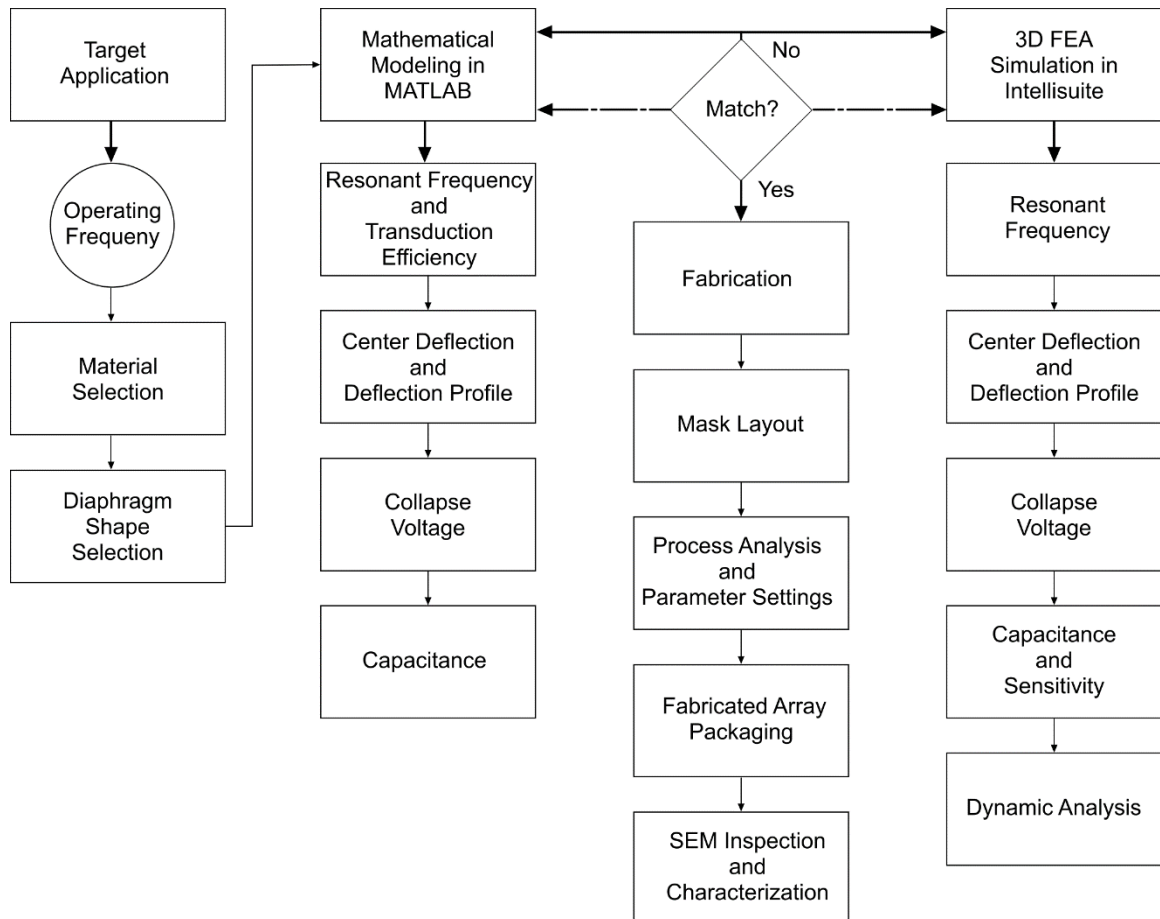


Figure 3.9. Synthetic aperture image of a five-wire phantom in B-scan mode by (a) 35 MHz piezo-composite ultrasound transducer array [72], (b) 40 MHz BCB based CMUT linear phased array in Vanatge128™ imaging platform.

This section presents the design methodology of the CMUT cells that includes the MATLAB based mathematical modeling and 3D FEA simulation results to verify the design. Finite element analysis has been carried out in IntelliSuite™. Results from both mathematical model and FEA simulation are in excellent agreement.

4.1 Design Methodology



Typical CMUT diaphragms are fabricated with a thin aluminum or gold conducting layer on the top of a silicon nitride structural layer [74]. Highly doped polycrystalline silicon or single crystal silicon and other polymers are also used as the diaphragm material [2]. However, as the dielectric property of a semiconductor material such as single crystal silicon or polysilicon is frequency dependent, an analysis presented in [2] shows that at low frequencies such diaphragms behave as conductors and gradually switches to insulators as the frequency increases. Consequently, the associated capacitance change becomes frequency dependent. Investigation by the authors show that these problems can be resolved if it is possible to fabricate the top electrode beneath the diaphragm structural material. This will increase the effective capacitance change to increase the sensitivity while reducing the frequency dependent effects of a semiconductor type diaphragm material or electrical charging effects of a nitride type insulating material. This also will reduce the unwanted charge flow in the dielectric material due to charge tunneling from the biased electrode. Cross-sectional geometry of such CMUT cells are shown in figure 4.1(a) where a low-K insulator BCB has been used as the structural material of the diaphragm. BCB has also been used as the dielectric spacer between the CMUT electrodes. Additionally, a thin BCB layer has been used on the top of the bottom electrode to provide an insulating barrier to prevent any accidental device failure due to pull-in. Low resistivity silicon has been selected to act as the bottom electrode. Relevant physical and electrical properties of all of these materials are provided in Table 4.1. Square shaped CMUT cells having a sidelength of 10 μm have been chosen to optimize the fill factor and

satisfy the array specifications as listed in Table 3.1. A cross-section of the proposed CMUT array with three cells is shown in figure 4.1(a). A single cell is magnified and shown in figure 4.1(b).

TABLE 4.1. MATERIAL PROPERTIES.

Parameters	Unit	Cyclotene-3000™ (BCB)	Gold (Au)	Silicon (Si) <100>
Young's modulus, E	GPa	2.9	70	165.9
Poisson's ratio, ν		0.34	0.44	0.26
Density, ρ	Kg.m ⁻³	1050	19300	2329
Residual stress, σ	MPa	28	106	55
Relative permittivity, ε		2.6	1	11.8
Conductivity, S	S.m ⁻¹		4.1×10^7	1.56×10^{-3}

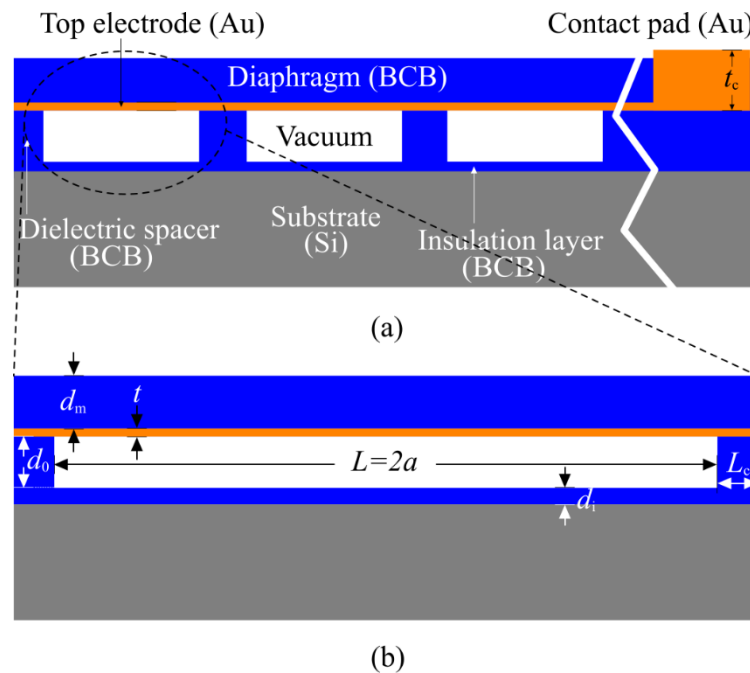


Figure 4.1. (a) A cross-section of the proposed CMUT cells, (b) A single cell structure.

4.2 Center Displacement and Deflection Profile

Maximum displacement of a homogenous and isotropic CMUT membrane with clamped edges takes place at the center of the respective cell under any external load (electrical or ultrasound). A simple cross-section of deformed CMUT cell is shown in figure 4.2. It is assumed that the clamped edges hold the diaphragm rigidly against any out-of-plane rotation or displacement at the edges but allow displacement parallel to the diaphragm plane. At the edges, out-of-plane displacement is zero and the tangent plane to the displacement surface along the edge coincides with the initial position of the middle plane of the diaphragm. The boundary condition can be expressed as follows:

$$\begin{aligned}
 w(x = \pm a, \forall y) &= 0 \\
 w(y = \pm a, \forall x) &= 0 \\
 \frac{dw}{dx}(x = \pm a, \forall y) &= 0 \\
 \frac{dw}{dy}(x = \pm a, \forall x) &= 0
 \end{aligned} \tag{4.1}$$

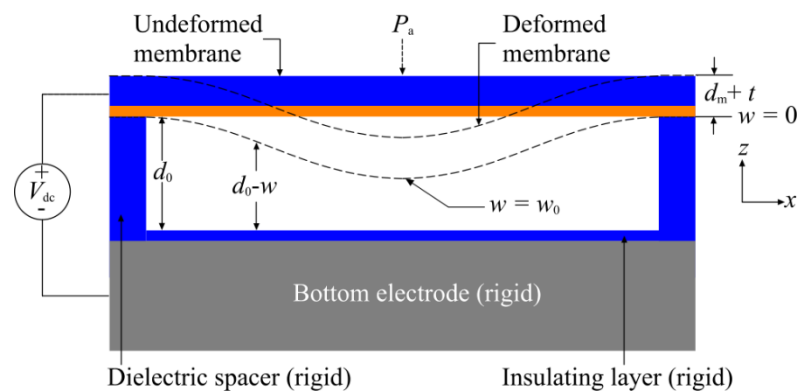


Figure 4.2. Typical boundary conditions and center deflection of a CMUT unit cell.

A center displacement model of a square membrane in [82] that includes both the electrical and ambient air pressure load is expressed as:

$$\begin{aligned} & \left[C_s f_s(\nu) \frac{\tilde{E} t}{a^4} \right] w_0^3 + \left[C_r \frac{\sigma_0 t}{a^2} + C_b \frac{12 D_{eff}}{a^4} - \frac{\epsilon_0 V^2}{2a} \left(\frac{4a}{d_{eff}^3} + 0.394 \frac{a^{0.25}}{d_{eff}^{2.25}} \right) \right] w_0 \\ & - \left[P_a + \frac{\epsilon_0 V^2}{2a} \left(\frac{2a}{d_{eff}^2} + 0.315 \frac{a^{0.25}}{d_{eff}^{1.25}} \right) \right] = 0 \end{aligned} \quad (4.2)$$

Where, w_0 is the membrane center deflection, \tilde{E} is the effective Young's modulus, σ_0 is the residual stress, D_{eff} is the effective flexural rigidity, P_a is the ambient pressure. C_r , C_b and C_s are 3.45, 4.06 and 1.994 respectively. $f_s(\nu)$ and d_{eff} can be calculated from Equation (4.3) and (4.4).

$$f_s(\nu) = \frac{1-0.27\nu}{1-\nu} \quad (4.3)$$

$$d_{eff} = \frac{d_m}{\epsilon_m} + \frac{d_i}{\epsilon_i} + d_0 \quad (4.4)$$

Effective flexural rigidity for a multilayered membrane as shown in Figure 4.1(b) can be expressed as:

$$D_{eff} = \frac{(A \times C) - B^2}{A} \quad (4.5)$$

Where,

$$\begin{aligned}
A &= \sum_k \tilde{E}_k (t_k - t_{k-1}), \\
B &= \sum_k \tilde{E}_k \left(\frac{t_k^2 - t_{k-1}^2}{2} \right), \\
C &= \sum_k \tilde{E}_k \left(\frac{t_k^3 - t_{k-1}^3}{3} \right), \\
\tilde{E}_k &= \frac{E_k}{1 - \nu^2}
\end{aligned} \tag{4.6}$$

In (4.6), k denotes the k^{th} layer of a multilayer lamination of membrane. In this paper, $k = 1$ (BCB) and $k = 2$ (Au).

$$w(x, y) = \left[w_0 + w_1 \left(\frac{x^2 + y^2}{a^2} \right) + w_2 \left(\frac{x^2 y^2}{a^4} \right) + w_3 \left(\frac{x^4 + y^4}{a^4} \right) \right] \cos^2 \left(\frac{\pi x}{2a} \right) \cos^2 \left(\frac{\pi y}{2a} \right) \tag{4.7}$$

Where, the adjustable parameters are multiples of w_0 and can be expressed as following:

$$\begin{aligned}
w_1 &= \frac{0.0013}{\sqrt{t}} w_0, \\
w_2 &= \frac{0.005}{\sqrt{t}} w_0, \\
w_3 &= \frac{0.0021}{\sqrt{t}} w_0
\end{aligned} \tag{4.8}$$

Following (4.2) and (4.7), the deflection profile of the deformed diaphragm due an ambient pressure load of 101.3 kPa has been calculated analytically and shown in figure 4.3. The analytical model result has been compared with the FEA simulation result. The center deflection of 7.6 nm was obtained from the analytical model whereas the 3D FEA result using IntelliSuite™ deviates by 0.36 nm (4.73%). A 3D deflection profile is shown in figure 4.4.

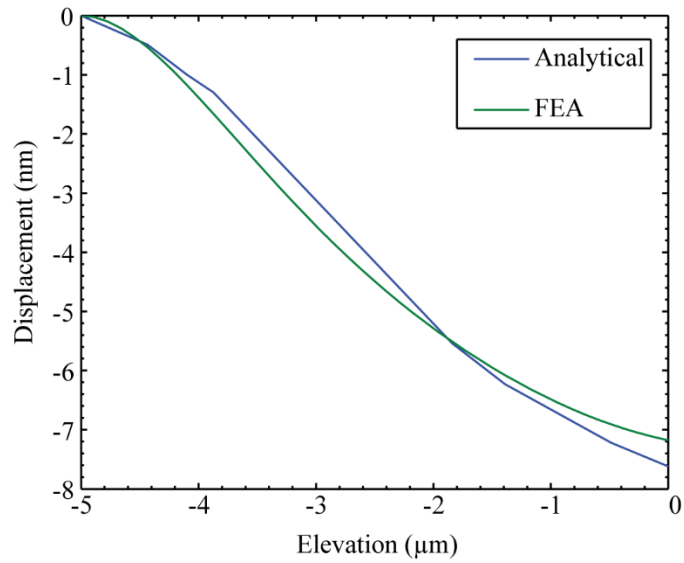


Figure 4.3. Comparison of the diaphragm deflection profile under ambient pressure of 101.3 kPa between analytical and FEA simulation result.

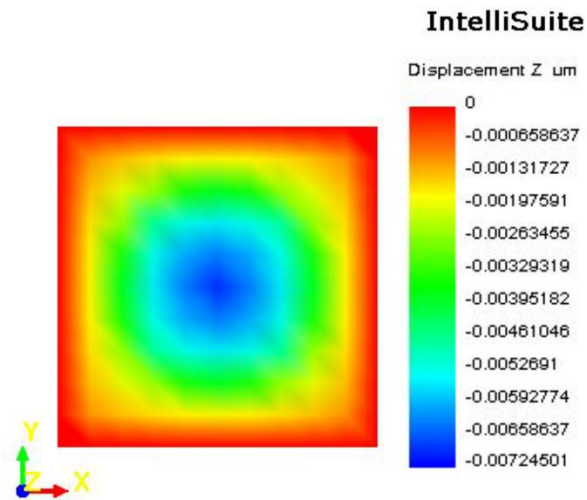


Figure 4.4. 3-D FEA deflection result of a 10x10 μm² diaphragm from IntelliSuite™.

Analytical	FEA	% Deviation
7.6 nm	7.24 nm	4.7

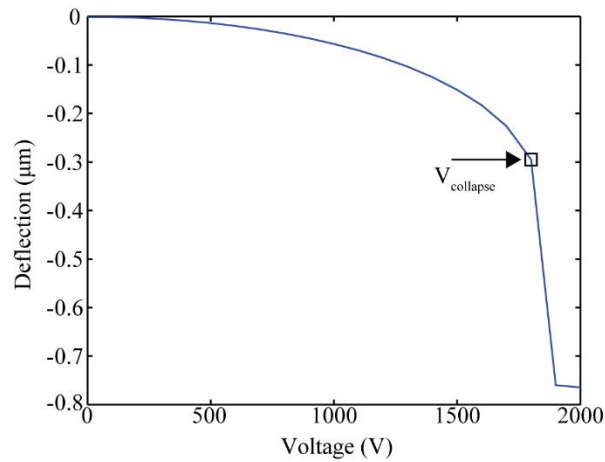
4.3 Collapse Voltage

The collapse voltage is one of the important key factors to design a CMUT array that limits the membrane deflection. When biased with a DC voltage, the membrane deflects towards the bottom electrode due to electrostatic attraction force. The mechanical restoring force of the membrane balances this deflection. However, after increasing the bias voltage after a certain limit, known as collapse or pull-in voltage, the electrostatic force starts dominating over the restoring force and the membrane collapses over the bottom electrode. To avoid short-circuit, typically a dielectric material is used as an insulating layer between the top and bottom electrode as shown in figure 4.1(b). The collapse voltage of the CMUT cell has been calculated as 1680 V following a mathematical model presented in (4.9). The calculated value is in 6.67% agreement with the collapse voltage obtained from IntelliSuite using 3-D electromechanical simulation as shown in figure 4.5 (a, b).

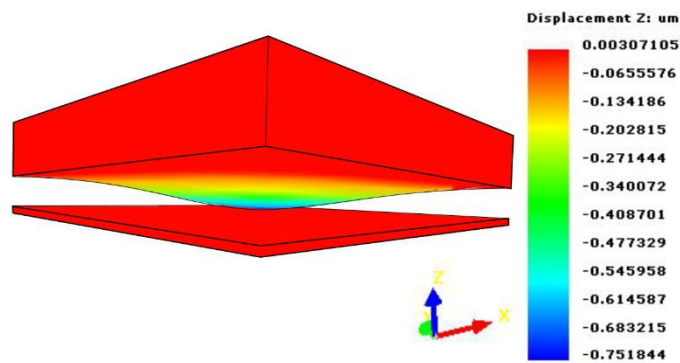
$$V_{collapse} = \sqrt{\frac{\left(\frac{C_r \sigma_0 t}{a^2} + \frac{12C_b D_{eff}}{a^4}\right) + \left(\frac{C_s f_s(v) \tilde{E} t}{a^4}\right) \frac{d_{eff}^3}{9}}{3\epsilon_0 \left(\frac{0.665}{d_{eff}^2} + \frac{0.2231a^{-0.75}}{d_{eff}^{1.25}}\right)}} \quad (4.9)$$

Following [83], CMUTs with smaller size diaphragm with large gap height between two electrodes has high collapse voltage. For example, a 20 μm radius circular diaphragm with 1.5 μm diaphragm and 0.2 μm electrode thickness has been reported to have a collapse voltage of 1300 V [84]. The collapse voltage can be

reduced by reducing the gap height if other variables remain unchanged. However, a lower gap height would result in a lower dynamic range.



(a)



(b)

Figure 4.5. (a) Collapse voltage of a $10 \times 10 \mu\text{m}^2$ square diaphragm CMUT cell at 1752 V, (b) 3D FEA diaphragm collapses at pull-in voltage in IntelliSuite™.

Analytical	FEA	% Deviation
1680 V	1752 V	0.04

4.4 Resonant Frequency, Drift Analysis and Coupling Efficiency

Natural frequency was calculated 40 MHz in air using (4.10) that is presented in [85]. 3D FEA model with fixed boundary condition on all sides of the membrane except the top and bottom surface that has been used for collapse voltage calculation in Intellisuite was also utilized to calculate the natural frequency under no external loading.

$$f = \sqrt{\frac{1}{\rho} \left(\frac{D_{eff} \pi^2}{a^4} + \frac{T}{2a^2} \right)} \quad (4.10)$$

where, tensile force, $T = \sigma \times t$. 3-D FEA simulated resonance frequency has been obtained as 39.2 MHz from IntelliSuite. A 0-300 V DC bias sweep with an increment of 10 V was used to determine the natural frequency shift due to the spring softening effect as shown in figure 4.6.

The diaphragm mechanical impedance was calculated by solving fourth order differential equation of motion presented in [86] and electrical impedance in air was calculated by simplifying the first order equivalent circuit model presented in [86]. The diaphragm mechanical impedance and electrical imaginary impedance are plotted in figure 4.7 and 4.8, respectively as a function of frequency. According to figure 4.7, diaphragm impedance shows a -3dB bandwidth of 142.01%.

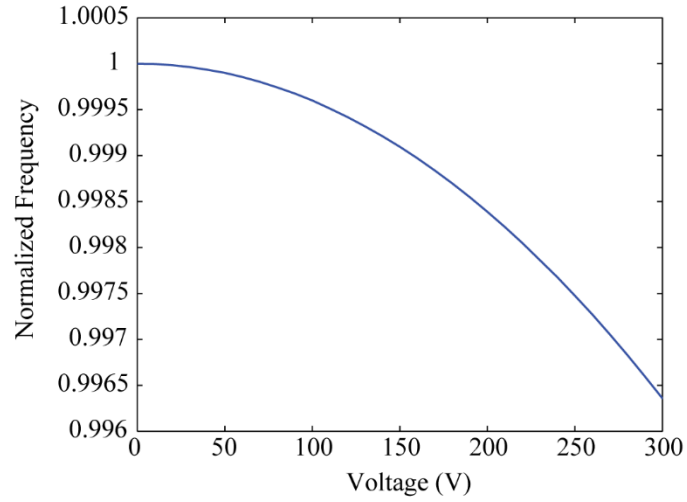


Figure 4.6. Spring softening phenomenon in terms of natural frequency drift as a function of bias voltage.

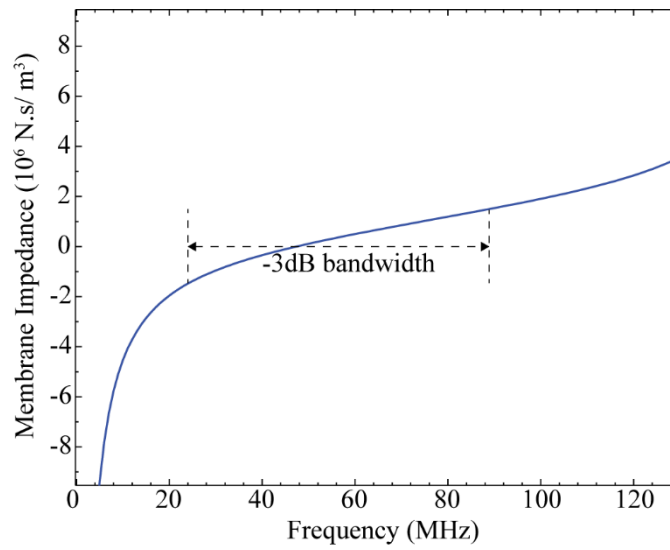


Figure 4.7. Mechanical impedance of a CMUT cell diaphragm as a function of frequency.

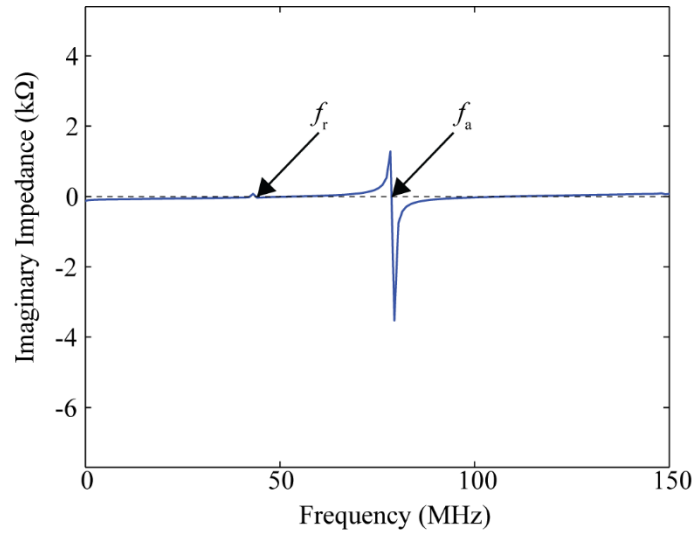


Figure 4.8. Matlab based resonance and anti-resonance frequencies extracted from imaginary electrical impedance curve as a function of frequency.

Analytical	FEA	First order circuit model
40 MHz	39.2 MHz	48.25 MHz

In figure 4.8, the series resonance frequency f_r was 48.25 MHz where the impedance curve intersects the dotted line. The maximum impedance is at 78.5 MHz that corresponds to the parallel resonance frequency, f_a . The difference between the results from the equivalent circuit model and the FEA simulation is due to the simplification of the first order model.

Electromechanical coupling coefficient k_T^2 can be extracted following (4.11) based on resonant and anti-resonant frequency [87]. The extracted coupling coefficient was 0.63 that is 53.3% higher than the coupling coefficient presented in [26]. High coupling coefficient due to the use of BCB diaphragm at a very low bias voltage

compared to other dielectric material increases the dynamic range of the CMUT and at the same time avoids operation near the non-linear regime close to pull-in.

$$k_T^2 = 1 - \left(\frac{f_r}{f_a} \right)^2 \quad (4.11)$$

4.5 Capacitance Analysis and Sensitivity

The two parallel electrodes (top and bottom) with a dielectric medium in between act as two parallel plates of a capacitor. The static capacitance of a single CMUT cell was approximated 0.997 fF from the following (4.12).

$$C = C_0 (1 + C_{ff}) \quad (4.12)$$

Where, C_0 is the parallel plate capacitance associated with CMUT and C_{ff} is the capacitance due to fringing field effect. Both the capacitance value can be expressed as follows:

$$C_0 = \frac{4\epsilon_0 a^2}{d_{eff}} \quad (4.13)$$

$$C_{ff} = \frac{0.385 d_{eff}}{a} + 1.06 \left(\frac{d_{eff}}{2a} \right)^{0.75} + \frac{0.53}{a} (t \times d_{eff})^{0.5} \quad (4.14)$$

This capacitance changes as the membrane deflects towards the bottom electrode when electrostatic force is generated due to the applied dc bias and overcome the mechanical restoring force. The capacitance between the membrane and bottom electrode after the deformation can be approximated from the following:

$$C = C_d (1 + C_{ff}) \quad (4.15)$$

$$C_d = \epsilon_0 \iint_A \left(\frac{dxdy}{d_{eff} - w(x,y)} \right) \quad (4.16)$$

Where, C_d was calculated based on the deflection profile of the membrane w on the (x, y) plane. The static capacitance of a single CMUT cell has been calculated following (4.12) as 1.3 fF. A comparison of analytical model (4.15) and 3-D FEA evaluated capacitance change as a function of DC bias is shown in figure 4.9.

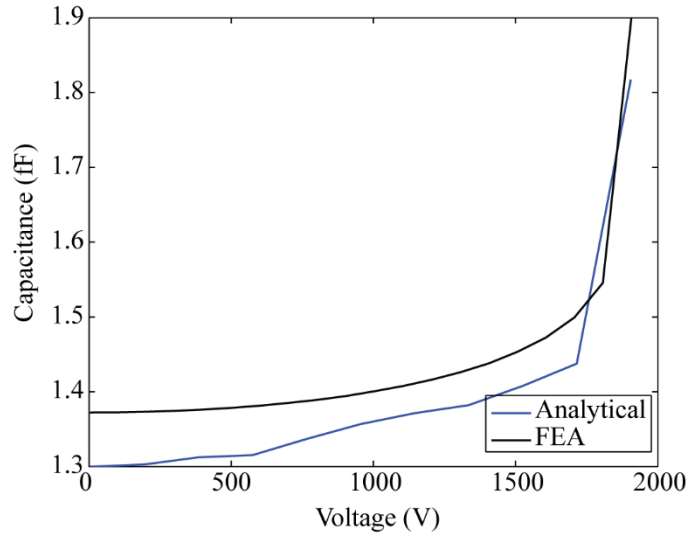


Figure 4.9. Comparison of a single cell capacitance changes as a function of applied DC bias voltage based on analytical and 3-D FEA model.

Analytical	FEA	% Deviation
1.3 fF	1.37 fF	5.1

Figure 4.9 shows that the FEA simulation and analytical results are in good agreement with a maximum deviation of 6.2%. Capacitance changes abruptly after

1800 V in FEA model which also represents the occurrence of the pull-in whereas analytical model exhibits the collapse phenomenon at 1694 V.

The sensitivity of the CMUT cell has been calculated to be $1.89 \mu\text{V}.\text{Pa}^{-1}$ following (4.17) as presented in [88]:

$$\text{Sensitivity} = \left(\frac{C_{adc} - C_{dc}}{C_{dc} \Delta P} \right) V_0 \quad (4.17)$$

Where, C_{dc} is the capacitance value after applying a DC bias and C_{adc} is the capacitance after applying a combination of DC bias and acoustic pressure. The receive sensitivity was calculated based on the operating voltage, V_0 and the acoustic pressure, ΔP of the ultrasonic wave at the CMUT cell surface reflected from the cornea. The parameter values were deduced from the 3-D FEA model in IntelliSuite™ and shown in Table 4.2.

TABLE 4.2. SENSITIVITY PARAMETERS EXTRACTED FROM INTELLISUITE™.

Parameter	C_{dc} (fF)	C_{adc} (fF)	ΔP (MPa)	V_0 (V)
Value	1.330	1.348	1.16	100

4.6 Dynamic Analysis

Dynamic displacement as a function of frequency under the ambient pressure was analyzed in IntelliSuite™ and shown in figure 4.10. The maximum displacement of $0.04 \mu\text{m}$ at 39.2 MHz also verifies the resonance of the diaphragm.

The dynamic settling time of the diaphragm has been simulated in IntelliSuite™ where the input mechanical parameter of the simulation was set to an ambient pressure of 101.3 kPa. A 3 μs short 1 V pulse of electrical load was superimposed

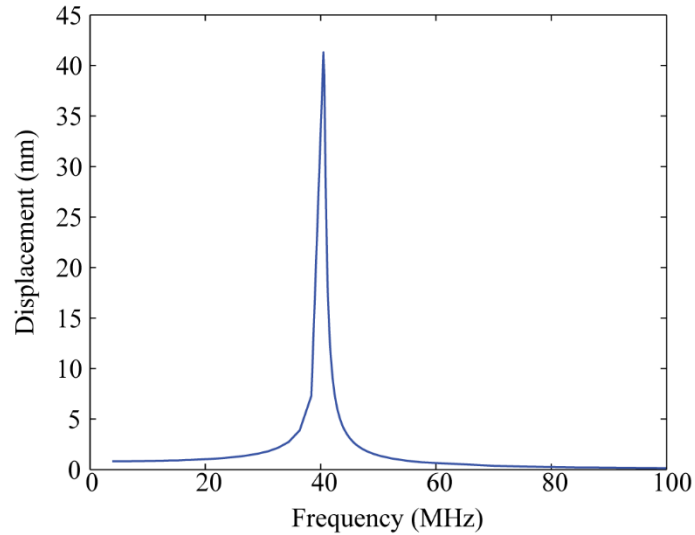
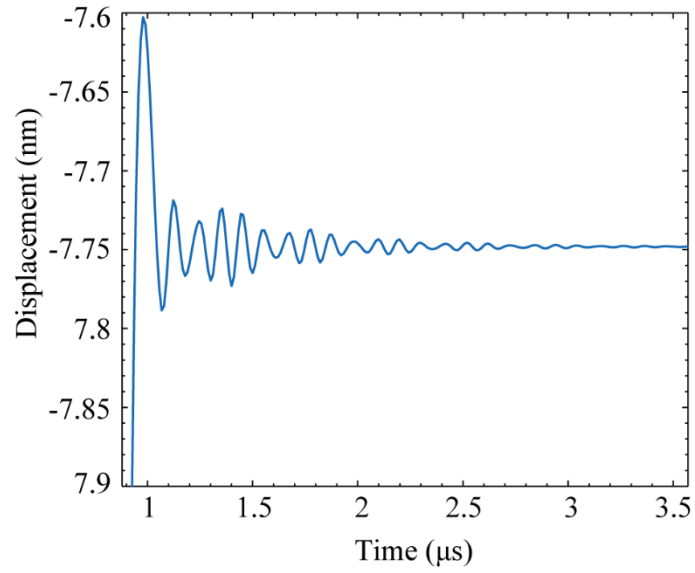


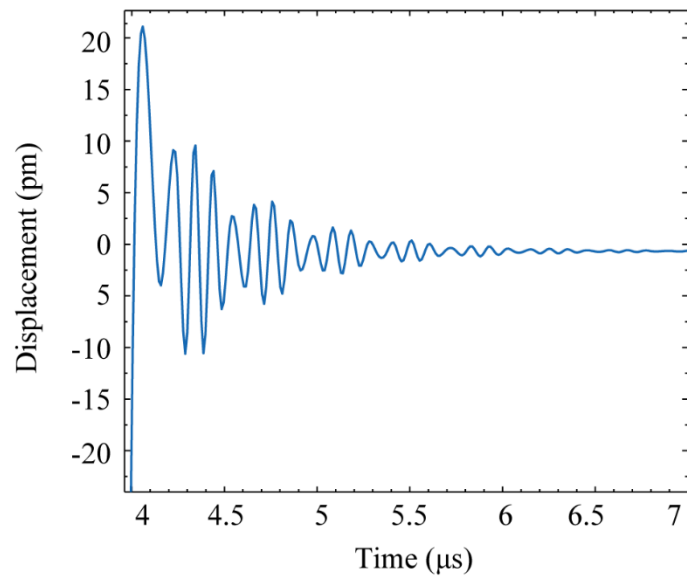
Figure 4.10. Dynamic displacement of a $10 \times 10 \mu\text{m}^2$ square diaphragm as a function of frequency in IntelliSuite™.

at simulation time, $t=1 \mu\text{s}$. The simulated mechanical load (pressure) and the electrical load was applied to the top surface of the BCB layer and the top electrode gold layer of the FEA model respectively to evaluate the impulse response of the diaphragm.

The deflection due to the electrical and pressure load was settled at 7.756 nm in 2.5 μs with an initial overshoot of 1.88%. At $t=4 \mu\text{s}$, the diaphragm restored to the initial position of unbiased condition with a settling time of 2.9 μs and an overshoot up to 21 pm as shown in figure 4.11



(a)



(b)

Figure 4.11. Dynamic settling time of a unit cell (a) applying 1 V DC bias and (b) reducing to 0 V DC bias in IntelliSuite™.

4.7 Discussion

Following (4.18) as presented in [82] the spring softening, k_s of an electrostatically actuated diaphragm with square geometry as shown in figure 4.1(b) can be expressed as:

$$k_s = \frac{\epsilon_0 V_0^2}{2a} \left(\frac{4a}{d_{eff}^3} + 0.394 \frac{a^{0.25}}{d_{eff}^{2.25}} \right) \quad (4.18)$$

where V is the bias voltage. BCB and Silicon nitride diaphragm based CMUT cells having the same structural specifications as listed in Table 4.3 have been compared to predict the effect of spring softening on both the cells following (4.18).

TABLE 4.3. DESIGN SPECIFICATIONS OF A CMUT CELL.

Parameter	Unit	Value
Cell sidelength, $L = 2a$	μm	10
BCB diaphragm layer thickness, d_m	μm	1.5
Cavity height, d_0	nm	750
Insulating layer thickness, d_i	nm	200
Top electrode thickness, t	nm	100
Contact pad area, A_c	μm^2	150 x 150
Contact pad thickness, t_c	μm	0.5
Dielectric spacer width, L_c	μm	8.75

The effect of spring softening on the stiffness of the BCB diaphragm was 51.69% less as compared to the effect on that of the Silicon nitride diaphragm. The coupling

coefficient can be evaluated following (4.19) where the initial stiffness, k_u is due to accumulated effect of residual stress, bending [82] and the stiffness after biasing is $k_b = k_u - k_s$ which are provided in Table 4.4.

TABLE 4.4. ANALYSIS OF THE SPRING SOFTENING EFFECT ON STIFFNESS AND COUPLING COEFFICIENT.

Stiffness parameter	Silicon nitride (N/m)	BCB (N/m)
Spring softening, k_s	1.74	0.7
Residual stress, k_r	2.93×10^3	620.17
Bending, k_{be}	7.84×10^4	1.02×10^3
Initial stiffness, k_u	8.13×10^4	1.63×10^3
Biased stiffness, k_b	8.12×10^4	1.62×10^3
Ratio, k_s/k_u	0.21×10^{-4}	4.27×10^{-4}

Following (4.19), the coupling coefficient was calculated to be 94.9% higher for BCB diaphragm as compared to Silicon nitride at 30 V DC biasing.

$$k_T^2 = 1 - \frac{k_b}{k_u} = 1 - \frac{k_u - k_s}{k_u} \quad (4.19)$$

Based on this rationale, at 30 V DC bias (1.76 % of the collapse voltage), the proposed CMUT design is able to achieve coupling coefficient up to 0.63 that is 93.65% higher than nitride based diaphragm presented in [84]. The electromechanical coupling coefficient is also 2.1 times higher than the CMUT with 0.294 coupling efficiency where BCB is used only as an insulating layer and silicon as the diaphragm material in [26]. The model presented in [84] requires 193 V

(96.5% of the collapse voltage) to achieve similar coupling coefficient based on the extrapolation of the coupling coefficient curve as a function of bias voltage. This clearly establishes that a BCB diaphragm based CMUT exhibits superior coupling coefficient and lower frequency drift due to lower spring softening. Furthermore, as a high coupling coefficient can be achieved at a much lower voltage, the technique will be helpful to avoid nonlinear operation near collapse while achieving high transduction efficiency.

The DC bias can still be increased to a higher level that is generally used for CMUT biasing (100 V-200 V) to achieve larger displacement of the diaphragm as per the requirement of the application. The typical output voltage of a CMUT when biased with 100-160 V is in the range of 1-5 mV depending on the number of cells and their geometry. The CMUT cell model in IntelliSuite is simulated with a bias voltage of 100 V DC along with a 50 V_{p-p} square pulse AC signal at 40 MHz. The simulation result shows a maximum deflection of individual cell diaphragm is 15.3 nm that corresponds to an output acoustic pressure of 4.17 MPa from the array following

$$P_{out} = \text{Re}(Z_m) \omega w_0 \quad (4.20)$$

where, $\text{Re}(Z_m)$ is the real value of the medium impedance in Rayl and ω is the operating frequency in radians. Typically, for ophthalmic imaging the ultrasound travel distance is 2~4 mm. Following [89], a two-way attenuation at 40 MHz in oil medium has been calculated to be 11.7 dB. Considering this attenuation, the magnitude of the maximum rarefaction pressure of the returning acoustic wave

$$Attenuation(\text{dB}/\text{mm}) = 4.7 \times 10^{-2} f_r^{1.12} \quad (4.21)$$

can be calculated as 1.16 MPa. Following [82], this pressure can effect 0.35 pF capacitance change in an element that in turn result in an output current of 0.8 mA as per (4.22) where n is the number of cells in each element.

$$I = \omega n w_0 V \cdot C_d \Big|_{w=w_0} \quad (4.22)$$

A commercially available low noise transimpedance amplifier MAX4805A from MAXIM Integrated™, with a voltage gain of 8.7 dB can be used to obtain a voltage output of 2.1 mV from this amount of current. This output magnitude can easily be processed further using existing signal processing circuits. The sensitivity of a single CMUT cell has been calculated from the extracted values of capacitance change using the 3D FEA model. For a single element with 264 cells biased at 100 V, the individual element sensitivity has been calculated to be 628.32mV.kPa⁻¹ that is 1.57 times higher than the sensitivity measured for individual elements in [90]. Therefore, the proposed design of the CMUT is capable of generating output signals that can be detected and processed by existing imaging system within the practical range of DC biasing that is much lower than the collapse voltage with a superior sensitivity and higher transduction efficiency. This proposed design to achieve high coupling coefficient at low bias voltage will open up the possibility to increase the sensitivity and the dynamic range of the CMUT further to emit and receive high acoustic pressure at a low operating voltage.

Fabrication of Linear Phased CMUT Array

The fabrication process flow of the designed CMUT array is shown conceptually in Fig. 5.1-5.3 where Fig. 5.1 shows the realization of the CMUT diaphragm including the metallization and the cavity on wafer 1, Fig. 5.2 shows the processing of wafer 2 (backplate) and adhesive bonding of wafer 1 and wafer 2, and finally Fig. 5.3 shows the removal of wafer 1 and contact pad realization.

Following Fig. 5.1, the fabrication started with thermal oxidation of a 500 μm thick silicon wafer (wafer 1) to grow 1 μm thick oxide layer as shown in Fig. 5.1(a). 1500 nm thick BCB layer (Cyclotene™ 3022-35) was then spin deposited on the topside oxide layer as shown in Fig. 5.1(b). This process step was followed by deposition and patterning of a 100 nm thick gold layer on top of the BCB layer to form the top electrode and the routing traces as shown in Fig. 5.1(c). In the next step a 750 nm thick BCB layer was spin deposited and patterned on top of the gold layer to realize the CMUT cavities and the dielectric spacers as shown in Fig. 5.1(d, e).

In the next step, a 200 nm thin layer of BCB was spin deposited on the top side of wafer 2 (bottom electrode) as shown in Fig. 5.2(a, b) to prevent accidental short circuit. Wafer 1 was then flipped and adhesively bonded in a vacuum with wafer 2 using a low temperature process. Next, the top silicon and oxide layers at the top of the bonded structure were removed as shown in Fig. 5.3(a). Finally,

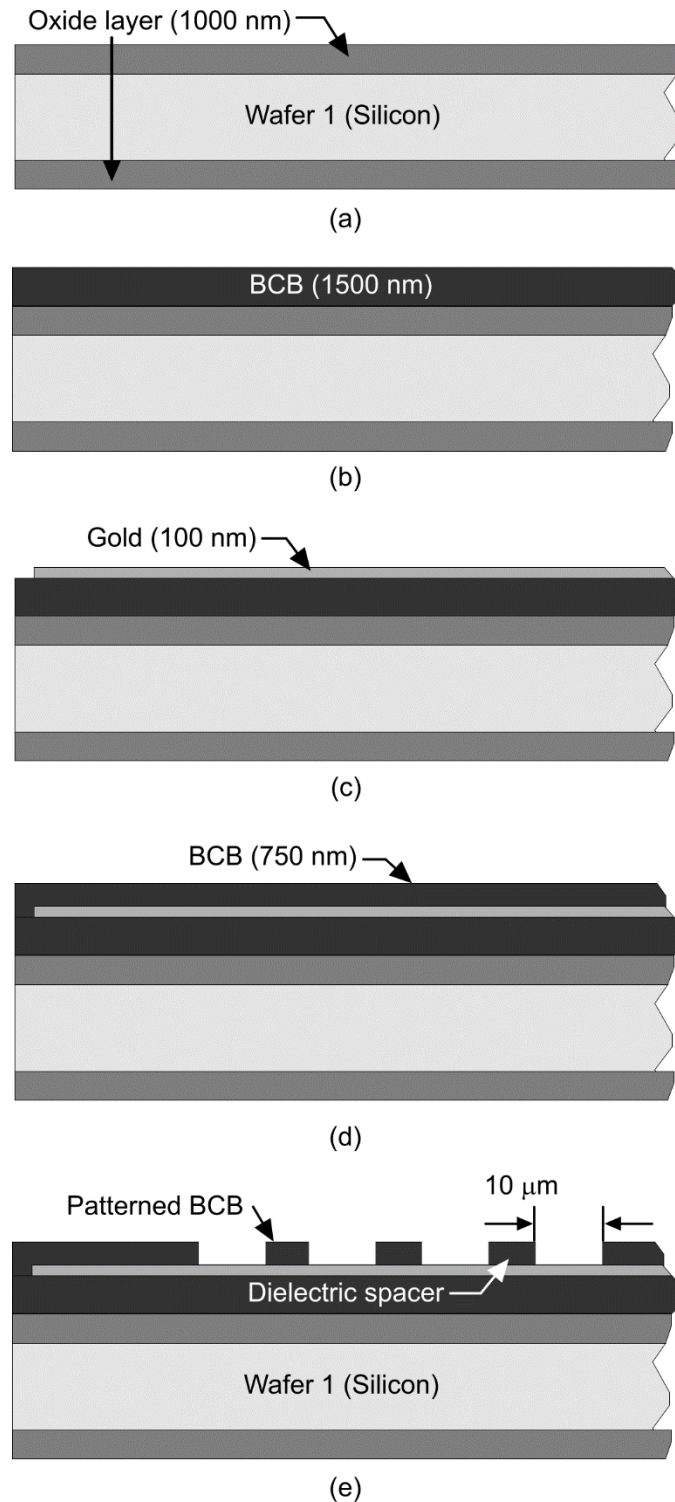


Figure 5.1. (a) Thermally grown 1000 nm oxide layer on both sides of the silicon wafer (wafer 1), (b) structural BCB layer deposition for CMUT diaphragm (1500 nm), (c) gold metallization to realize the top electrode and routing traces, (d) BCB layer deposition for interelectrode dielectric spacer (750 nm), and (e) Patterning of BCB layer to create the CMUT cavities.

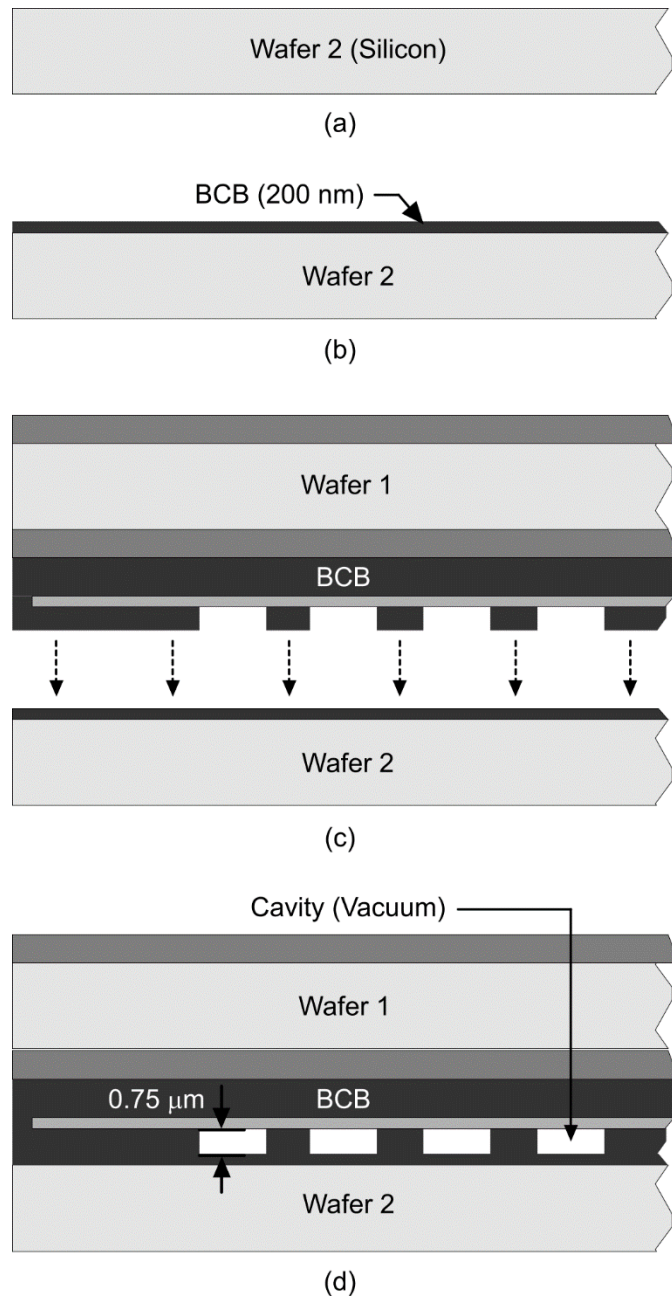


Figure 5.2. (a) Wafer 2 (bottom electrode) cleaning, (b), 200 nm BCB insulating layer realization, and (c), (d) Adhesive wafer bonding of wafer 1 and wafer 2. nm thick gold contact pads.

the top BCB layer was patterned to create the contact pad positions that were filled with 400 nm thick gold contact pads. This step is shown in Fig. 5.3 (b) and (c). An elevation plane cross-section of an element is shown in Fig. 5.3 (c). In Fig. 5.4, a conceptual top view of the fabricated CMUT array is provided and a section of it is magnified to show the cross-section drawn across the azimuthal plane for better visualization of the array geometry. This step is shown in Fig. 5.3 (b) and (c). An elevation plane cross-section of an element is shown in Fig. 5.3 (c). In Fig. 5.4, a conceptual top view of the fabricated CMUT array is provided and a section of it is magnified to show the cross-section drawn across the azimuthal plane for better visualization of the array geometry. The following section describes the detailed fabrication process.

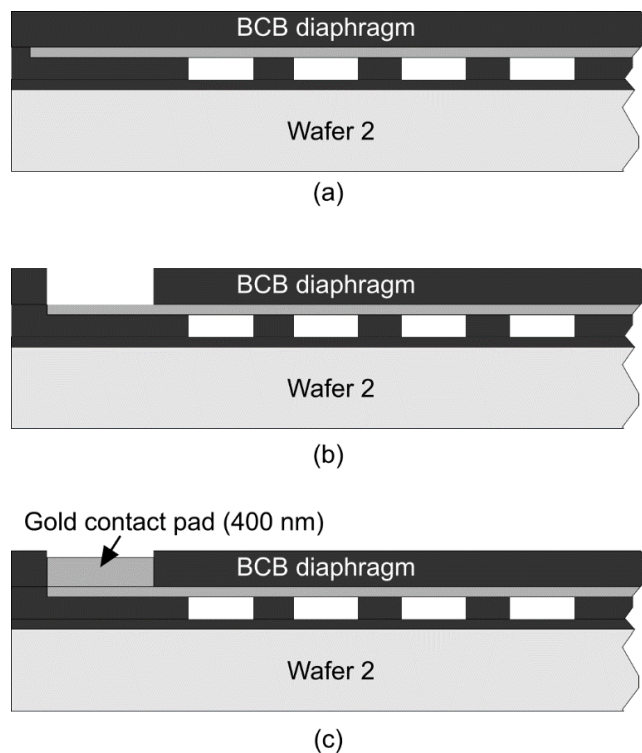


Figure 5.3. (a) BCB diaphragm realization by etching the top silicon and oxide layers, (b) realization of contact pad regions by selectively etching the top BCB diaphragm, and (c) realization of contact pads by depositing gold layer (400 nm).

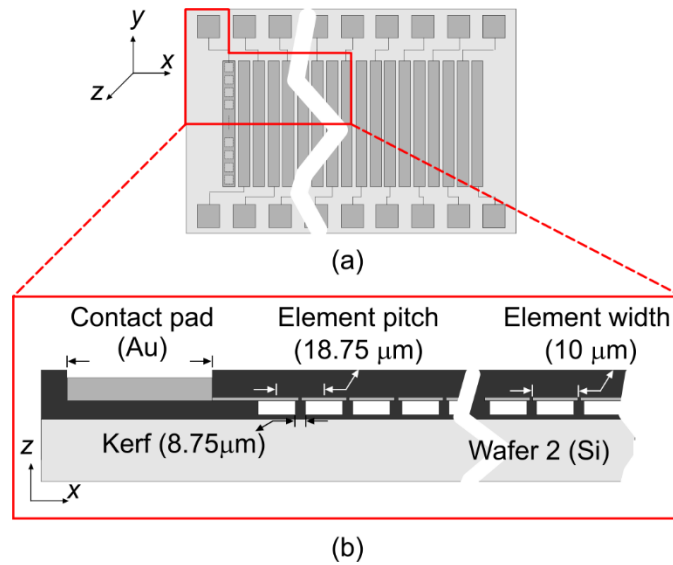


Figure 5.4. (a) Conceptual top view of the fabricated CMUT array, and (b) magnified cross-section across the azimuthal plane.

5.1 Oxide Layer Deposition

The process started with a 100 mm diameter single sided polished <100> oriented silicon wafer (wafer 1). The wafer thickness is 500 μm with a maximum thickness variation of ± 4 μm measured at five different points excluding the edges. The wafer was cleaned in a standard RCA process and 1 μm thick oxide layer was grown on both sides of the wafer using a thermal oxidation process as shown in Fig. 5.1(a).

5.2 Realization of BCB Diaphragm

The wafer was cleaned with O₂ plasma for 20 minutes at 10 sccm flow rate, 100 mTorr chamber pressure, and 90 W RF power. After cleaning, the wafer was rinsed with DI water, dried, and vacuum baked at 150°C. A BCB adhesion promoter AP3000 [34] was spin coated (~ 10 Å) on the wafer topside with a spread speed at 500 rpm for 5 seconds and spin speed of 3000 rpm for 45 seconds. Later the wafer was baked on a hotplate for 2 minutes at 150°C to cure the adhesion promoter. It

was followed by spin coating of BCB without any Mesitylene dilution at a spread speed of 500 rpm for 5 seconds, spin speed of 2300 rpm for 45 seconds and then baked on a hotplate at 100°C for 2 minutes. BCB spin curves for different dilutions (n:m) are shown in Fig. 5.5 where n and m represent BCB and Mesitylene by weight.

However, the aim of the BCB baking at this stage was to achieve about 80% of curing that provides enough stability and acceptable adhesion to the subsequent BCB layer [19]. The baking oven was under nitrogen flow with the thermal profile

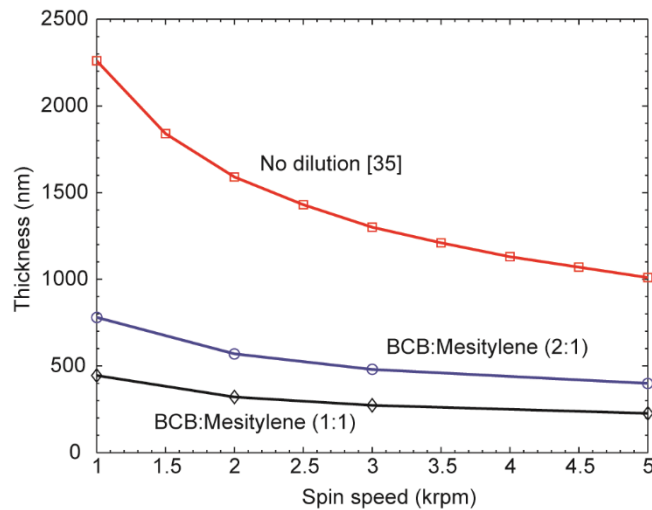
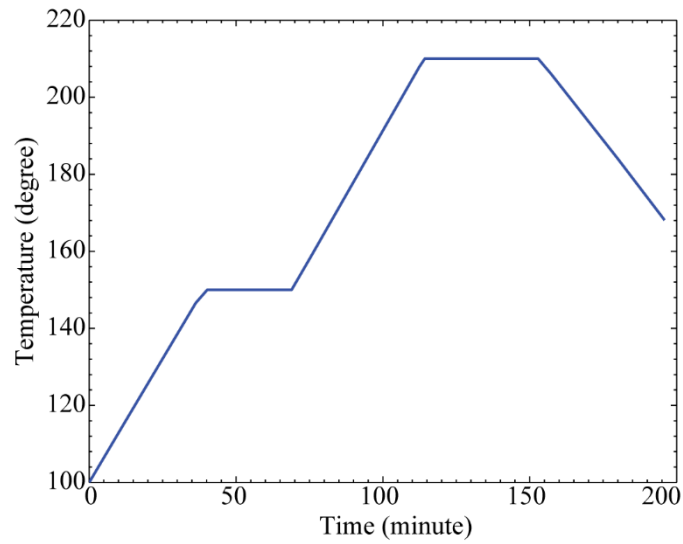


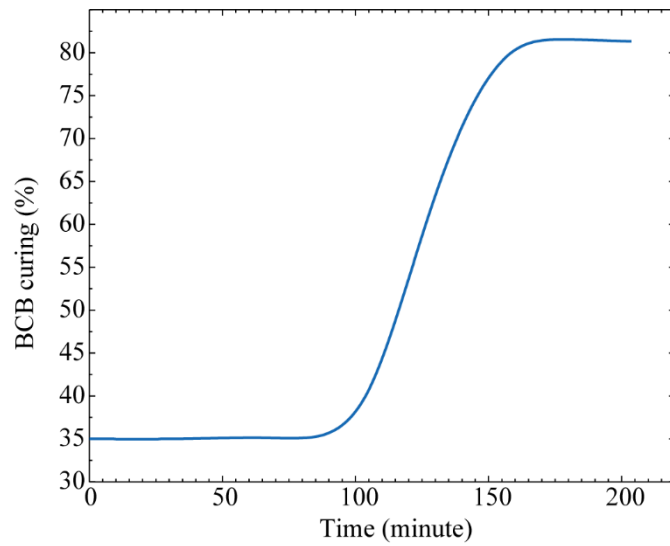
Figure 5.5. Cyclotene™ 3022-35 spin curve for different BCB and Mesitylene ratio.

mentioned in Table 5.1. The curing profile and the corresponding curing level for this step are shown in Fig. 5.6 based on Appendix A. The desired wafer temperature was achieved by adjusting the oven set point. The set point was determined and adjusted to 25°C higher for wafer temperature between 120°C to

170°C and to 20°C higher for wafer temperature above 170°C up to 220°C. About 5% layer shrinkage was expected during the curing process [15].



(a)



(b)

Figure 5.6. (a) Temperature profile, and (b) the corresponding curing level for BCB diaphragm layer.

TABLE 5.1. 80% CURING PROFILE FOR BCB

Duration (minute)	Temperature (°C)
1 (multiple purging)	100
39 (Ramp)	150
30 (Soak)	150
45 (Ramp)	210
40 (Soak)	210
Cool down to below 150 °C	

5.3 Top Metallization and Routing

The aim of this step was to form the CMUT top electrode and the routing traces to the contact pads as shown in Fig. 5.1(c). The process step was started with spin coating of 320 nm LOR 3A (lift-off resist) at spread speed of 300 rpm for 5 seconds, followed by spin speed of 3000 rpm for 45 seconds and soft baking on a hot plate at 170°C for 5 minutes. This step was followed by spin coating of 500 nm Shipley 1805 photoresist at spread speed and spin speed of 500 rpm and 3000 rpm, respectively, for 5 and 45 seconds. A hot plate baking was performed next at 115°C for 3 minutes. The layers were exposed to 405 nm wavelength UV light at a dose of 55 mJ.cm⁻² and developed for 130 seconds in MF319 developer. The wafer was spin rinsed in DI water and dried. A 30 seconds duration short BCB descum etching was carried out to clean any residuals that might roughen the BCB surface in a microscopic level. This step also increases the BCB adhesion to metals. This BCB descum etch-clean recipe was carried out using 10 sccm of CF₄, 40 sccm of O₂ at a chamber pressure of 100 mTorr and RF power of 90 W.

Afterward, a 5 nm thick titanium layer was deposited as a promoter for BCB-gold adhesion. It was followed by deposition of 100 nm of gold using an e-beam evaporation process. The sample was kept in PG remover solution for 2 hours and the beaker was shaken every 0.5 hours. Layer swelling was observed as PG remover has a tendency to diffuse into BCB layer, especially at the edge of the patterns where it was exposed more to the solvent. 1 hour of vacuum baking at 100°C was done to evaporate the diffused PG remover. At last, the wafer was spin washed with DI water and dried.

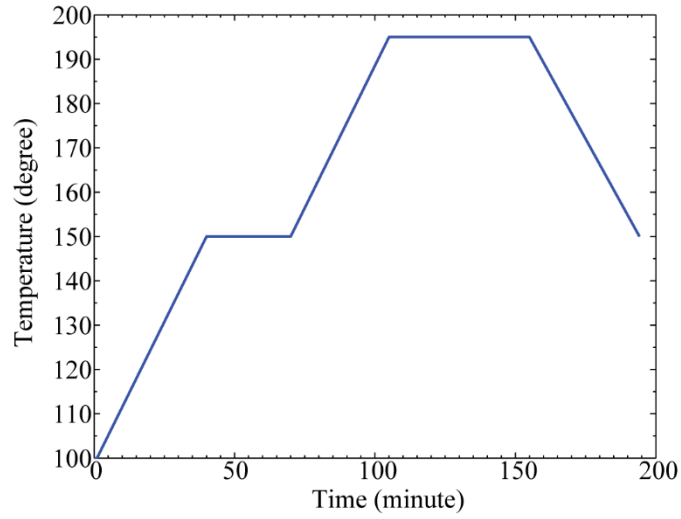
5.4 BCB Cavity Formation

Following Fig. 5.1(d) and 5.1(e), a 750 nm thick BCB layer was deposited on the top of the gold layer followed by carefully patterned etching of the deposited layer to realize the desired cavity height. This process step was started with the spin coating of AP3000 adhesion promotion ($\sim 10 \text{ \AA}$) to increase BCB-gold adhesion at a spread speed of 500 rpm for 5 seconds followed by a spin speed of 3000 rpm for 45 seconds and finally soft baking on a hotplate at 170°C. This step was followed by spin deposition of another layer of BCB of 2:1 dilution with Mesitylene by weight with a spread speed of 500 rpm for 5 seconds, followed by spin speed of 1000 rpm for 45 seconds, and finally baked on a hotplate at 100°C for 2 minutes. This step was followed by a curing procedure suitable for the bonding. The curing level must be balanced between allowing reactivity of the BCB for bonding while minimizing the amount of flow during bonding process under vacuum and therefore pattern fidelity. The curing aim at this stage was to achieve 50-60% curing level [19]. Various temperature profiles and curing levels calculated from Appendix A for

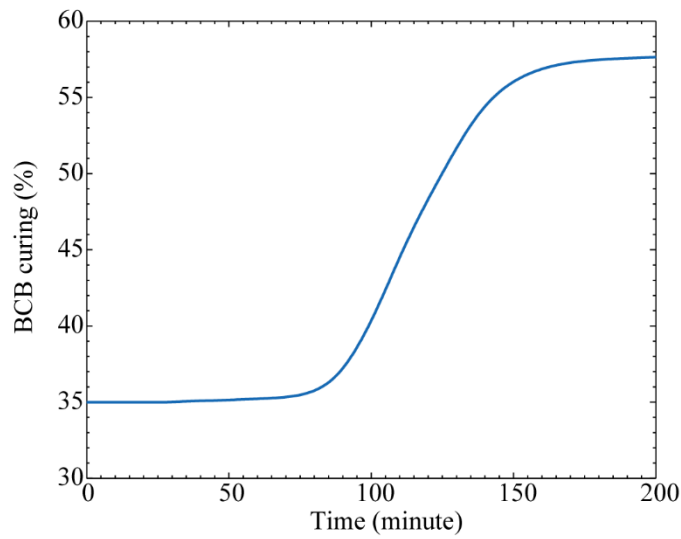
suitable bonding are shown in Table 5.2 and Fig. 5.7. The cavities were realized by etching through the BCB layer after the curing with a spin coating of 4 μm thick Shipley S1827 with a spread speed at 500 rpm for 5 seconds and spin speed at 2500 rpm for 45 seconds followed by a hot plate baking at 115°C for 3 minutes. The 405 nm wavelength UV light exposure dose was adjusted to 480 $\text{mJ}\cdot\text{cm}^{-2}$. The resist was developed for 2.5 minutes in MF319 developer and spin washed in DI water and dried. The etching of BCB was done following STS™ Reactive Ion Etch (RIE) for 4 minutes using 22.5 sccm of CF_4 , 90 sccm of O_2 at a chamber pressure of 50 mTorr and RF power of 200 W. BCB layer was etched down to the top edge of the gold layer to realize the cavity regions. The Shipley S1827 resist was etched at the same rate as the BCB layer. The resist was over exposed to UV light of 1000 $\text{mJ}\cdot\text{cm}^{-2}$. Later the sample was washed in MF319 developer for 10 minutes to remove the remaining resist. The wafer was spin rinsed in DI water, dried, and made ready for bonding with the carrier wafer (bottom electrode).

TABLE 5.2. THE 50-60 % CURING PROFILE FOR BCB

Duration (minute)	Temperature (°C)
1 (multiple purging)	100
39 (Ramp)	150
30 (Soak)	150
35 (Ramp)	195
40 (Soak)	195
Cool down to below 150 °C	



(a)



(b)

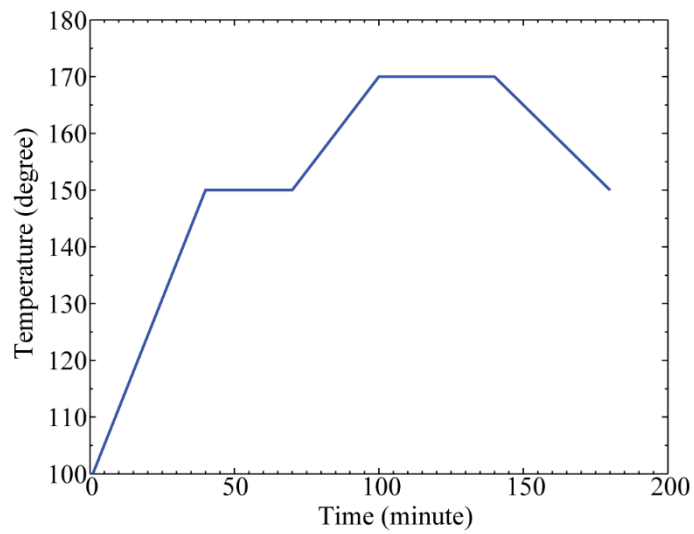
Figure 5.7. (a) Temperature profile, and (b) the corresponding curing level for BCB layer suitable for bonding.

5.5 Preparation of the Carrier Wafer and Realization of Insulation Layer

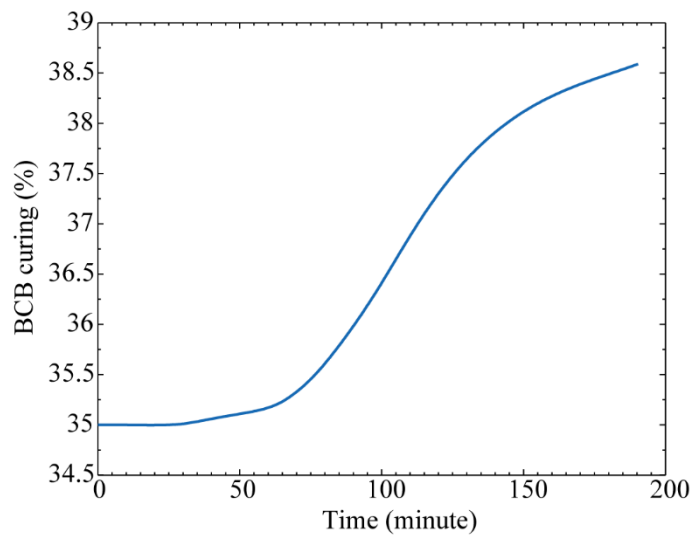
The aim of this step was to prepare the carrier wafer (bottom electrode) for bonding. The process step was started by standard RCA cleaning of a 100 mm diameter 500 μm thick <100> oriented low resistivity boron doped silicon wafer with a resistivity of 0.005-0.01 $\Omega\text{-cm}$. After that, the wafer was cleaned in O_2 plasma for 20 minutes at 10 sccm flow rate, 100 mTorr chamber pressure, and 90 W RF power. The wafer was then rinsed with DI water, dried, and baked in vacuum at 150°C. A 200 nm thick layer of BCB was then spin deposited on the topside at 1:1 dilution of BCB to mesitylene at a spread speed and spin speed of 500 rpm and 5000 rpm for 5 and 45 seconds, respectively. The wafer was then baked on a hot plate at 100°C for 2 minutes as shown in Fig. 5.2(b). The curing profile was derived from Appendix A. According to Table 5.3 and Fig. 5.8, the curing level was very mild at this step. Finally, the wafer was spin rinsed with DI water and dried to make it ready for bonding.

TABLE 5.3. THE 38% CURING PROFILE FOR BCB

Duration (minute)	Temperature (°C)
1 (multiple purging)	100
39 (Ramp)	150
30 (Soak)	150
30 (Ramp)	170
40 (Soak)	170
Cool down to below 150 °C	



(a)



(b)

Figure 5.8. (a) Temperature profile, and (b) the corresponding curing level for BCB layer deposited on wafer 2.

5.6 Adhesive Bonding of the Wafers

The wafer pairs were adhesively bonded as shown in Fig. 5.2(c) and 5.2(e) using a custom-built heated vacuum chuck. Before bringing the wafers into contact, the space between the wafers was evacuated to approximately 10 mTorr. The temperature, pressure, and vacuum levels as a function of time during the bonding process are shown in Fig. 5.9. Under the vacuum, the two halves of the chuck were ramped to 150°C over 30 minutes. Pressure from a hydraulic press was applied for 30 minutes at a rate of approximately 100 psi.min⁻¹ to produce a maximum bonding pressure of 850 psi. The chuck temperature was ramped to the final curing temperature of 230°C in 15 minutes. The chuck was held at 230°C for 60 minutes and then slowly cooled down to below 150°C as the pressure was withdrawn. As the hydraulic press ram diameter was 45 mm, the bonding pressure was equivalent to 2100 lbs.

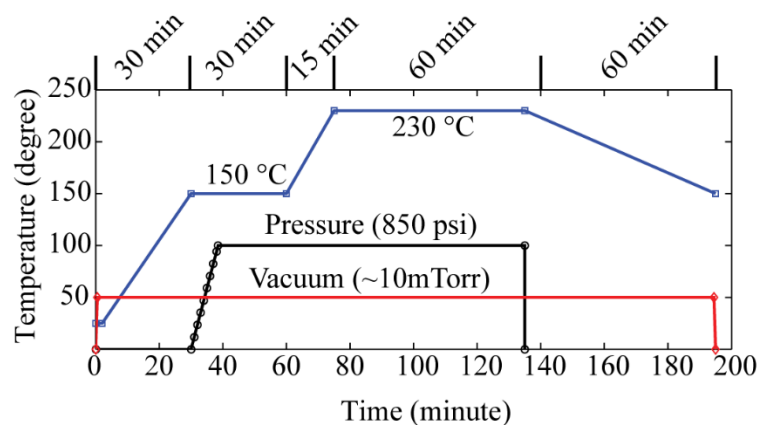


Figure 5.9. Temperature (blue line), pressure (black line), and vacuum (red line) profile.

5.7 Layer Transfer

The aim of this step was to transfer the patterned BCB layer to the carrier wafer as shown Fig. 5.2(d). The process was started by cleaning the back sides of the wafers. It was followed by dry etching of any residual BCB that may be left at the back side of the wafer. The BCB etching was performed for 4min following the recipe mentioned in section 4. Then the 1 μm oxide layer was removed from the backside of the bonded structure by submerging for 15 minutes in buffered HF. Next, the 500 μm thick silicon wafer at the top of the bonded structure was etched by 25% hot KOH (by weight) at 100°C (3L of DI water with 1kg of KOH pellet, and the tank was filled with Ethylene glycol at a temperature of 120°C). An etching paddle from AAMT Germany was used where it exposed the front side of the wafer to hot KOH and protected the back side. In order to avoid any thermal shock to the bonded wafers, the paddle, and the KOH was heated up simultaneously and at the end of the process, the paddle was cooled down before starting any further cleaning process. The total etching time was about 3 hours and 30 minutes if the KOH was freshly made (while it takes 1.17 hours to bring the KOH to its nominal etching temperature). The silicon etching was stopped as soon as the etching reached the oxide layer. After cooling down, the wafer was cleaned with DI water. The exposed 1 μm thick oxide layer was removed using buffered HF again. Finally, the sample was spin rinsed in DI water and dried. About 70% surface of the wafer survived after the bonding process.

5.8 Metallization of Contact Pads and Dicing

The aim of this step was to realize the contact pads for external connectivity of each CMUT element. As the contact pad regions in the gold metallization layer of the bonded structure was then covered by the top BCB layer as shown in Fig. 5.3(a), the first step of this process was to selectively etch the top BCB layer as shown in Fig. 5.3(b) to expose the gold contact pad areas in the gold metallization layer. In the next step Fig. 5.3(c), gold contact pads were to be realized in the contact pad areas using a lift-off process.

The process is started by vacuum baking the sample at 150°C and spin coating of about 3 µm of lift-off resist LOR 30B. The lift-off resist was deposited with a spread speed of 500 rpm for 8 seconds, the spin speed of 3000 rpm for 45 seconds, and baked on a hotplate at 170°C. The process was continued by spin coating of about 8.5 µm of AZ 9260 photoresist using spread speed and spin speed at 500 and 3000 rpm for 5 and 45 seconds, respectively followed by hot plate baking at 110°C for 3 minutes. The wafer was then exposed to 405 nm wavelength UV light at an exposure dose of 1100 mJ.cm⁻². The wafer was developed with mild agitation for 10 minutes in AZ-400K developer. Then the wafer was washed with DI water, spin-rinsed and dried. The 1.5 µm thick BCB layer was etched using BCB plasma etching for 8 minutes following the recipe provided in section 4. The etching time was long enough to ensure the underneath gold contact pad areas are clearly exposed.

The AZ-400K developer was used for much longer time to avoid PG remover as the solvent for the final lift-off process. In order to facilitate the lift-off process, the

wafer was over exposed to UV light with about 2000 mJ.cm^{-2} before the metallization step. The metallization was started by 5 nm titanium evaporation and ended with 400 nm of gold e-beam evaporation. The lift-off process was performed using AZ-400K developer and was completed in 40 hours. Afterward, the wafer was spin-rinsed and dried to complete this process step.

5.9 Die Singulation

To facilitate dicing, the top layer was protected by a spin coating of $4 \mu\text{m}$ of Shipley S1827 first. Later, the dies were sorted and cleaned using double isopropyl alcohol bath and dried overnight in vacuum at 120°C . Numbers of arrays with different operating frequencies have been fabricated following this process that is shown in figure 5.10 after the die singulation.

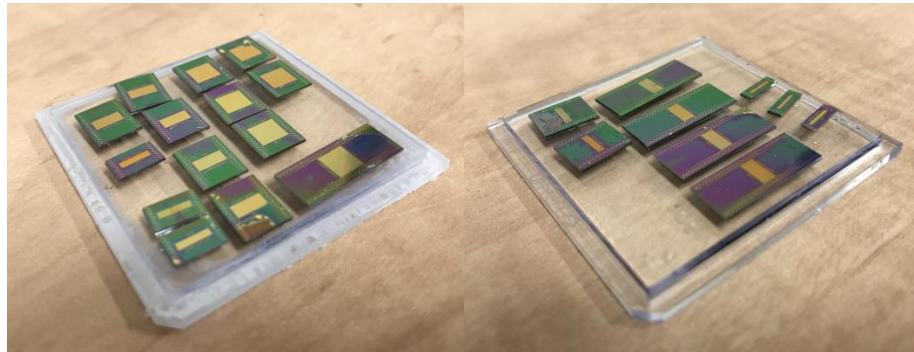


Figure 5.10. Fabricated arrays (8-128elements) for various operating frequencies after dicing and isopropyl alcohol bath.

5.10 Discussion

A new technique of CMUT fabrication has been realized by fabricating 32 elements 40 MHz CMUT linear phased array. Detailed fabrication procedure and preliminary test results are presented. In the new technique, a low-k dielectric material BCB

(dry etched BCB™) has been used to realize the CMUT diaphragm structural material, interelectrode spacer, and the bottom insulation layer. Contrary to conventional fusion bonding, BCB has also been used as the low temperature adhesive bonding agent. Another novel aspect of the realized fabrication process is that the top electrode of the CMUT was fabricated under the diaphragm structural material to result in a higher capacitance change that consequently resulted in a higher sensitivity while isolating the electrical charging effects of the diaphragm material from CMUT operation.

The simple and flexible processing scheme of BCB using existing IC processing techniques makes BCB an excellent candidate to fabricate CMUTs in a conventional IC compatible fabrication processing to achieve long term reliability and stability of operation.

Fabrication Validation & Characterization of the CMUT array

A 32 channel 40 MHz CMUT array has been packaged and wire bonded for the verification of the fabrication process and initial characterization. The CMUT array specifications are listed in Table 6.1.

TABLE 6.1. 32 CHANNEL 40 MHz CMUT ARRAY SPECIFICATIONS

Parameters	Value	Unit
<i>Array</i>		
Aperture size	0.62	mm
Number of elements	32	
Element pitch	150	μm
Kerf width	8.75	μm
Fill factor	53.33	%
No. of cells per element	266	
<i>Individual cell</i>		
Diaphragm sidelength	10	μm
Diaphragm thickness	1500	nm
Cavity height	0.75	μm
Top electrode thickness	100	nm
Resonant frequency	40	MHz
Coupling coefficient (calculated)	0.63	
Static capacitance (calculated)	4.5	pF

The following sections provides a thorough SEM inspection of different parts of the array to verify the fabrication accuracy and preliminary characterization results that validate the improvements of CMUT performance in terms of transduction efficiency.

6.1 SEM Inspection and Fabrication Validation

About 70% surface of the wafer survived after the bonding process. An optical microscopic image of a section of the array is shown in Fig. 6.2.

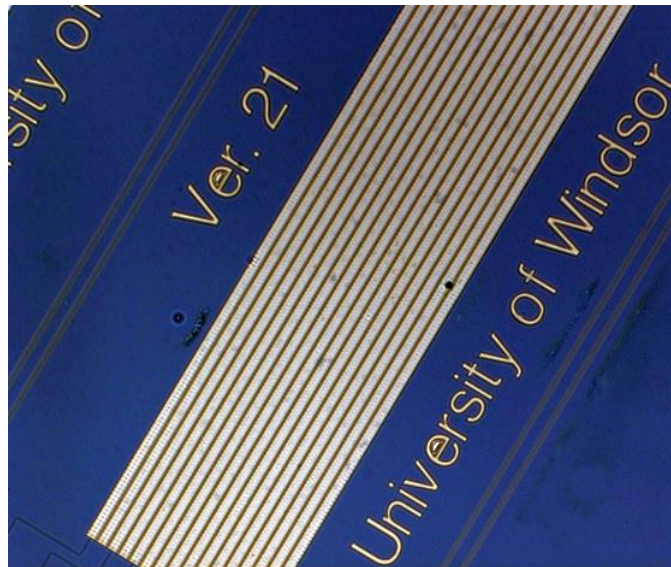
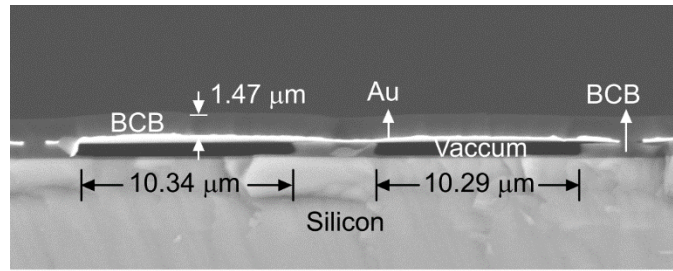
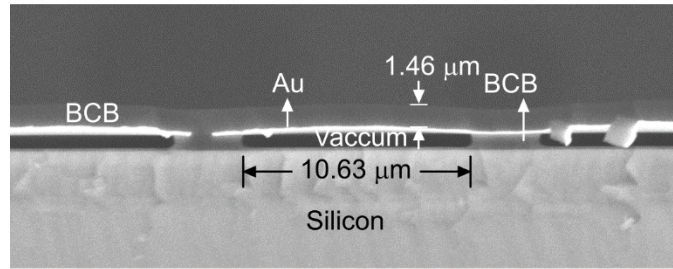


Figure 6.1. Top metallization of a section of a linear array.

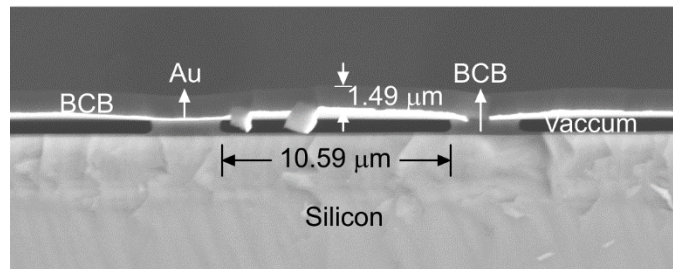
After the layer transfer, cross-sectional SEM images were taken from different parts of the array that are shown in Fig. 6.2.



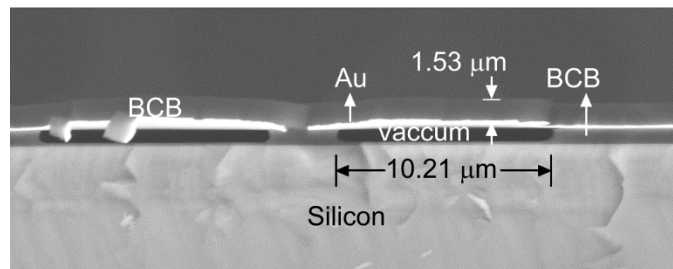
(a)



(b)



(c)



(d)

Figure 6.2. Cross-sectional SEM images of the fabricated CMUT elements each consists of 2 CMUT diaphragms along the lateral direction after the adhesive wafer bonding.

The average diaphragm sidelength was $10.41\ \mu\text{m}$ based on the SEM measurements with a deviation of 3.9% from the proposed design. Individual cell sidelength are slightly larger than the designed one due to the 5% shrinkage of BCB interelectrode posts during the curing process.

A surface topography of a portion of the array is shown in figure 6.3 followed by SEM images of the routing traces and contact pad in figure 6.4. Based on the array topography, average element width is $150\ \mu\text{m}$ with 8 cells in each row and the average kerf width is $8.7\ \mu\text{m}$.

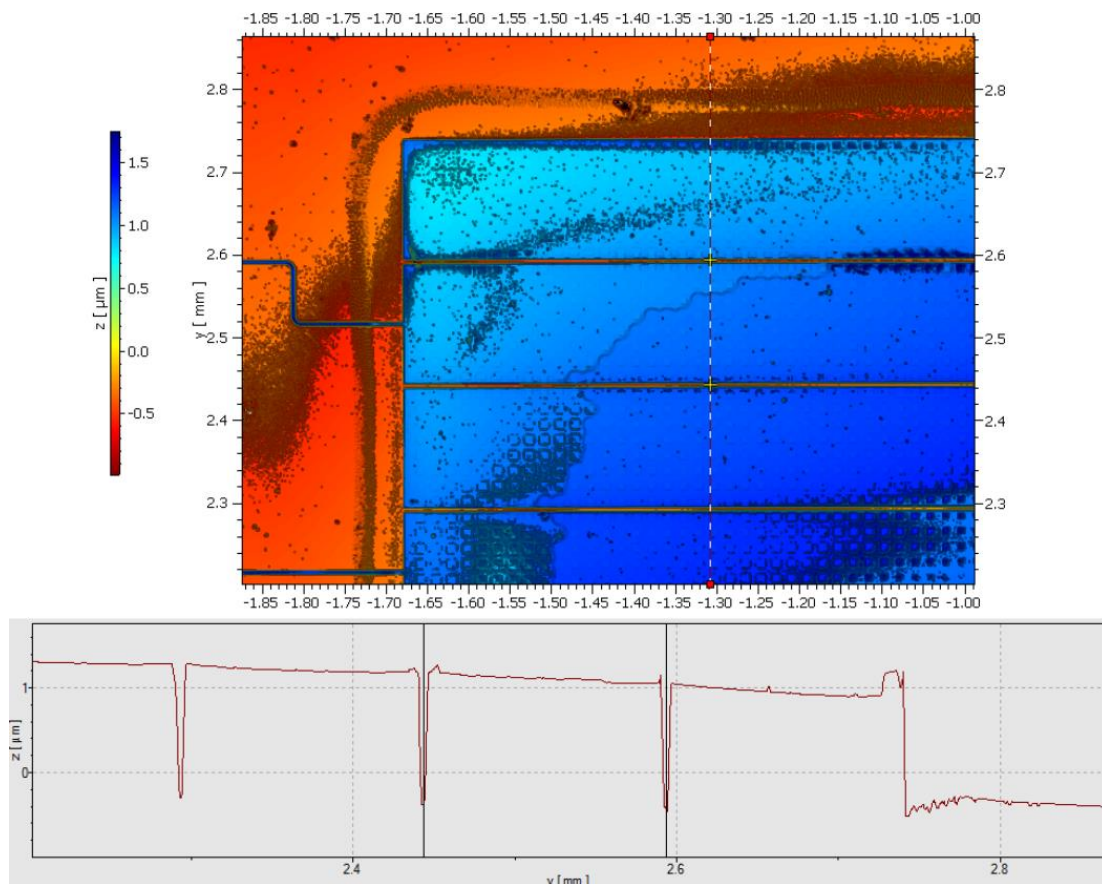
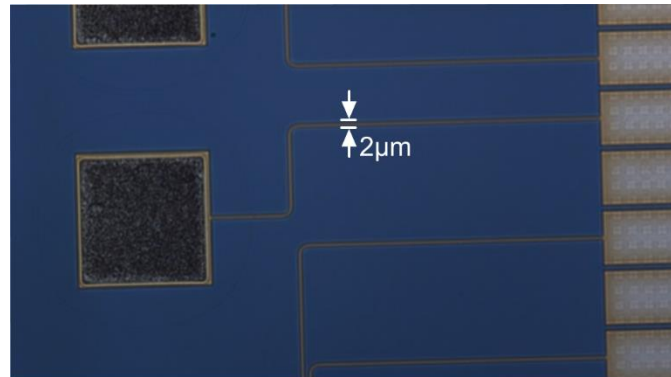
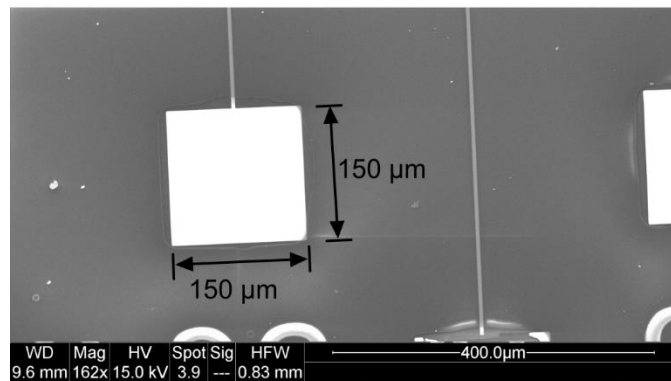


Figure 6.3. Surface topography of a portion of the 40 MHz CMUT linear phased array.



(a)



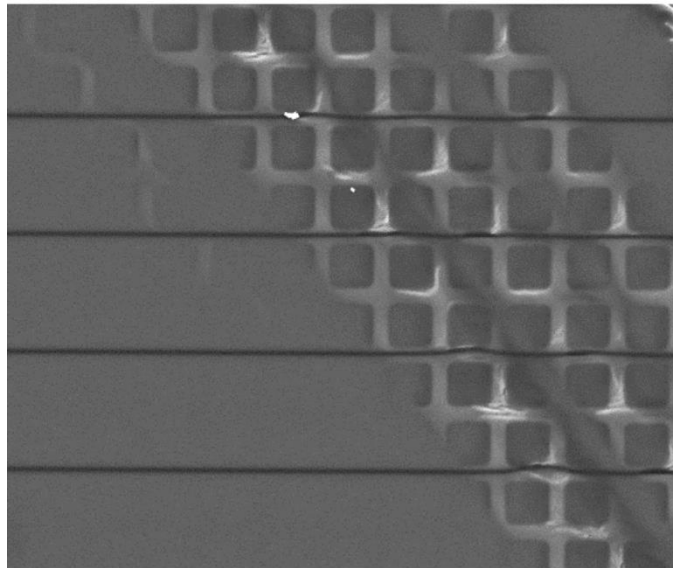
(b)

Figure 6.4. SEM images of (a) 2 μm wide conductive traces to individually access elements, and (b) 150 x 150 μm^2 contact pads for wire bonding.

In Fig. 6.5 (a) and (b), a portion of the diced array that clearly shows the cavity shape before and after scratching out the top BCB and gold layer with numbers of cells in each element. In Figure 6.4 (b), the top layer BCB and Gold was scratched out using tweezers randomly to expose the square shaped cavity beneath it.



(a)



(b)

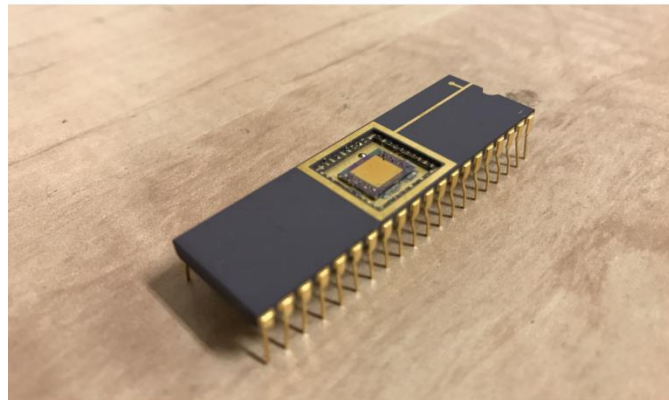
Figure 6.5. Optical images of diced diaphragms with cavities underneath.

6.2 Packaging of the Array and Wirebonding

The fabricated 40 MHz 32 channel linear array was mounted in a CSB04075 40 pins DIP package. The array was initially attached to the center base using silver conductive epoxy to act as the ground plane. The epoxy was a mixture of part A and part B as shown in figure 6.6 (a) at 1:1 ratio. While wire bonding using F&K Delvotec manual wire bonder 5310 series, most of the gold pads came off from the contact pad area due to poor adhesion between 500 nm gold and BCB as shown in figure 6.7. Further investigation is in progress.

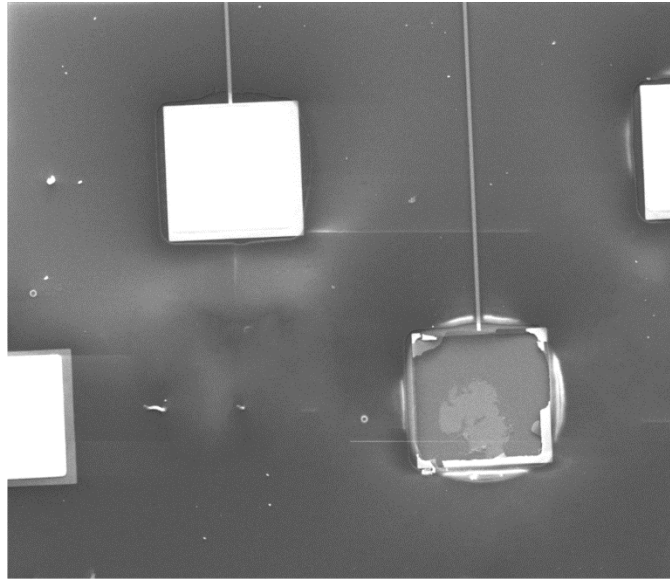


(a)

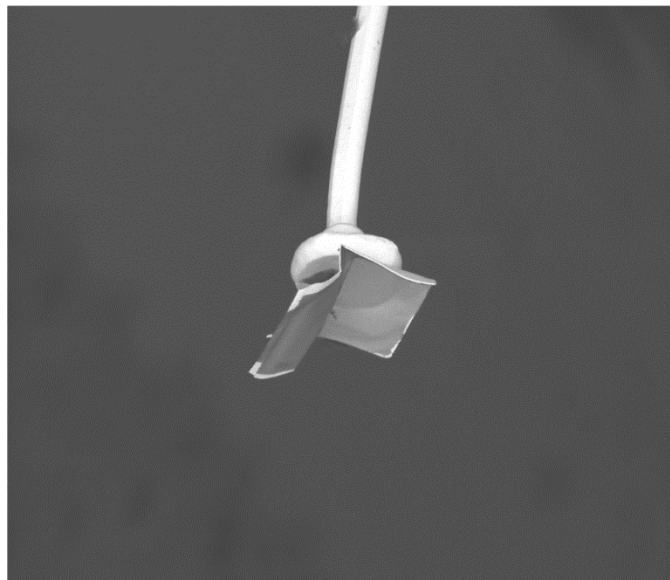


(b)

Figure 6.6. (a) Silver conductive epoxy part A and part B, and (b) array glued to the base of the package using the epoxy mixture of 1:1 ratio.



(a)



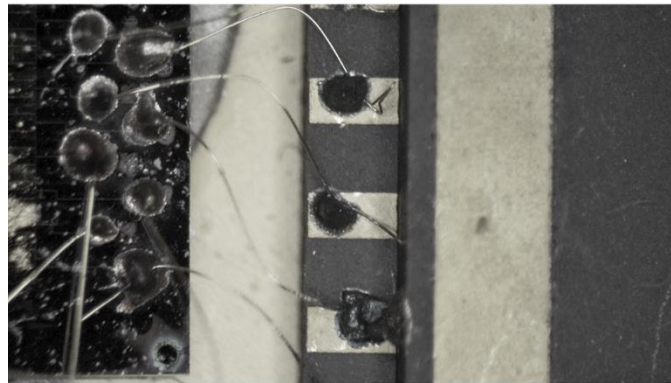
(b)

Figure 6.7. (a) Damaged contact pad while wire bonding, and (b) the detached gold pad from the contact pad area along with the 28 μm thin bonded wire.

An alternative way has been developed to wire bond manually by depositing silver conductive epoxy (EPOTEK 12670 EE) in the damaged contact pads and inserting gold bonding wires into the silver epoxy under a microscope for test and measurement purposes. A section of the contact pad area is shown after wire bonding using the epoxy in figure 6.8.



(a)



(b)

Figure 6.8. CMUT contact pads wire bonded to the package using EPOTEK 12670 EE silver conductive epoxy.

6.3 Static Characterization of the Fabricated CMUT Structure

6.3.1. Electrical Input Impedance Measurement

The natural frequency of the array was measured using an Agilent 5061B Vector Network Analyzer (VNA). Individual array elements were connected to port 1 of the VNA and the S_{11} parameters were measured and converted to Z-parameters. The measurement setup is shown in figure 6.9. Electrical input real and imaginary impedances as a function of the frequency of one of the elements are shown in Fig. 6.7. The magnitude of the real impedance reaches a maximum of 185 k Ω at anti-resonance of 79.7 MHz and a minimum at the series resonance of 48.1 MHz. Experimental values are slightly different from 40 MHz obtained from FEA simulation carried out by IntelliSuite™ and the analytical model developed in MATLAB®. Apparently, this deviation is due to the slight difference in the top electrode and diaphragm thickness as shown in Fig. 6.1.

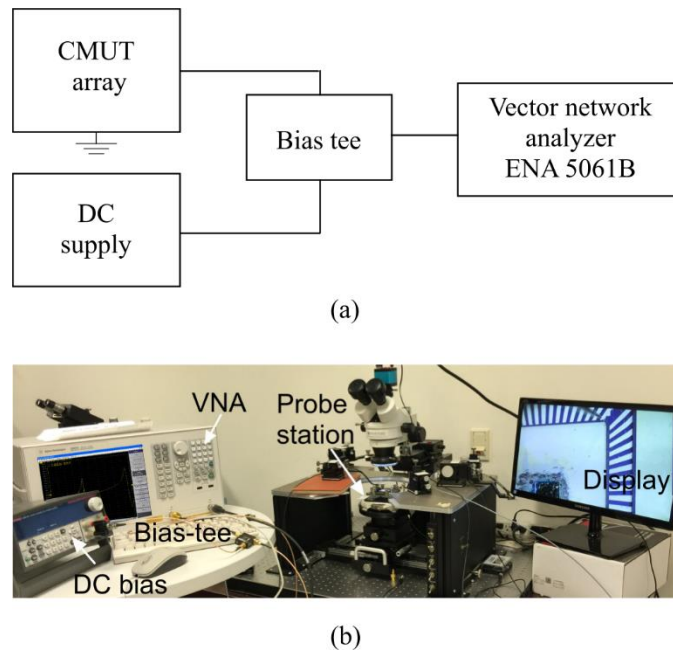


Figure 6.9. Vector Network Analyzer (VNA) setup for electrical input impedance measurement (a) schematic, and (b) experimental.

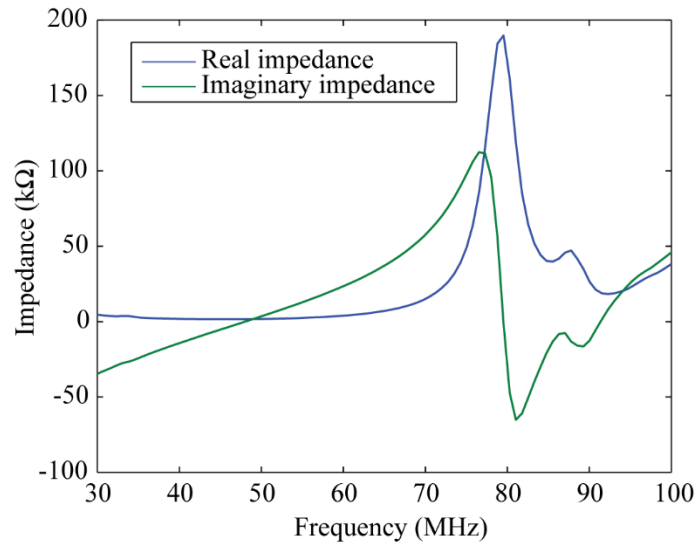
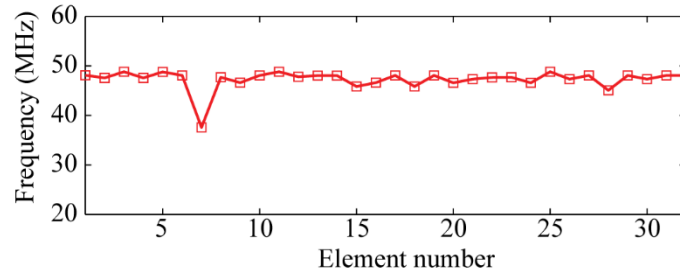


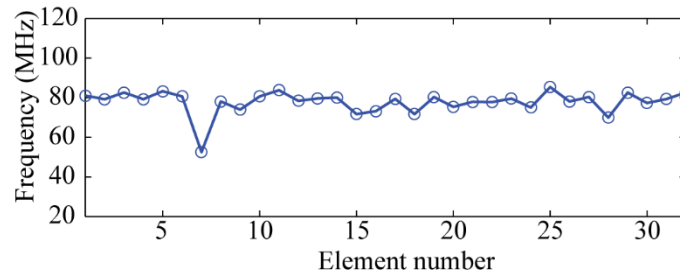
Figure 6.10. Real and imaginary electrical input impedance as a function of frequency measured using vector network analyser, applied DC bias 20 V.

6.3.2. Series and Parallel Resonance

The series resonance in Fig. 6.8(a) was extracted from the x-axis zero crossing imaginary impedance curve and the parallel resonance in Fig. 6.8(b) was extracted from the peak values of the real impedance curve of respective elements. Apparently, this variation of natural frequency is due to the non-uniform CMUT diaphragm thickness. The relative standard deviation has been calculated to be 3.2% across the array. The electromechanical coupling coefficient was calculated as 0.66 based on series and parallel resonance that is ~50% higher than that of as reported in [6, 36] and a deviation of 4.7% from analytical values carried out by the authors [30].



(a)



(b)

Figure 6.11. (a) Series and (b) parallel resonance of the array elements measured using VNA 5061B.

6.3.3. Static Capacitance Measurement

An Agilent U1733C handheld LCR meter was used to measure the static capacitance of the elements at a low frequency of 100 Hz and compared with the extracted capacitance values from impedance curves and calculated results from the mathematical model. Average static capacitance across the array was measured to be 5.26 pF with a standard deviation of 0.78 pF and 0.85 pF from extracted and calculated value, respectively. The variation in static capacitance shown in Fig. 6.9 is due to the parasitic capacitance of the DIP package and probe settings.

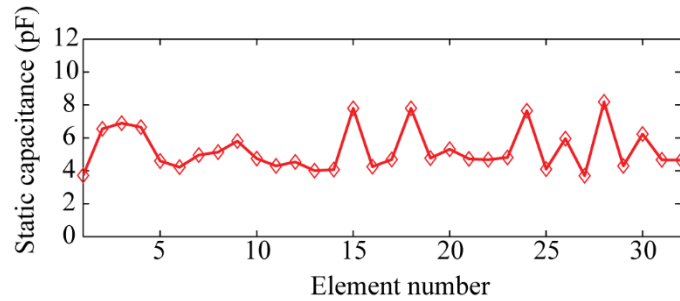


Figure 6.12. Static capacitance across the array element using LCR meter.

6.3.4. Frequency drift and the effect of bias voltage

The resonant frequency drift with time has been experimentally characterized and compared with silicon diaphragm with BCB insulation layer and silicon diaphragm with silicon dioxide insulator which were fabrication in our lab for different applications. All three CMUT arrays were connected to VNA and biased at 50 V. The measurement readings were taken for 24 hours. The first reading was at the beginning of the experiment. The second and third reading was after 2 hours and 10 hours. Then final reading was taken after 24 hours. The resonant frequency drift with time for three different diaphragm based CMUT has been shown in Figure 6.10 (a, b and c). The corresponding resonant frequencies can be extracted from the intersection of the dotted and the solid lines. A portion of the impedance curve is shown to better visualize the frequency drift. Table 6.2 shows a comparison of the percent drift with time between the BCB, silicon and silicon nitride based CMUT diaphragms.

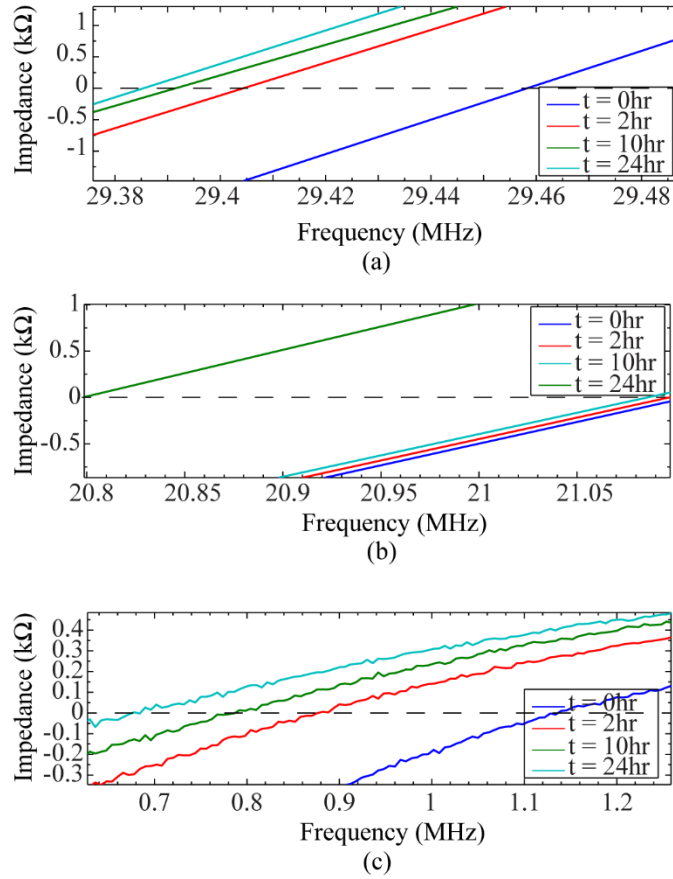


Figure 6.13. Frequency drift with time for (a) BCB, (b) Silicon and (c) Silicon nitride based diaphragm.

TABLE 6.2. COMPARISON OF RESONANT FREQUENCY DRIFT IN MHZ WITH TIME

Diaphragm material	Insulation material	t = 0	t = 2 hrs	t = 10 hrs	t = 24 hrs
		Frequency (MHz)			
BCB	<i>BCB</i>	29.46	29.44	29.40	29.35
Percentage drift			0.067	0.20	0.37
Silicon	<i>BCB</i>	21.12	21.11	21.08	20.08
Percentage drift			0.047	0.19	4.92
Silicon	<i>Silicon dioxide</i>	1.11	0.87	0.79	0.68
Percentage drift			21.6	27.9	49.7

From Table 6.2, the effect of using BCB on the reduced frequency drift is evident. BCB as only insulation layer reduced the drift by 90% as compared to the oxide based insulation layer. When BCB was used as the diaphragm the drift got further reduced by 92.4%. The CMUT array was initially biased at 30 V and then increased to 40 V and 50 V to visualize the effect of spring softening. Due to spring softening effect the resonant frequency decreases which has been shown in Figure 6.11.

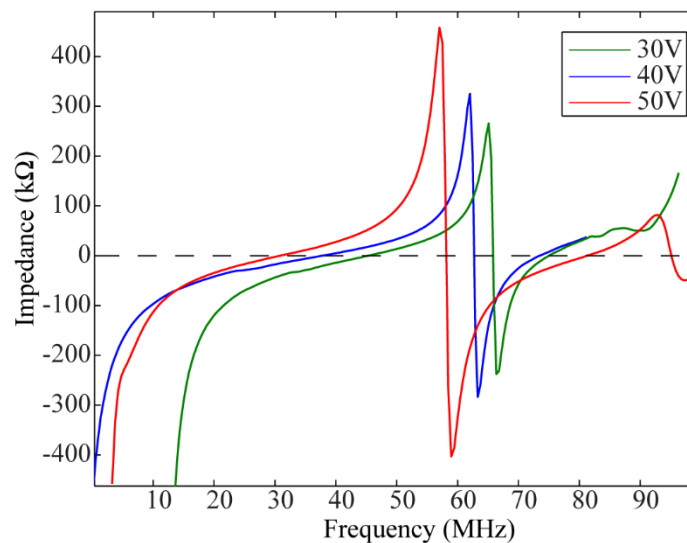


Figure 6.14. Spring softening effect on the frequency as function of bias voltage at 30 V, 40 V and 50 V.

At 30 V the resonant frequency was at 45.6 MHz. After increasing the bias to 40 V the series resonance shifts to 38.31 MHz with a decrement of 15.9%. Later the bias voltage was increased to 50 V and the resonance shifted down to 29.8 MHz (22.2%).

6.4 Experimental Analysis using Laser Doppler Vibrometer

A laser doppler vibrometer Polytec MSA-500 has been used to characterize the deflection under DC bias and small AC signal. It was also used to analyze the out of plane vibration and velocity. The equipment has a maximum limit of upto 20 MHz displacement decoder. For which, a different CMUT linear array with a resonant frequency of 10 MHz that has been fabricated following the process presented in chapter 5 has been characterized to validate the CMUT operation. The array under the test was designed to have square shape diaphragms with the same thickness of the layers as mentioned in table 6.1. The sidelength was changed to have 22 μm to achieve the resonant frequency.

6.4.1. Surface Topography

Surface topography measurement of the CMUT cells was carried out using a white light interferometer (Polytec MSA-500). The travel range was calibrated before taking the measurements to achieve maximum displacement. The measurement was done in short coherent mode at 0 V bias voltage. The topography was measured at every 100 nm and plotted as a 3D map. A three dimensional surface topography of a section of the CMUT array is shown in Figure 6.15. The diaphragm bending due to atmospheric pressure was captured along the dotted scan line. The average sidelength of the diaphragms is measured to be 23.4 μm with kerf width of 7.2 μm .

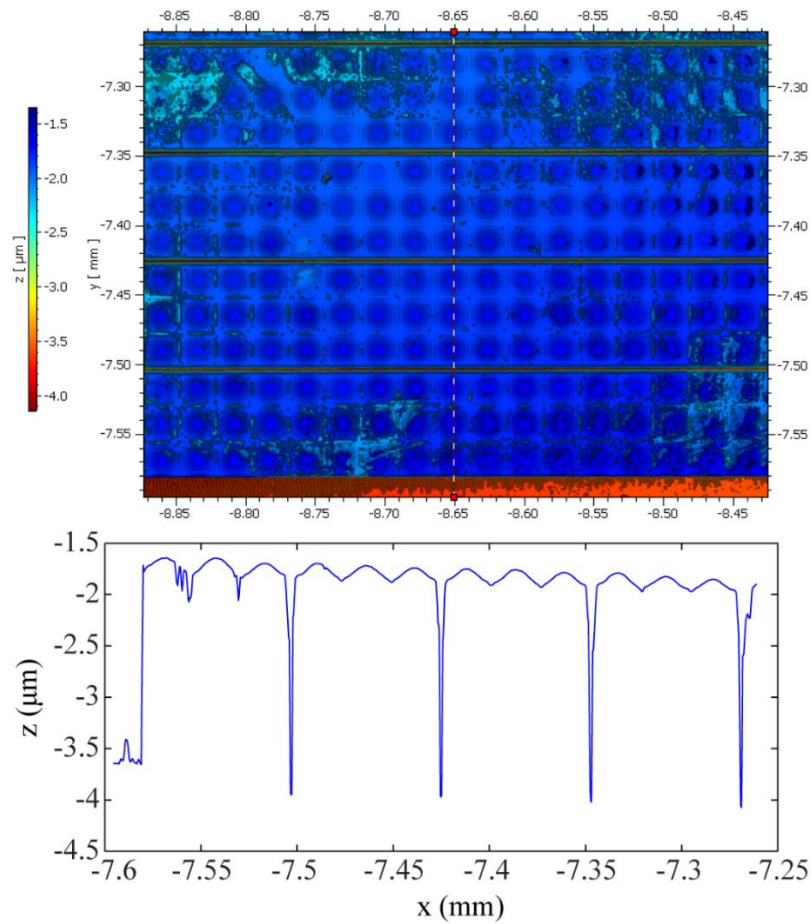


Figure 6.15. Surface topography of a portion of the CMUT array.

6.4.2. Deflection Profile

The experimental setup of measuring the CMUT diaphragm deflection due to DC bias using the laser Doppler vibrometer is shown in figure 16.6. A 3D map and a corresponding 2D plot of deflection profile along the dotted scan line is shown in figure 6.17. From Figure 6.17, an average deflection was measured to be $0.4 \mu\text{m}$.

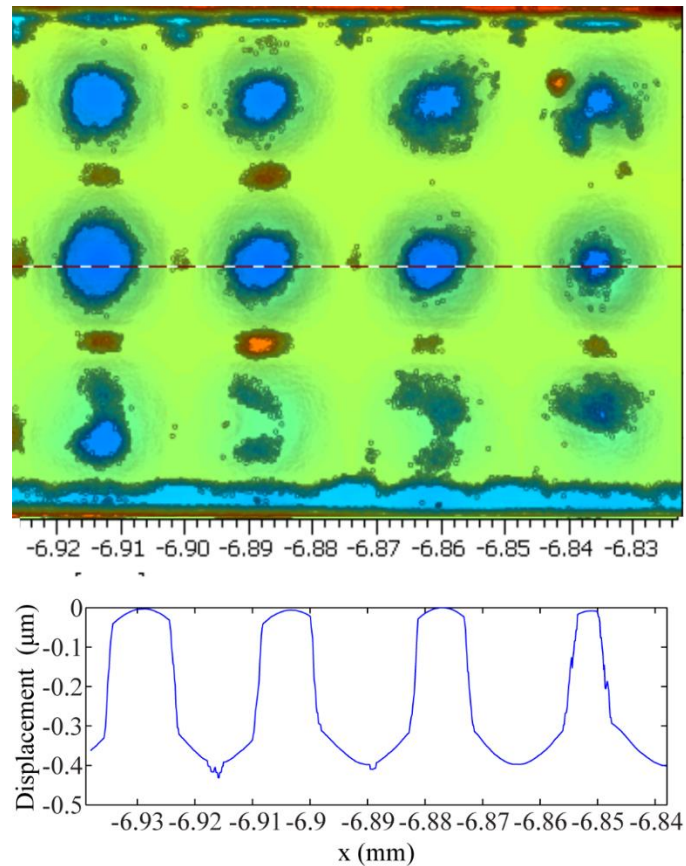


Figure 6.16. 60 V DC bias deflection of CMUT diaphragms measured using a Polytec MSA-500 laser Doppler vibrometer.

6.4.3. Out of Plane Measurement

The out of plane measurement of the CMUT array while operating in air has also been carried out, where a 10 V chirp signal with a frequency range from zero to 15 MHz has been applied along with 10 V DC bias. The maximum displacement is supposed to occur at the resonance. A 3-D snapshot of a section of the array with vibrating diaphragms was captured from Polytec MSA-500 laser Doppler vibrometer and is shown in Figure 6.18 (a) and (b). In figure 6.19, the maximum

deflection of the diaphragm center has been measured as 3.48 picometers at 10.13 MHz and compared with the FEA simulation that shows a deviation of 0.5%.

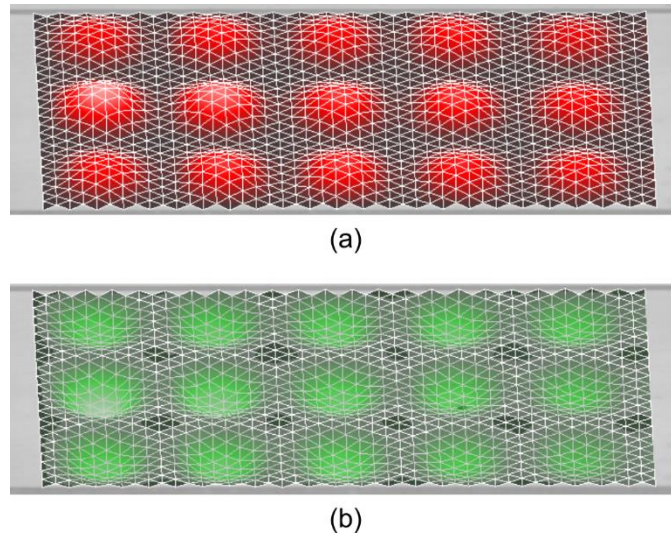


Figure 6.17. 3D snapshot of the out of plane vibration of the CMUT cell diaphragms.

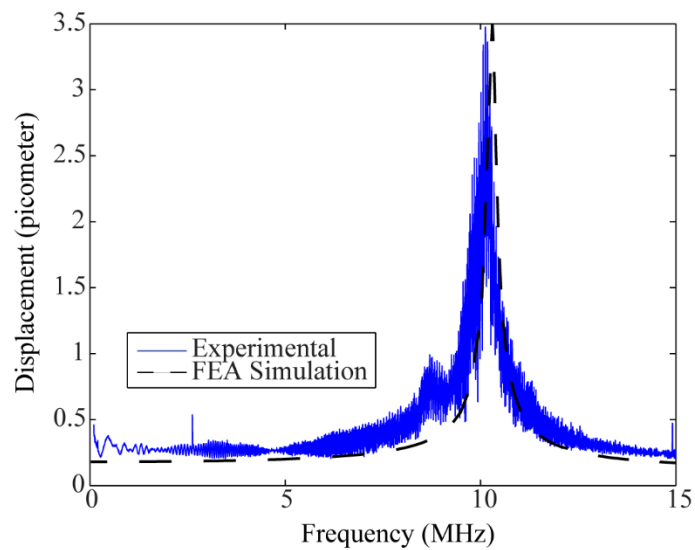


Figure 6.18. Diaphragm displacement as a function of frequency validating the resonance at 10.13 MHz with a peak deflection.

6.4.4. Velocity Measurement

The velocity of a single cell diaphragm has been measured. A 10 V_{p-p} sine wave signal was applied at different frequencies ranging from 0-15 MHz. For each frequency the velocity is measured and plotted continuously. A 2D plot of the measurement is shown in figure 6.20. Maximum velocity of 220.9 $\mu\text{m}\cdot\text{s}^{-1}$ can be observed at the resonant frequency with a comparatively very low amplitude harmonic near 15 MHz.

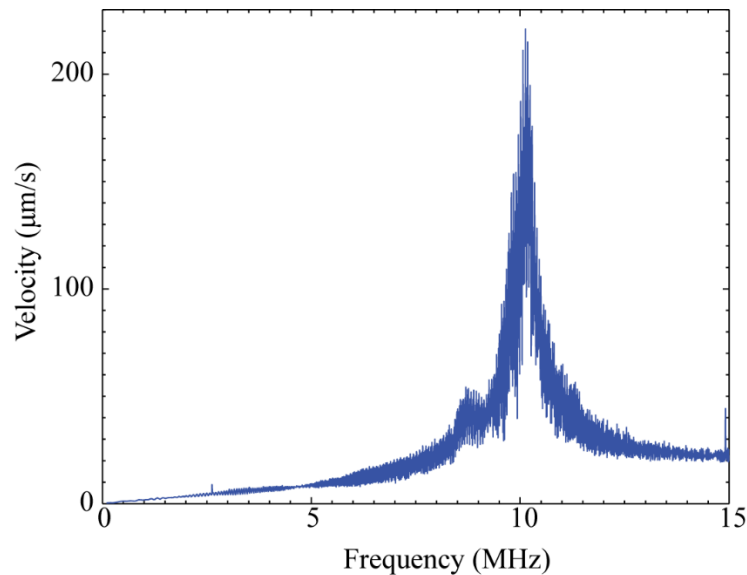


Figure 16.19. Velocity measurement of CMUT diaphragm.

6.5 Discussion

The fabrication process has been validated by inspecting different sections of the array based on SEM images. It was observed that the adhesion of gold metal pads deposited on metal contact pad area of the CMUT top electrode was not adequate and got detached in most cases during wire bonding using an F&K Delvotec™ wire bonder. The investigation is underway to resolve the issue.

The preliminary characterization of the fabricated CMUT array exhibits superior performance with a high electromechanical coupling coefficient. As BCB has very low ionic contaminations, the electrical charging effects can be expected to be much lower as compared to CMUTS fabricated with other dielectric materials as has been experimentally verified with the newly fabricated CMUT array. Higher coupling coefficient of 0.66 as compared to 0.294 [6] at the same bias voltage is an indication of lower electrical charging.

The experimental results are promising to carry out a further investigation for the ophthalmic imaging application. The measured static capacitance of individual cell is in excellent agreement with the 3-D FEA model with a deviation of 1.27%. Slight variation in the diaphragm thickness could be a reason that might lead to a difference between FEA simulation and experimental results for the resonant frequency (measured standard deviation of 3.2% across the array) and the electromechanical coupling coefficient (4.7% deviation from FEA). The layer swelling that occurred as PG remover diffused into BCB layer, especially at the edge of the patterns might be a reason that contributed to the variation in diaphragm thickness. Also, the dielectric post sidewalls were slightly curved due to the RIE process of the 750 nm BCB layer that leads to a variation in the effective sidelength of the CMUT. However, the fabrication process provides a much simpler and cost-effective approach to realize the CMUT array structure and high uniformity throughout the array as well. The experimental analysis of the frequency drift verifies the effect of using BCB as a solution to the charging and drift issues typically observed in existing CMUT probes.

Perspective, Summary and Future Direction

7.1 Perspective

The emerging capacitive micromachined ultrasonic transducers (CMUT) technology offers a superior method of ultrasound generation and detection as compared to the conventional piezoelectric transducers. Global research efforts are underway to make this technology available commercially for biomedical diagnostics and non-destructive testing and to replace the conventional piezoelectric transducers. However, based on the literature review, the dielectric charging is a common phenomenon in CMUT and one of the barriers to make this technology commercially viable. Though it has been addressed as one of the prime issues to be resolved, very few attempts have been taken so far which are case specific that impose further complexity in terms of fabrication as well as operation. This dissertation work was started with a goal to reduce the charging effect. In order to achieve that, in depth review of the existing research work on CMUT charging effect was done first to find out different sources of this dielectric charging. The output of the review indicates that the presence of ionic contamination, occurrence of the dipole randomization and existence of trapped charges lead to change the characteristics of dielectric materials typically used in realizing the CMUT membrane, spacer and insulation layer. Inconsistency in the dielectric properties is more prevalent under the applied electric field during the operation and causes to change the DC operating point. At an increased DC bias

voltage, a shift in the electric field could reduce the CMUT electromechanical coupling efficiency and even can cause the device to collapse in a premature way.

The electrical, mechanical, and thermal properties of Cyclotene™ are superior to the conventional bonding and dielectric materials as it has been characterized with a low loss tangent, low dielectric constant, low moisture absorption, low out-gassing, low curing temperature, excellent planarization, and very low dielectric constant variation over a wide frequency range. The dry etching capability of Cyclotene 3000™ is among the most interesting features for wafer bonding as it can be patterned easily using standard photolithography techniques. While ensuring a firm bond with a fracture strength as high as silicon, a Cyclotene 3000™ layer can also function as an electrical and thermal isolation layer between two bonded surfaces.

The idea of replacing the typical CMUT membrane material with BCB came from the improved transduction efficiency of the second generation CMUT designed in our lab as compared to the silicon dioxide and nitride based CMUTs where BCB was used only as the dielectric spacer and insulation layer. With this motivation, BCB membrane based CMUT linear phased array for possible ophthalmic anterior segment imaging was designed and fabricated with a goal to achieve reduced dielectric charging and improved transduction efficiency at a lower bias voltage.

7.2 Summary and Discussion

Design concept and analysis of a high frequency 40 MHz BCB diaphragm based 128 elements CMUT phased array has been presented. The designed array was compared to other published experimental results of linear phased arrays for similar application specifications. This array design is capable of exhibiting better lateral resolution with smaller active aperture size, and providing higher fractional bandwidth for ophthalmic imaging. Cell diaphragm was designed using BCB polymer and the top electrode was placed beneath the diaphragm to reduce the dielectric charging problem in CMUTs and improve the transduction efficiency further. This proposed design to achieve high coupling coefficient at low bias voltage will open up the possibility to increase the sensitivity and the dynamic range of the CMUT operation to emit and receive high acoustic pressure at a low operating voltage.

A new technique of CMUT fabrication has been realized by fabricating 32 elements 40 MHz CMUT linear phased array. Detailed fabrication procedure and preliminary test results are presented. In the new technique, a low-k dielectric material BCB (dry etched BCB™) has been used to realize the CMUT diaphragm structural material, interelectrode spacer, and the bottom insulation layer. Contrary to conventional fusion bonding, BCB has also been used as the low temperature adhesive bonding agent. Another novel aspect of the realized fabrication process is that the top electrode of the CMUT was fabricated under the diaphragm structural material to result in a higher capacitance change that consequently

resulted in a higher sensitivity while isolating the electrical charging effects of the diaphragm material from CMUT operation.

The simple and flexible processing scheme of BCB using existing IC processing techniques makes BCB an excellent candidate to fabricate CMUTs in a conventional IC compatible fabrication processing to achieve long term reliability and stability of operation. As BCB has very low ionic contaminations, the electrical charging effects can be expected to be much lower as compared to CMUTS fabricated with other dielectric materials as has been experimentally verified with the newly fabricated CMUT array. Higher coupling coefficient of 0.66 as compared to 0.294 [6] at the same bias voltage is an indication of lower electrical charging. Further investigation is in progress in this regard.

The fabrication process has been characterized by inspecting different sections of the array based on the SEM images. During fabrication, the curing level was balanced within the allowable reactivity range of the BCB for bonding while minimizing the amount of flow during the bonding process under vacuum to maintain pattern fidelity. It was also observed that the adhesion of gold metal pads deposited on metal contact pad area of the CMUT top electrode was not adequate and got detached in most cases during wire bonding using an F&K Delvotec™ wire bonder. The investigation is underway to resolve the issue.

The preliminary characterization of the fabricated CMUT array exhibits superior performance with a high electromechanical coupling coefficient. The experimental results are promising to carry out a further investigation for the ophthalmic imaging

application. The measured static capacitance of individual cell is in excellent agreement with the 3-D FEA model with a deviation of 1.27%. Slight variation in the diaphragm thickness could be a reason that might lead to a difference between FEA simulation and experimental results for the resonant frequency (measured standard deviation of 3.2% across the array) and the electromechanical coupling coefficient (4.7% deviation from FEA). The fabricated CMUT array has been compared two different silicon diaphragm based arrays with BCB and silicon dioxide insulating layers to characterize the effect of using BCB diaphragm on the resonant frequency drift with time. The experimental results after 24 hours indicate excellent stability and ~90% less frequency drift in the case of a BCB based diaphragm along with BCB as insulating layer and dielectric spacers. The spring softening effect is 15-20% when the bias voltage was increased gradually from 30V to 50V. The layer swelling that occurred as PG remover diffused into BCB layer, especially at the edge of the patterns might be a reason that contributed to the variation in diaphragm thickness. However, the fabrication process provides a much simpler and cost-effective approach to realize the CMUT array structure and high uniformity throughout the array as well. The fabrication process presented in this paper can also be utilized to realize CMUT arrays for other applications operating at different centre frequencies. Further characterization measurements of the fabricated array are in progress.

7.3 Future Directions

7.3.1. Contact Pads and Wirebonding

In the fabricated CMUT arrays, the gold layer deposited in the contact pad region did not have sufficient adhesion to the BCB layer to withstand the bonding force and the gold layer was coming off of the surface. As a result, silver conductive epoxy was deposited manually with a gold wire inserted in the epoxy before it gets fully cured. Even though that approach worked out to access the individual elements, this method is rudimentary and time consuming. The epoxy on contact pads located on each side of the array elements took two days to get cured and bonded to the package. Above all, the uniformity across the contact pads was compromised due to the manual deposition of the epoxy and many a time, adjacent contact pads got shorted due to the uncured epoxy. Added thickness contributed to the increase in parasitic capacitance and stiffness. It can be solved following different approaches. The 1500 nm BCB layer required to be cured more and that will increase the adhesion to the gold layer. Another possible approach could be plasma etching of the top BCB layer to realize a 1.5 μm deep and $\sim 20 \mu\text{m}$ trench outside the active array area instead of the $150 \times 150 \mu\text{m}^2$ etching of the BCB layer as shown in figure 5.3(b). That could be followed by filling up the trench with gold layer and with an additional mask, contact pads can be realized on top of the BCB layer as shown in figure 7.1 (a and b). A thin layer of chromium can be deposited in the contact pad region before depositing gold to increase the adhesion between gold and BCB.

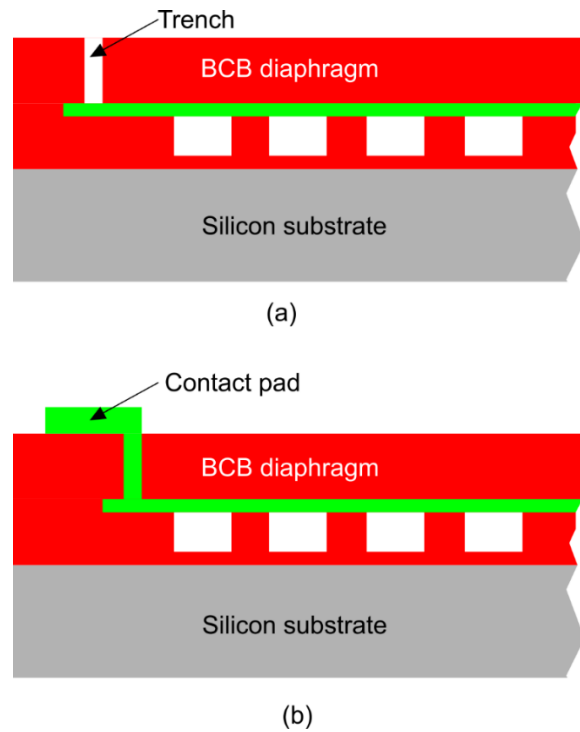
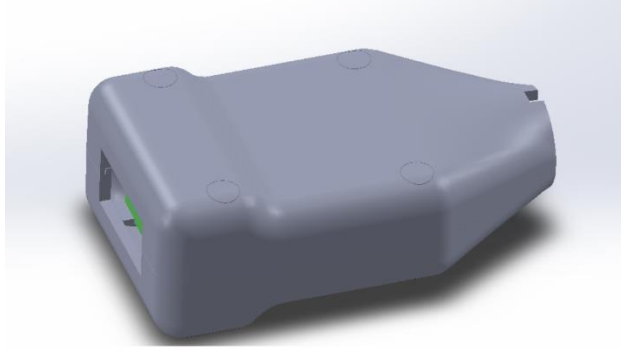


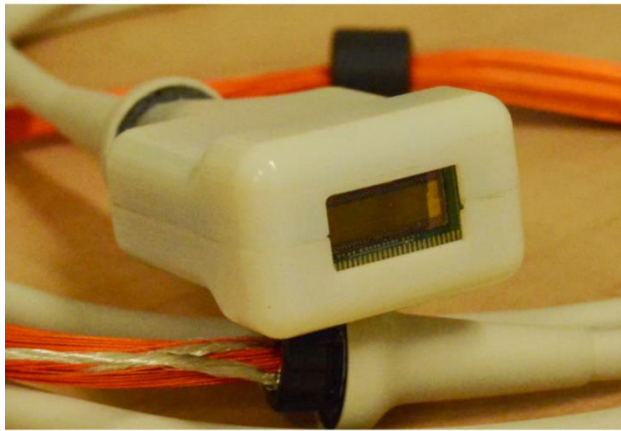
Figure 7.1. (a) 1.5 μm deep 20 μm narrow trench for routing and (b) gold contact pad adhered to BCB layer.

7.3.2. Probe Design, Fabrication and Characterization

A proto type model of a hand-held probe was designed and fabricated to accommodate the array and two readout circuitry. As shown in Figure 7.2 (a and b), the probe casing was designed in SolidWorks and 3D printed using polyjet process and made of vero white plus material. The two readout circuitry are based on 8 layer rigid pcb design consisting of 8 MAX4805A low-noise amplifier as shown in Figure 7.3. The probe cable from TE Connectivity can accommodate 128 channel with 4 individual connectors on each side having 35 pins in each of them. The array was mounted on a separate pcb board and connected to two readout circuitry using right angled connectors. The readout circuitry can be implemented on a flex pcb where the array can be mounted also to reduce the



(a)



(b)

Figure 7.2. (a) 3D design of the probe casing in SOLIDWORKS and (b) 3D printed probe head from PROTO 3000.

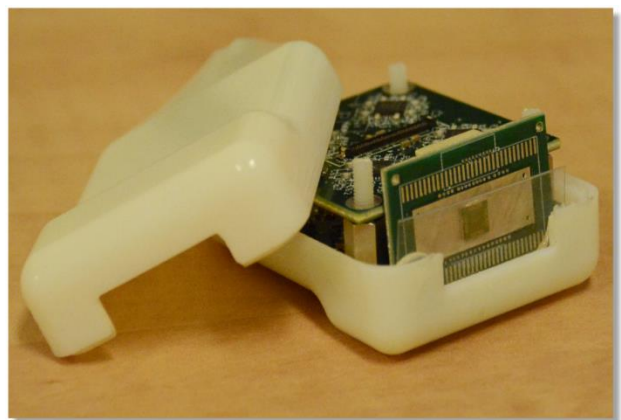


Figure 7.3. 8 layer PCB design of readout module with the CMUT array carrier board.

size of the overall probe and reduce the unwanted parasitic capacitance by avoiding long signal traces and impedance mismatch. The probe is required to be tested in air and oil medium to characterize. To do so, a customized breakout board is needed to be designed and manufactured that will have the 256 pin Canon connector, DC bias supply and AC signal traces from Vantage 128. A preliminary PCB design is shown in figure 7.4. Both the designs of readout and breakout module can be used as rapid development board for future probe integration. Furthermore, a fabrication process can be developed for in-situ encapsulation of the probe head for the immersion characterization so that the fabricated arrays can be characterized experimentally for ophthalmic application. In house cleanroom will be of great advantage for the future researchers in our lab to implement the suggested approaches, debug and resolve the difficulties faced during the fabrication process.

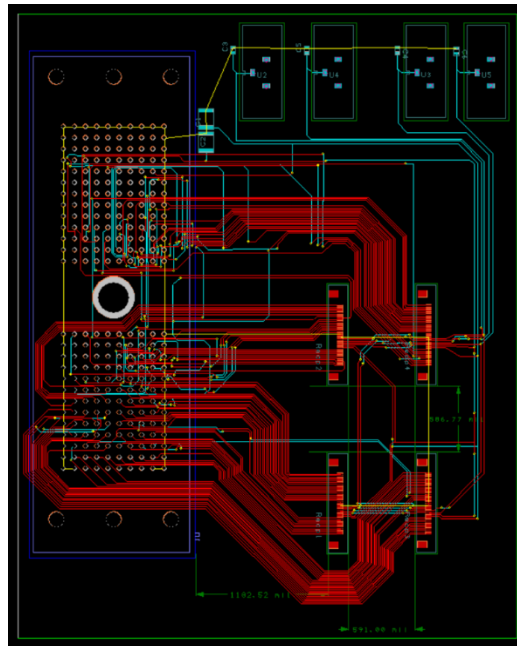


Figure 7.4. 5x4.5 square inches two layer PCB designed for breakout module.

7.4 Concluding Remarks

The major contribution of this dissertation work is to reduce the dielectric charging effect of the CMUT array. At the same time, the transduction efficiency was improved at a low bias voltage than the collapse voltage. The frequency drift was minimized. The bias voltage can easily be increased without operating the CMUT in non-linear region if the application demands. Several approaches have been discussed to resolve the issues faced during the fabrication process and different scope of utilizing this technique have been shared for future purposes. It also offers excellent planarization capability which can be utilized on materials with high roughness and low uniformity. The use of BCB is a breakthrough to one of the crucial limitations of the capacitive based MEMS technology and this will create the opportunity of future research work to utilize the maximum potential of CMUT for various application.

APPENDICES

Appendix A. Advanced kinetic model for Cyclotene polymerization

The polymerization reaction of Cyclotene is modeled based on the combination of two models with a smooth transition [27]. The polymerization of BCB is governed by diffusion process when the polymer is in glassy state and chemical reaction process when the polymer is in the gel state. The overall reaction rate constant, α is the sum of both, however, the terms are combined with a smooth step-function.

$$\frac{d\alpha}{dt} = k_r(T) f(\alpha) f_{step}(\alpha, T) + k_d(T) f(\alpha) [1 - f_{step}(\alpha, T)] \quad (\text{A.1})$$

The step-function is a function of temperature, T and the glass transition temperature, T_g . This function generates a value between one and zero. The following expression was used for the step-function:

$$f_{step}(\alpha, T) = \frac{1}{1 + \exp[-B(T - T_g(\alpha))]} \quad (\text{A.2})$$

Where B is a parameter to smooth the transition between the two reaction states. The value was set at 0.1 to get a change in the temperature range of $\pm 5^\circ\text{C}$ around the glass transition temperature. The glass transition temperature depends on the extent of cure, and was estimated as:

$$T_g = \frac{17500}{27} \alpha^2 - \frac{10865}{27} \alpha + \frac{3070}{27} \quad (\text{A.3})$$

For both reaction regimes, a first-order reaction model was used based on a good fit.

$$f(\alpha) = 1 - \alpha \quad (\text{A.4})$$

The model uses two different reaction models for chemically and diffusion controlled states:

$$k_r = A_r \exp\left[\frac{-E_r}{R}\left(\frac{1}{T} - \frac{1}{T_0}\right)\right]; k_d = A_d \exp\left[\frac{-E_d}{R}\left(\frac{1}{T} - \frac{1}{T_0}\right)\right] \quad (\text{A.5})$$

Where $R = 8.31 \times 10^{-3} \text{ kJ.mol}^{-1}\text{°C}$ is the universal gas constant. The activation energy and the reaction rate at a reference temperature of $T_0 = 210 \text{ °C}$ for the chemically controlled region have an approximate value of $E_r = 157.1 \pm 3.6 \text{ kJ.mol}^{-1}$ and $A_r = 0.27 \text{ h}^{-1}$ respectively. For the diffusion controlled region, an activation energy, $E_d = 166.1 \pm 8.1 \text{ kJ.mol}^{-1}$ was measured. The result for the diffusion reaction rate at the reference temperature of $T_0 = 210 \text{ °C}$ is $A_d = 1.41 \text{ h}^{-1}$. Integrating equation (A.1) by knowing the curing profile $T(t)$, the curing profile and final curing level of BCB can be estimated. The commercially available Cyclotene™ is indeed a B-staged resin with the pre-curing level of $\alpha_0 = 0.35$.

REFERENCES

- [1] BCC Research: New Applications Charging Growth in Ultrasonic Technology Markets in *Entertainment Close Up*, Close-Up Media inc. Jacksonville, USA July 03, 2016.
- [2] A. S. Ergun, G. G. Yaralioglu, O. Oralkan and B. T. Khuri-Yakub, "Techniques & applications of capacitive micromachined ultrasonic transducers" in *MEMS/ NEMS Handbook Techniques and Applications*, C. T. Leondes, Ed., Los Angeles, CA, USA: Springer Science + Business Media Inc. 2006, vol. 2, ch. 7, pp. 222- 332.
- [3] A. Unamuno, "Interview with Anartz Unamuno" in MEMS Report, Fleischer M and Zschiedrich R, Eds. Dresden, Germany. *Fraunhofer Institute of Photonic Microsystems IPMS*, February 2013 [online]. Available: <http://www.ipms.fraunhofer.de/content/dam/ipms/common/mems-reports/m2013-q2-e.pdf> (accessed on 27 October 2016).
- [4] Y. Huang, E. O. Haeggstrom, X. Zhuang, A. S. Ergun and B. T. Khuri-Yakub, "A solution to the charging problems in capacitive micromachined ultrasonic transducers," *IEEE Trans. Ultrason., Ferroelectr., and Freq. Control*, vol. 52, no. 4, pp. 578-580, April 2005.
- [5] S. Machida, T. Takezaki, T. Kobayashi, H. Tanaka and T. Nagata, "Highly reliable CMUT cell structure with reduced dielectric charging effect," *Ultrasonics Symposium (IUS), 2015 IEEE International*, Taipei, 2015, pp. 1-4.
- [6] G. Papaioannou and R. Plana, "Physics of charging in dielectrics and reliability of capacitive RF-MEMS switches," in *Proc. Advanced Microwave and Millimeter Wave Technologies Semiconductor Devices Circuits and Systems*, pp. 275-302, 2010.
- [7] S. Machida, S. Migitaka, H. Tanaka, K. Hashiba, H. Enomoto, Y. Tadaki, "Analysis of the charging problem in capacitive micro-machined ultrasonic transducers," in *Proc. IEEE Ultrasonics Symp.*, pp. 383-385, 2008

- [8] K. Midtbo and A. Ronnekleiv, "Analysis of charge effects in high frequency CMUTs," in *Proc. IEEE Ultrasonics Symp.*, pp. 379-382, 2008.
- [9] H. Martinussen, A. Aksnes and H. E. Engan, "Investigation of charge diffusion in CMUTs using optical interferometry," in *Proc. IEEE Ultrasonics Symp.*, pp. 1218-1221, 2008.
- [10] A. Bakhtazad, R. Manwar, and S. Chowdhury, "Fabrication and characterization of sealed cavities realized by adhesive wafer bonding with dry etched Cyclotene™," *Microsystem Technologies*, pp. 2435-2442, 2015.
- [11] A. Logan and T. W. Yeow, "Fabricating capacitive micromachined ultrasonic transducers with a novel silicon-nitride-Based wafer bonding process," in *IEEE Transactions on Ultrasonics, Ferroelectrics, and Frequency Control*, vol. 56, no. 5, pp. 1074-1084, May 2009.
- [12] Y. Huang, A. S. Ergun, E. Haeggstrom, M. H. Badi and B. T. Khuri-Yakub, "Fabricating capacitive micromachined ultrasonic transducers with wafer-bonding technology," in *Journal of Microelectromechanical Systems*, vol. 12, no. 2, pp. 128-137, Apr 2003.
- [13] Y. Tsuji, M. Kupnik and B.T. Khuri-Yakub, "Low temperature process for CMUT fabrication with wafer bonding technique," *IEEE International Ultrasonics Symposium*, San Diego, CA, pp. 551-554, 2010.
- [14] Q. Zhang, P. V. Cicek, K. Allidina, F. Nabki and M. N. El-Gama, "Surface- Micromachined CMUT Using Low-Temperature Deposited Silicon Carbide Membranes for Above-IC Integration," in *Journal of Microelectromechanical Systems*, vol. 23, no. 2, pp. 482-493, April 2014.
- [15] Y. L. Huang, A. S. Ergun, E. Haeggstrom, M. H. Badi and B. T. Khuri-Yakub, "Fabricating capacitive micromachined ultrasonic transducers with wafer-bonding technology", *J. Microelectromech. Syst.*, vol. 12, pp. 128-137, Apr. 2003.

- [16] O. Oralkan, B. Bayram, G. G. Yaralioglu, A. S. Ergun, M. Kupnik, D. T. Yeh, I. O. Wygant and B. T. Khuri-Yakub, "Experimental characterization of collapse-mode CMUT operation," *IEEE Transactions on Ultrasonics, Ferroelectrics and Frequency Control*, vol. 53, no. 8, pp. 1513- 1523, 2006.
- [17] J. Song, C. Xue, C. He, R. Zhang, L. Mu, J. Cui, J. Miao, Y. Liu, W. Zhang, "Capacitive Micromachined Ultrasonic Transducers (CMUTs) for Underwater Imaging Applications," in *MDPI Sensors* vol. 15, pp. 23205–23217, 2015.
- [18] O. Oralkan, S. T. Hansen, B. Bayram, G. G. Yaralioglu, A. S. Ergun, B. T. Khuri-Yakub, "High-Frequency CMUT Arrays for High-Resolution Medical Imaging," in Proc. *IEEE Ultrason. Symp.* vol. 1, pp. 399–402, 2004.
- [19] Y. Huang, A. S. Ergun, E. Haeggström, M. H. Badi, B. T. Khuri-Yakub, "Fabricating Capacitive Micromachined Ultrasonic Transducers with Wafer Bonding," in *IEEE/ASME J. Microelectromech. Syst.* vol. 12, pp. 128–137, 2004.
- [20] T. Zure, J. Hernandez, S. Chowdhury, "Dynamic Analysis of an SOI based CMUT," in Proc. *IEEE International Conference on Industrial Technology (ICIT), Athens, Greece*, vol. 1, pp. 539–544, March 2012.
- [21] B. G. Streetman, K. S. Banerjee, "Field-Effect Transistors. In Solid State Electronics Devices", 7th Ed.; Horton, M., J., Eds.; *Pearson Education, Inc.*: Upper Saddle River, NJ, USA, ch. 6, pp. 289–299, 2015.
- [22] X. G. Zhang, "Etching of Silicon. In Electrochemistry of Silicon and its Oxide" *Kluwer Academic Publishers*, New York, NY, USA, 2004.
- [23] J. A. Voorthuyzen, K. Keskin, P. Bergveld, "Investigations of the Surface Conductivity of Silicon Dioxide and Methods to Reduce it," in *Surf. Sci.* vol. 187, pp. 201–211, 1987.

- [24] V. Sharma, "Study of Charges Present in Silicon Nitride Thin Films and Their Effect on Silicon Solar Cell Efficiencies," *Ph.D. Thesis*, Arizona State University, Tempe, AZ, USA, December 2013.
- [25] J. R. Reid, "Simulation and Measurement of Dielectric Charging in Electrostatically Actuated Capacitive Microwave Switches," in Proc. of the *International Conference on Modeling and Simulation of Microsystems*, San Juan, Puerto Rico, vol. 1, pp. 250–253. April 2002.
- [26] D. Zhao, S. Zhuang and R. Daigle, "A commercialized high frequency CMUT probe for medical ultrasound imaging," in Proc. IEEE Int, Ultrason. Symp., pp. 1-4, 2015.
- [27] R. Manwar, S. Chowdhury, "Experimental Analysis of Bisbenzocyclobutene Bonded Capacitive Micromachined Ultrasonic Transducers," in *MDPI Sensors: Integrated Sensor Arrays and Array Signal Processing*, vol. 16(7), no. 959, June 2016.
- [28] N. Tavassolian, "Dielectric charging in capacitive RF MEMS switches with Silicon nitride and Silicon dioxide," *Ph.D. dissertation*, School of Electrical and Computer Engineering, Georgia Institute of Technology, Atlanta, GA, USA, 2011.
- [29] C. Antoine, S. Bharatan, E. Tarvin, U. Shah and M. Judy, "Low drift in polysilicon-oxide micromachined ultrasonic transducers," in Proc. IEEE Sensors, pp. 476-479, 2011.
- [30] CYCLOTENE Advanced Electronics Resins—Electrical Properties. The Dow Chemical Company [online]. Available: <http://www.dow.com/cyclotene/solution/elecprop.htm> (accessed 18 April 2016).
- [31] Y. H. So, P. Garrou, J. H. Im, D. M. Scheck, "Benzocyclobutene-based polymers for microelectronics" in Proc. *Chemical Innovation*, vol. 31, no. 12, pp-40-47, December 2001 [online]. Available: <http://pubs.acs.org/subscribe/archive/ci/31/i12/html/12so.html> (accessed on October 3, 2016)

- [32] R. Manwar, University of Windsor, Windsor, ON, Canada, Mills LK, The DOW Chemical Company, Midland, MI, USA, Personal communication, 2016.
- [33] M. Woehrmann and M. Topper, "Polymerization of Thin Film Polymers," in *New Polymers for Special Applications*, Gomes A, Ed., InTech 2012, DOI: 10.5772/48205. Available from: <http://www.intechopen.com/books/new-polymers-for-special-applications/polymerization-of-thin-film-polymers>
- [34] F. Windrich, M. Malanin, K. J. Eichhorn, B. Voit, "Rapid Scan In-Situ FT-IR Curing Studies of Low-Temperature Cure Thin Film Polymer Dielectrics in Solid State," *IEEE 66th Electronic Components and Technology Conference*, Las Vegas, NV, USA, June 2016.
- [35] R. Hubbard and R. Garard, "Wafer Level Curing of Polymer Dielectrics with Variable Frequency Microwaves," in Proc. of *15th International Conference on Advanced Thermal Processing of Semiconductors RTP*, Catania, Italy, 2007.
- [36] M. Topper, T. Fischer, T. Baumgartner and H. Reichl, "A comparison of thin film polymers for Wafer Level Packaging," in Proc. of *60th Electronic Components and Technology Conference (ECTC)*, Las Vegas, NV, USA, 2010.
- [37] S. Seok, J. Kim, "A study on effect of wafer bow in wafer-level BCB cap transfer packaging," *Microsystem Technologies*, February 2014, vol: 20(2), pp. 215-219.
- [38] F. Niklaus, R. Kumar, J. McMahon, J. Yu, J. Q. Lu, T. Cale and R. Gutmann, "Adhesive wafer bonding using partially cured benzocyclobutene for three-dimensional integration", *Journal of The Electrochemical Society*, vol. 153, pp. G291-G295, 2006
- [39] V. Dragoi, T. Glinsner, G. Mittendofer, B. Wieder, P. Lindner, "Adhesive wafer bonding for MEMS application," in Proc *SPIE*, vol. 5116, pp. 160–167, 2003.
- [40] A. Modafe, "Benzocyclobutene-based electric micromachines supported on microball bearings: design, fabrication, and characterization," *Ph.D. dissertation*, University of Maryland, Maryland, MD, USA, 2007.

- [41] N. Ghalichechian, "Integration of benzocyclobutene polymers and silicon micromachined structures fabricated with anisotropic wet etching," *M.S. thesis*, University of Maryland, Maryland, MD, USA 2005.
- [42] G. Roelkens, J. Brouckaert, D. Van Thourhout, R. Baets, R. Notzel and M. Smit, "Adhesive Bonding of InP/InGaAsP Dies to Processed Silicon-On-Insulator Wafers using DVS-bisBenzocyclobutene," *Journal of the Electrochemical Society*, vol. 153, no. 12, pp. 1015-1019, 2006.
- [43] S. Seok, N. A. Rolland, P. A. Rolland, "Mechanical and electrical characterization of benzocyclobutene diaphragm packaging," in *Proc. of Electronic Components and Technology Conference (ECTC07)*, vol 1, pp 1685–1689, 2007.
- [44] B. Cox, "Acoustics for ultrasound imaging," in *Lecture Notes*, London:University College, 2012.
- [45] R. Brennan, "Ultrasonic nondestructive evaluation of armor ceramics," *Ph.D. dissertation*, Rutgers University, NJ, USA, 2007.
- [46] F. A. Firestone, "The Supersonic Reflectoscope, an Instrument for Inspecting the Interior of Solid Parts by Means of Sound Waves," *Journal of the Acoust. Society of America* 17, 287-99, 1945.
- [47] J. A. Woo, "Short history of the development of ultrasound in obstetrics and gynecology." Available: <http://www.ob-ultrasound.net/history1.html>
- [48] G. D. Ludwig, The velocity of sound through tissues and the acoustic impedance of tissues. *J. Acoust. Soc. Am.* 22:862-866, 1950.
- [49] I. Edler, K. Lindstrom, "The history of echocardiography," in *Ultrasound Med Biol*, vol. 30, pp.1565–644, 2004.

- [50] J. J. Wild and J. M Reid, "Application of echo-ranging techniques to the determination of structure of biological tissues," *Science* vol. 115, pp. 226-230, 1952.
- [51] J. J. Wild and J. M Reid, "Current developments in ultrasonic equipments of medical diagnosis," *IRE Trans. Ultrason. Engng.* vol. 5, pp. 44-56, 1952
- [52] T. L. Szabo, "Diagnostic ultrasound imaging: Inside out.: *Elsevier Academic Press* Burlington, MA, 2004.
- [53] N. M. Tole, "Ultrasound beam shape. Basic physics of ultrasonic imaging," in *Geneva World Health Organisation*, H. Ostensen (ed.), 39-47, 2005
- [54] L. W. Schmerr, "Fundamentals of Ultrasonic Phased Arrays," *Springer*, New York, 2015.
- [55] Introduction to Phased Array Technology Applications, R/D Tech Guideline, *Olympus NDT*, MA, USA, 2007.
- [56] Verasonics Inc., WA, USA. [Online]. Available: <http://verasonics.com/new-transducer-page/>.
- [57] NDK Co. Ltd., Japan, "Basic principle of medical ultrasonic probes (transducer)", Available: <http://www.ndk.com/en/sensor/ultrasonic/basic02>.
- [58] Onda Corporation, CA, USA, "Table of acoustic properties of material", Available: http://www.ondacorp.com/tecref_acoustictable.
- [59] S. Logan, L. L. P. Wong, and J. T. W. Yeow, "A 1-D Capacitive Micromachined Ultrasonic Transducer Imaging Array Fabricated with a Silicon-Nitride-based fusion process", *IEEE/ASME Transactions on Mechatronics*, vol. 16, no. 5, pp. 861-865, Oct. 2011.
- [60] A. Sako, M. Fukuda, S. Sano, K. Ishida, K. Asafusa, M. Izumi, "Development of Ultrasonic Transducer Mappie with cMUT Technology", [Online]. Available: www.hitachi-medical.co.jp/medix/pdf/vol51/P31-34.pdf

- [61] A. Caronti, G. Caliano, R. Carotenuto, A. Savoia, M. Pappalardo, E. Cianci, V. Foglietti, "Capacitive micromachined ultrasonic transducer (CMUT) arrays for medical imaging", *Microelectronics Journal* vol. 37, pp. 770-777, 2006.
- [62] X. Zhuang, "Capacitive micromachined ultrasonic transducers with through-wafer interconnects", *ProQuest Dissertations and Theses 2008*, Department of Electrical Engineering, University of Stanford.
- [63] I. O. Wygant, D.T. Yeh, X. Zhuang, A. Nikoozadeh, O. Oralkan, A.S. Ergun, M. Karaman, B.T. Khuri-Yakub, "A Miniature Real-Time Volumetric Ultrasound Imaging System" in *Medical Imaging: Ultrasonic Imaging and Signal Processing*, W.F. Walker, S.Y. Emelianov Eds., Bellingham, WA, USA: Proc. of *SPIE*, vol. 5750, pp. 26-36, 2005.
- [64] I.O Wygant, X. Zhuang, D.T. Yeh, S. Vaithilingam, A. Nikoozadeh, Ö. Oralkan, A.S. Ergun, M. Karaman and B.T. Khuri-Yakub, "An Endoscopic Imaging System Based on a Two-Dimensional CMUT Array: Real-Time Imaging Results," presented at the 2005 *IEEE International Ultrasonics Symposium*, Rotterdam, The Netherlands, Sept. 18 - 21, 2005.
- [65] G. R. Lockwood, D. H. Turnbull, D. A. Christopher and F. S. Foster, "Beyond 30 MHz: Applications of high frequency ultrasound imaging," *IEEE Eng. Med. Biol.*, vol. 15, pp. 60-71, 1996.
- [66] P. A. Lewin, "High frequency biomedical and industrial ultrasound applications," in *Proc. of the International Congress on Ultrasonics*, Vienna, April, 2007.
- [67] F. Lizzi, D. Coleman, "History of ophthalmic ultrasound," in *J Ultrasound Med*, vol. 23, pp. 1255–1266, 2004.
- [68] D. J. Coleman, W. F. Konig, L. Katz, "A hand-operated, ultrasound scan system for ophthalmic evaluation," *Am J Ophthalmol*; vol. 68, pp. 256–263, 1969.
- [69] C. J. Pavlin, M. D. Sherar, F. S. Foster, "Subsurface ultrasound microscopic imaging of the intact eye," in *Ophthalmology*, vol. 97, pp. 244–250, 1990.

- [70] C. Bantignies, P. Mauchamp, R. Dufait, F. Levassort, T. Mateo and J. Grégoire, "40 MHz piezo-composite linear array for medical imaging and integration in a high resolution system," in *Proc. IEEE Int. Ultrason. Symp.*, pp. 226-229, 2011.
- [71] J. A. Ketterling, O. Aristizábal, D. H. Turnbull and F. L. Lizzi, "Design and fabrication of a 40-MHz annular array transducer," *IEEE Trans. Ultrason. Ferroelect. Freq. Control*, vol. 52, pp. 672-681, Apr. 2005.
- [72] J. M. Cannata, T. A. Ritter, W. H. Chen, R. H. Silverman and K. K. Shung, "Design of efficient broadband single-element (20-80 MHz) ultrasonic transducers for medical imaging applications," *IEEE Trans. Ultrason. Ferroelect. Freq. Control.*, vol. 50, no. 11, pp. 1548-1557, 2003.
- [73] A. Bezanson, R. Adamson, M. Bance and J. A. Brown, "Fabrication and performance of a miniaturized 64-element high-frequency endoscopic phased array," *IEEE Trans. Ultrason., Ferroelectr., and Freq. Control*, vol. 61, no. 1, pp. 33-43, 2014.
- [74] D. Yeh, O. Oralkan, I. Wygant, A. Ergun, J. Wong and T.B.T. Khuri-Yakub, "High resolution imaging with high-frequency 1-D linear CMUT arrays," *IEEE Trans. Ultrason., Ferroelectr., and Freq. Control*, pp. 665-668, 2005.
- [75] A. Shaw, K. Martin, "The acoustic output of diagnostic ultrasound scanner," in *The Safe Use of Ultrasound in Medical Diagnosis*, G. ter Haar, Ed., London, UK: The British Institute of Radiology, ch. 3, pp. 18-45, 2012.
- [76] "Guidelines for the Safe Use of Diagnostic Ultrasound", Health Canada, [online]. <http://www.hc-sc.gc.ca/ewh-semt/pubs/radiation/01hecs-secs255/index-eng.php>
- [77] J. Yang, W. S. Gan, K. S. Tan, M. H. Er, "Acoustic beamforming of a parametric speaker comprising ultrasonic transducers," In *Sensors and Actuators* vol. 125, pp. 91–99, 2005. doi:10.1016/j.sna.2005.04.037.

- [78] P. Ask P, "Ultrasound imaging. Waves, signals and signal processing," A. J. Bjorn, A. S. Emantec (Eds), Trondheim, Norway. vol. I and II, 2000, 1416 pp. *Ultrasound Med Biol* 28:401–402.
- [79] D. Belgroune, J. F. de Belleval, H. Djelouah, "A theoretical study of ultrasonic wave transmission through a fluid-solid interface," *Ultrasonics* vol. 48, pp. 220–230, 2008. doi:10.1016/j.ultras.2008.01.003.
- [80] R. Zhang, C. Y. Xue, C. D. He, Y. M. Zhang, J. L. Song and W. D. Zhang, "Design and performance analysis of capacitive micromachined ultrasonic transducer (CMUT) array for underwater imaging," in *Microsyst. Technol, Springer*, vol. 22, no. 12, pp 2939-2947, December 2016.
- [81] B. Kohout, "Transducer Array Calculation (TAC) GUI-MATLAB," USCT, Karlsruhe Institute of Technology, 2012 [online], Available: <https://www.mathworks.com/MATLABcentral/fileexchange/35657-transducer-array-calculation--tac--gui>.
- [82] T. Zure, "Characterization of a CMUT Array," *M.S. thesis*, Dept. of ECE, University of Windsor, Windsor, ON, Canada, 2012.
- [83] I. O. Wygant, M. Kupnik and B. T. Khuri-Yakub, "Analytically calculating membrane displacement and the equivalent circuit model of a circular CMUT cell," *IEEE Ultrasonics Symposium*, Beijing, pp. 2111-2114, 2008.
- [84] J. Lardiès, F. Bellared, G. Bourbon, P. Le Moal, V. Walter and M. Berthillier, "Characterization of capacitive micromachined ultrasonic transducers," in *Microsyst. Technol, Springer*, vol. 22, no. 3, pp 593-601, March 2016.
- [85] R. Manwar, L. Arjunan, M. Ahmadi and S. Chowdhury, "Resonant frequency calculation of square diaphragms: A comparison," *Circuits & Systems (LASCAS), 2015 IEEE 6th Latin American Symposium*, Montevideo, pp. 1-4, 2015.

- [86] A. S. Ergun, G. G. Yaralioglu and B. T. Khuri-Yakub, "Capacitive micromachined ultrasonic transducers: Theory and technology," *J. Aerospace Eng.*, vol. 16, no. 2, pp. 76-84, 2003.
- [87] G. G. Yaralioglu, A. S. Ergun, B. Bayram, E. T. Khuri-Yakub, "Calculation and measurement of electromechanical coupling coefficient of capacitive micromachined ultrasonic transducers," *IEEE Trans. Ultrason. Ferroelectr. Freq. Control*, vol. 50, pp. 449-456, Apr. 2003.
- [88] IntelliSense Software Corporation of Woburn, MA (2013). "Application note: Microphone Design Analysis" in *Intellisuite Training Manual Version 8.7*.
- [89] C. Chang, K. Firouzi, K. K. Park, A. F. Sarioglu, A. Nikoozadeh, H. S. Yoon, S. Vaithilingam, T. Carver and B.T. Khuri-Yakub, "Acoustic lens for capacitive micromachined ultrasonic transducers," *Journal of Micromechanics and Microengineering, IOPscience*, vol. 24, no. 8, July 2014.
- [90] J. M. Cannata, J. A. Williams, Qifa Zhou, T. A. Ritter and K. K. Shung, "Development of a 35-MHz piezo-composite ultrasound array for medical imaging," in *IEEE Trans. on Ultrason., Ferroelectr., Freq. Control*, vol. 53, no. 1, pp. 224-236, 2006.

VITA AUCTORIS

Name:	Rayyan Manwar
Place of birth:	Dhaka, Bangladesh
Year of birth:	November, 1990
Education:	Islamic University of Technology, Gazipur, Dhaka. (2008-2011) B.Sc. in EEE University of Windsor Windsor, ON (2012-2013) MAsC. in ECE (switched to Ph.D.) University of Windsor Windsor, ON (2013-2017) Ph.D in ECE